

University of St Andrews



Full metadata for this thesis is available in
St Andrews Research Repository
at:

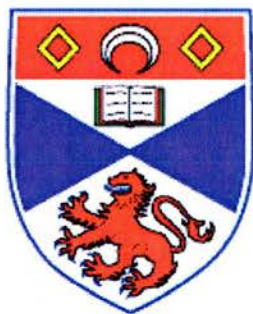
<http://research-repository.st-andrews.ac.uk/>

This thesis is protected by original copyright

PHOTONIC CRYSTAL WAVEGUIDES AND TUNABLE FILTERS IN *InP*

Thesis submitted for the degree of Doctor of Philosophy to the
University of St. Andrews
by

Maria Victorovna Kotlyar



June 2005



Th E975

I, Maria V. Kotlyar, hereby certify that this thesis, which is approximately 30 000 words in length, has been written by me, that is the record of work carried out by me and that it has not been submitted in any previous application for a higher degree

date 01/06/05

signature of candidate..

I was admitted as a research student in October, 2001 and as a candidate for the degree of Doctor of Philosophy in October, 2001; the higher study for which this is a record was carried out in the University of St Andrews between 2001 and 2005.

date 01/06/05

signature of candidate.

I hereby certify that the candidate has fulfilled the conditions of the Resolution and Regulations appropriate for the degree of Doctor of Philosophy in the University of St Andrews and that the candidate is qualified to submit this thesis in application for that degree.

date 01/06/05

signature of supervisor.

In submitting this thesis to the University of St Andrews I understand that I am giving permission for it to be made available for use in accordance with the regulations of the University Library for the time being in force, subject to any copyright vested in the work not being affected thereby. I also understand that the title and abstract will be published, and that a copy of the work may be made and supplied to any *bona fide* library or research worker.

date 01/06/05

signature of candidate.

*Я покинул родимый дом,
Голубую оставил Русь.
В три звезды березняк над прудом
Теплит матери старой грусть.*

*Золотою лягушкой луна
Распласталась на тихой воде.
Словно яблонный цвет, седина
У отца пролилась в бороде.*

*Я не скоро, не скоро вернусь!
Долго петь и звенеть пурге.
Стережет голубую Русь
Старый клен на одной ноге.*

*И я знаю, есть радость в нем
Тем, кто листьев целует дождь,
Оттого, что тот старый клен
Головой на меня похож.*

Сергей Есенин

For my parents Victor & Margarita



Abstract

The subject of this thesis is passive two-dimensional and active one-dimensional photonic crystals (PhCs) in InP-based material. PhC-based devices are attractive for the realization of microphotonic integrated circuits due to their small sizes and novel functionalities. Making PhC functionalities active can offer unique and ultra-compact tunable components for modern optical networks. The fabrication of PhCs in InP heterostructure gives access to several electro-optic effects and provides gain at the telecommunications wavelengths of 1.3 and 1.55 μm .

As the first step on the way to the realisation of high-quality InP-based PhCs, chlorine based chemically assisted ion beam etching was studied in the thesis. An etching technique favourable for the fabrication of high-aspect-ratio features was developed.

Deeply etched ($> 5 \mu\text{m}$) PhC planar waveguides in InP/InGaAsP, with three air rows removed, were fabricated making use of the above mentioned etching regime of the chemically assisted ion beam etching. The processed PhC waveguides were optically characterized and record low propagation losses ($\sim 1.8 \text{ dB/mm}$) were measured. A Fourier transform technique was applied to an experimental transmission spectrum of PhC waveguides in order to determine the propagation losses.

One-dimensional PhC-based cavities in InP/InGaAsP were designed to realise tunable devices. Two tuning mechanisms, the quantum confined Stark effect and free carrier-injection, were used in order to shift the cavity resonances. Blue- and red-shifts of $\sim 2 \text{ nm}$ were experimentally observed for cavities of only 20- μm in length. The comparison of both these tuning mechanism was made, highlighting the advantages and disadvantages of the methods.

Acknowledgements

I would like to thank all people whose support, interest, patience, time, prayers, enthusiasm, inspiration and ideas have made this thesis possible.

It has happened that our University bears the name of the saint patron of Scotland & Russia whose blessing assisted me through my PhD studies and helped me find my husband in this lucky city of St Andrews.

I suspect my fate to write this thesis was decided even before my birth when my pregnant mother and father, final-year students in physics, were writing up their graduation works.

There are so many people I would like to thank that in order not to forget someone (although I am afraid I will still miss someone, so I am sorry in advance) I will start my acknowledgements in a chronological order.

The excellent lectures at Physics Department of Samara State University and especially my supervisor, Professor V. V. Ivakhnik, gave me the necessary solid knowledge to be able to undertake this PhD and I am very grateful to them for it.

My parents, Victor & Margarita were the ones who gave me the idea to come to St Andrews and tried their best inspiring me in this totally novel for me experience of moving to a foreign country and have been giving me all their love and never-ending support through all these years abroad.

Professor Alan Miller, the then Head of the School, his secretary Mary Rodger and professor Andy Mackenzie made a lot to help me find my future supervisor - thank you all very much for your participation.

Let me say thanks to Donald H Brown and Dr Svetlana Tatarkova who made my transfer to the University and PhD life smooth and easy.

I would like to say special thanks to my supervisor Thomas F Krauss who wisely and patiently guided me through my studies towards this degree.

My friends Natalie Palina and Svetlana Zinoveva, who are also PhD students at Bonn University (Germany), gave me their spiritual help and I am very thankful to them for it.

My especial gratitude is to my grandmother Taisia Shanina for her love and care.

Mr George Robb is the one who made sure that all equipment is in the excellent order and I owe him a lot for this, and also for his friendship during my time here. Big thanks

to my colleagues Dr Rab Wilson, Dr Lijun Wu, Dr Michael Mazilu and Tim Karle whose helpful explanations pointed me in the right direction not once.

This thesis would not have been done without my husband's (William Whelan-Curtin) never ceasing support, who was patient enough to help me with my grammar and gave me lots of useful ideas.

And finally, let me say thanks to my two examiners Professor Allan Miller (St Andrews University) and Professor Srinivasan Anand (KTH, Sweden) who kindly agreed to spend their time and efforts reading and improving this thesis.

Publication list

Journal papers

- [1] M. V. Kotlyar, T. Karle, M. D. Settle, L. O'Faolain, and T. F. Krauss, "Low-loss photonic crystal defect waveguides in InP," *Appl. Phys. Lett.*, vol. 84, pp. 3588-3590, May 2004.
- [2] M. V. Kotlyar, L. O'Faolain, R. Wilson, and T. F. Krauss, "High-aspect-ratio chemically assisted ion-beam etching for photonic crystals using a high beam voltage-current ratio," *J. Vac. Scien. Technol. B*, vol. 22, pp. 1788-1791, July 2004.
- [3] M. V. Kotlyar, L. O'Faolain, A. B. Krysa and T. F. Krauss, "Electrically tunable Multiquantum-Well InGaAsP/InGaAsP microphotonic filter," *IEEE Phot. Technol. Lett.*, vol. 17, pp. 837-839, Apr 2005.
- [4] M. V. Kotlyar, L. O'Faolain, A. B. Krysa and T. F. Krauss, "Electro-optic tuning of InP-based microphotonic Fabry-Perot filters," *J. Lightwave Technol.*, to be published, 2005.
- [5] T. F. Krauss, M. V. Kotlyar, L. O'Faolain, R. Wilson, M. Settle, and T. Karle, "Photonic crystal channel waveguides in InP," *Proc. SPIE Photonics West*, paper 5360-24, Jan 2004.

Conference papers

- [1] M. V. Kotlyar, T. F. Krauss, and T. J. Karle, "Dry etch of GaAs/AlGaAs heterostructures based on chemically assisted ion beam etching", *Proc. Workshop and EOS Topical meeting on two dimensional photonic crystals*, Ascona, Switzerland, Aug 2002.
- [2] T. F. Krauss, M. V. Kotlyar, L. O'Faolain, R. Wilson, M. Settle, T. Karle, A. Bristow, A. Tahroui, M. Skolnich, and M. Fox, "Functional photonic crystal waveguides and lattices," *Proc. International Symposium on Photonic and Electromagnetic Crystal Structures V (PECS-V)*, Kyoto, Japan, Mar 2004

- [3] M. V. Kotlyar, L. O'Faolain, T. F. Krauss, "Low loss InP photonic crystal waveguides", *Proc. Semiconductor and Integrated Optoelectronics Conference*, Cardiff, UK, Apr 2004.
- [4] M. V. Kotlyar and T. F. Krauss, "Deeply etched tunable filters in InP-based material", *Proc. Emerging Technologies in Optical Sciences*, Cork, Ireland, Jul 2004.
- [5] M. V. Kotlyar, L. O'Faolain, A. Krysa and T. F. Krauss, "Compact Multiquantum-well tunable filters in InP," *International Symposium on Photonic and Electromagnetic Crystal Structures V (PECS-VI)*, Crete, Greece, to be presented, Jun 2005.

Contents

Abstract	V
Acknowledgements.....	VI
Publication list.....	VIII

1. Introduction and Motivation: Towards All-Optical Photonic Crystal-based

Integrated Circuits	1
1.1 The need for photonic integrated circuits.....	1
1.2 Existing photonic integrated circuits.....	2
1.2.1 Passive.....	2
1.2.2 Active.....	4
1.3 Photonic crystals.....	8
1.3.1 Photonic band gaps.....	8
1.3.2 Localization of light inside photonic crystals.....	12
1.3.3 Light-line.....	13
1.3.4 Three-dimensional photonic crystals.....	14
1.4 Passive photonic crystals devices.....	16
1.5 Active photonic crystals devices.....	18
1.6 Work presented in this thesis.....	21
References.....	23

2. Fabrication of one- and two-dimensional photonic crystals..... 31

2.1. Passive one-dimensional photonic crystals.....	31
2.1.1 Electron-beam lithography.....	32
2.1.1.1 Electron-beam resists.....	33
2.1.1.2 The proximity effect.....	34
2.1.1.3 Different methods of producing 100-nm wide lines.....	35
2.1.1.4 Summary of the e-beam writing process.....	38
2.1.2 Reactive ion etching.....	39
2.1.3 Chemically assisted ion beam etching.....	40

2.1.4 Photolithography process.....	42
2.2 Fabrication of active filters.....	43
2.2.1 Insulation and contact pads fabrication.....	44
2.2.2 Three-point alignment for the fabrication of active devices	45
2.3 Two-dimensional photonic crystal fabrication.....	50
2.4 Summary.....	51
References.....	52
3. Dry etching of one- and two-dimensional InP- and GaAs-based photonic crystals.....	53
3.1 Overview of advanced plasma processing etching systems.....	53
3.2 Chemically assisted ion-beam etching system.....	55
3.2.1 Basics of operation	55
3.2.2 Special features of the machine used in our work.....	55
3.2.3 Nature of the chemical/physical balance with respect to large features.....	56
3.3 High-voltage low-current etching regime.....	59
3.3.1 Conditions for balanced etching process for high-aspect-ratio features	60
3.3.2 Semiconductor/mask selectivity.....	63
3.3.3 “Neck” formation.....	66
3.3.4 Low sidewall roughness.....	67
3.3.5 Etching of two-dimensional photonic crystals.....	68
3.3.6 Comparison of achieved etch depths	69
3.4 Summary.....	71
References.....	72
4. Propagation losses.....	74
4.1 Origin of propagation losses in photonic crystal waveguides.....	74
4.2 Propagation losses analysis (theory).....	76
4.2.1 Theoretically simulated Fabry-Perot fringes.....	76
4.2.2 Fourier transform of Fabry-Perot fringes.....	77
4.2.3 Limitations and errors of the method.....	80

4.3 Photonic crystal propagation losses measurements.....	82
4.3.1 Description of photonic crystals used in this work.....	83
4.3.2 Fourier transform of photonic crystal transmission spectrum.....	84
4.3.3 Finding losses via interference technique.....	90
4.4 Summary.....	91
References.....	92
5. Tunable filters in one-dimensional photonic crystals in InP heterostructure.....	94
5.1 Introduction.....	94
5.2 Passive filter design.....	96
5.2.1 Filter parameters.....	96
5.2.2 Bragg resonator as a model for a filter design.....	97
5.3 Quantum confined Stark effect.....	101
5.3.1 Theory background.....	102
5.3.2 Wafer design.....	104
5.3.3 Three-dimensional modelling: diffraction losses.....	105
5.3.4 Operation in a single lateral mode.....	107
5.3.5 Fabrication of quantum confined Stark effect–based tunable filters.....	108
5.3.6 Experimental results and analysis.....	109
5.4 Carrier-injection.....	113
5.4.1 Theory background.....	114
5.4.2 Carrier-injection based device description	117
5.4.3 Experimental results and discussion	119
5.4.4 Lasing characteristics of the cavities.....	124
5.5 Comparison of tunable filters operated by quantum confined Stark effect and carrier injection.....	128
5.6 Summary.....	130
References.....	132
6 Conclusion.....	136
6.1 Achieved results.....	136

6.2 Possible improvements and future work.....	138
References.....	141

Chapter 1

Introduction and Motivation: Towards All-Optical Photonic Crystal-based Integrated Circuits

1.1 The need for photonic integrated circuits

Integrated circuits in electronics have been in intensive use since they were first released commercially in 1961. Their optical equivalent - photonic integration circuit - is a very attractive goal for the modern telecommunications industry. Optical integrated circuits have several advantages over electrical integrated circuits and conventional optical systems. Among those advantages are: smaller size, lower power, higher speed, and increased bandwidth. The possibility of the integration of many devices fabricated and arranged in different ways simultaneously in one fabrication process reduces significantly the cost of packaging individual components.

Microphotonic periodic structures, which are able to confine light on a wavelength scale and can operate in the forbidden gap at the frequency of the interest- known as Photonic Crystals (PhC) - are one of the most attractive and challenging candidates for components of optical integrated circuits. Integration of photonic crystals into optical circuits would provide additional ultra-miniaturization. Furthermore, PhCs promise to provide additional functionalities (dispersion, slow light) over conventional waveguide geometries.

Photonic crystal research aims to develop various novel nanophotonic devices and then utilise these devices to design monolithic optoelectronic chips as replacements for the racks of hybrid boxes that now switch and route optical networks. This will revolutionize the dense wavelength division multiplexing (DWDM) [1] systems market (at the moment, DWDM is the clear winner for the future of optical networks) by integrating all of the optical elements on a single chip.

PhC-based devices suitable for passive components for optical integrated circuits have been intensively studied for some time. However, PhCs offering a realization of active components for integration are still at the early stages of their development, with fabrication being the main issue. Thus, in this thesis we mainly focus on means of realisation and fabrication of such active PhC elements.

1.2 Existing photonic integrated circuits

To begin with, it is worthwhile to note that despite the impressive advances in the photonics industry in the last decade, optical-electrical-optical (OEO) conversion [2] is still required in core optical networks. OEO conversion involves the transformation of the optical signals to electrical ones, after which they may be amplified, regenerated or switched, and then reconverted to optical signals. Developing photonic switching can in future replace existing electronic network switches with optical ones, removing the need for OEO conversion.

Existing devices for photonic circuits can be divided into two main classes: silica-based devices and InP-based devices. Most of the devices suitable for (D)WDM transmission techniques can be successfully fabricated in both material systems.

1.2.1 Passive

Wavelength multiplexers and demultiplexers are the main components in (D)WDM systems. They combine and recombine optical signals at different wavelengths, increasing the capacity of the embedded fibre. Research on integrated optic (de)multiplexers has been, for the last decade, mainly focused on arrayed waveguide gratings (AWG) (also called phased-array (PHASAR) based devices) [3] and some simpler splitter/coupler geometries. In AWGs (Fig. 1a), an array of waveguides of suitably chosen lengths provides the focusing and dispersive properties required for demultiplexing (they image the input field onto an array of output waveguides). Most commercial splitters are based on Y-junction (Fig. 1b) [4] whereas couplers use directional coupler geometry (Fig. 1c) [5]. Since the emergence of the multimode interference (MMI) couplers in 1996 [6] consisting of single-mode input and output waveguides separated by a multimode slab region, the realization of a novel type of

AWG based on MMI-couplers with very uniform channel response have been possible [7].

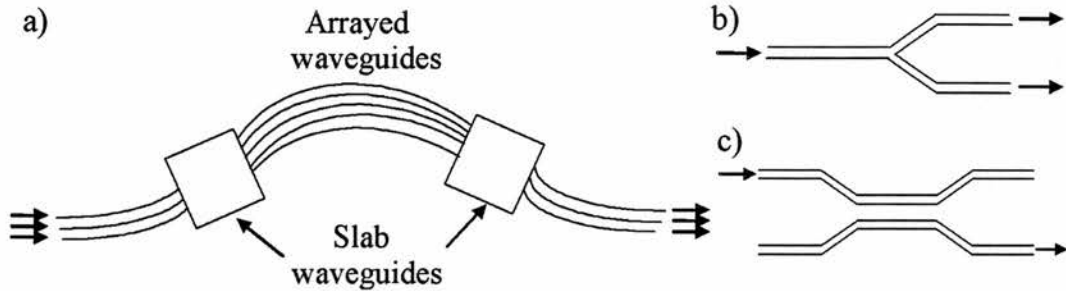


Fig. 1. Schematic representation of various components of (D)WDM systems: a) AWG, b) Y-junction, c) directional coupler.

Wavelength routers based on the extension of the AWG concept from $1 \times N$ to $N \times N$ devices were first reported by Dragone [8]. Such routers provide an important additional functionality compared with multiplexers and demultiplexers and play an important role in more complex devices such as add-drop multiplexers and wavelength switches [9, 10]. The new functionality of the wavelength router consists of the ability to realize complex interconnectivity schemes where each out-put channel receives N different frequencies (one from each input channel).

Although AWGs are key passive waveguide devices in photonic integrated circuits for (D)WDM applications, there are other devices used for spectral filtering, such as Mach-Zehnder interferometer [11], Fabry-Perot resonators [12] and Bragg gratings [13], which are also popular.

Most of the existing passive devices for photonic integrated circuits were fabricated in both materials (SOI and InP). The main advantage of the silica-based devices is low propagation loss and a high fibre-coupling efficiency, due to use of low-contrast (fibre-matched) waveguide structures. The first silica-based devices had relatively large vertical dimensions ($\sim 50 \mu\text{m}$) due to the low index contrast. However, the emergence of silicon-on-insulator with the large refractive index difference between silicon ($n=3.45$) and SiO_2 ($n=1.46$) largely resolved this issue allowing the realisation of the SOI devices [14] with

small vertical dimensions ($\sim 10 \mu\text{m}$), making them compatible with electronic integrated circuits technology.

In general, InP-based demultiplexers cannot compete with silica-based devices with regard to fiber coupling loss, which makes them less suitable for use in circuits with low complexity. But InP-based devices are ideal for complex optical circuits offering a reduction in volume and interconnection costs. Their main advantage lies in their potential for monolithic integration of active components such as detectors, optical amplifiers, modulators and switches.

1.2.2 Active

To achieve all-optical wavelength conversion, which is important as a method of enhancing routing options and network properties [15], e.g. such as wavelength reuse, various strategies have been investigated. There were originally two kinds of media: semiconductor optical amplifiers (SOA) [16] and fibre loops [17]. In spite of their good performances at high bit rates, the interferometric configurations based upon them are very complex and expensive for practical use.

More recently, electro-absorption modulators (EAM) were investigated for demultiplexing and wavelength conversion. This can be realised via the optical modulation of the EAM by saturation of the absorption. Switching windows as short as 5 ps have been obtained in EAM configurations [18] showing the capability, with dynamic requirements, for operation at high bit rates, in excess of 40 Gbit/s.

Optical filters are additional attractive components for flexible dense wavelength division multiplex networks providing a wide and continuous tuning range. For example, Fabry-Perot filters based on micro-opto-electro-mechanical system (MOEMS) technology have been reported for various material systems and can be used as optical filters, laser diodes and tunable receivers in WDM systems. These systems combine optical functionality with mechanical and electrical parts in a single device. MOEMS were realised via monolithic integration [19] as well as via separation of the MEMS chip and photonic device [20]. But up to 2002, the wavelength tuning range of these devices was approximately 70 nm, limited by the mechanical flexibility of the tunable membrane and the effective optical cavity length. J. Daleiden *et al.* [21] have recently demonstrated

micromechanically tunable Fabry-Perot filters with record wavelength tuning range of 112 nm with the application of only 5 V, exhibiting the extremely wide stop-band of the filters (1250–1800 nm). The present disadvantage of these filters is the rather large full width at half maximum (FWHM) of 3.5–4.5 nm and low speed (\sim ms). Another disadvantage of MOEMS is that they are rather difficult to integrate; also, each mechanical actuator requires fine tuning, which complicates the control electronics.

Fig. 2 shows the most important MOEMS concepts based on silicon for optical switches (a, b, c) and switch matrices (d, e). Additional applications such as optical filters (f) and optical motherboards (g) have recently entered into the optical components market.

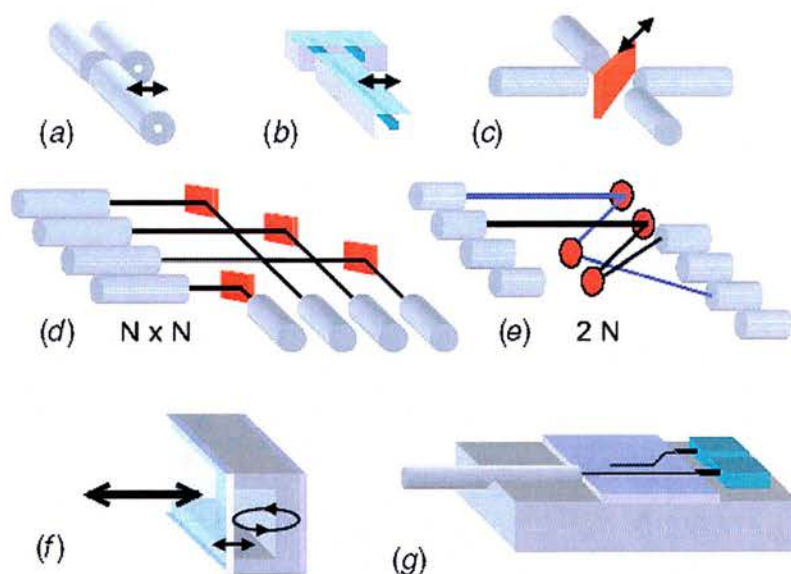


Fig. 2. Si-based MOEMS for optical communication networks: (a) moving-fibre switch; (b) moving-waveguide switch; (c) mirror switch; (d) $N \times N$ matrix switch; (e) $2N$ matrix switch; (f) Fabry-Perot filter; (g) planar lightwave circuit (PLC) [22].

Liquid crystal incorporation into a Fabry-Perot cavity offers another opportunity of creating a tunable optical filter, by changing the optical path in the cavity through changes in the crystal orientation as a result of an applied voltage, the resonant wavelength may be changed [23].

AWGs have also been proposed as tunable optical filters [24] for realisation of a tunable light source for WDM when combined with an optical amplifier. Recently, a novel widely tunable (58 nm) optical filter with a ladder-type structure using free carrier injection for the tuning mechanism was proposed by S. Matsuo *et al.* [25]. This type of structure is superior to tunable filters based on arrayed waveguide grating due to the reduced electrode area and power consumption. The big tuning range was obtained at the cost of a relatively large device size of ~ 1 mm and high injected currents of 30 mA. The experimental 3-dB bandwidth of the reported device is 4.5 nm, which also leaves much to be desired.

Finally, microcavities such as microrings, microdisks, and F-P cavities, broadly demonstrated lately as passive devices for WDM offer simple alternative ways to 2-D PhCs, for the realization of compact active components for optical integrated circuits. Tunability in these configurations was realised mainly by means of forward (free carrier-injection tuning mechanism or thermal tuning) and reverse biasing (quantum confined Stark effect). The experimentally observed tuning ranges were between 0.8 and 4 nm in III-IV semiconductors [26-28]. The Kerr effect was also implemented in the micro-ring resonator configuration producing nonlinear phase-shift [29].

Unfortunately, the spectral tuning range of these micro-resonators is presently rather small (less than 10 nm), however their small dimensions allow operation with very low power consumption and their tuning capabilities can be improved further by the implementation of more advanced designs.

To conclude this section, we present Table 1 showing main tuning mechanisms implemented in the above-described tunable components of photonic integrated circuits. This table compares the main tuning characteristics such as speed and achieved range of tuning, highlighting the typical lengths and consumed powers of the devices.

Table 1. Comparison of the main characteristics of tunable devices implementing different tuning mechanisms

<i>Parameters</i>	<i>Thermo-optic effect</i>	<i>Liquid-crystal</i>	<i>MOEMS</i>	<i>Carrier-injection</i>	<i>QCSE</i>	<i>Kerr-effect</i>
Δn_{modal}	~0.1	0.1	-	~0.005	~0.005	~0.001
$\Delta t(\text{time})$	~ms	ms- μ s	0.1-10ms	~ns	~ps	Instantaneous
<i>Tuning range</i>	~1-30 nm	~100nm	~100nm	~50 nm	~2 nm	~0.5nm
<i>Power</i>	~20mW-2W	~50mW	~5 μ W-mW	~100mW	(<10V)	~40W
<i>Length</i>	20 μ m-1mm	~mm	~mm	~mm	~20 μ m	~50 μ m
<i>Reference</i>	28, 30, 31	23,32	21	25	27,33	29

As one can see from Table 1, large tuning ranges of 30 nm and above are achieved using either long lengths (~mm) or high operating powers (~W). Thus, the implementation of photonic crystals as tunable components for photonic integrated circuits offers miniaturisation of devices that will lead to smaller consumed powers as well.

Concerning the choice of the tuning mechanism chosen for the tunable filters described in this work, several considerations were taken into account such as speed, possible tuning range and complexity. The Kerr effect is the fastest tuning mechanism but it requires a very high operating power and even then offers only small tuning ranges; the thermo-optic effect and LC infiltration both suffer from low speeds; MOEMS, as well as possessing a low tuning speed, are highly complex structures and are difficult to integrate; although QCSE and carrier-injection exhibit rather small refractive index changes, they have the advantages of low power requirements and fast switching, making them attractive as possible tuning mechanisms for compact tunable devices with low

power consumption. Thus, we will choose these two mechanisms to produce microphotonic tunable filters in this thesis. The principles behind these mechanisms will be discussed in Chapter 5.

1.3 Photonic crystals

PhCs have attracted the interest of researchers in basic sciences and engineering since 1987. In this year, the concept of a photonic band gap was formulated as a generalization of well-known 1-D dielectric Bragg mirrors to two or three directions, by two independent researches S. John and E. Yablonovitch [34, 35].

1.3.1 Photonic band gaps

PhCs are materials with a periodically modulated dielectric constant on the scale of the wavelength of light. A photonic band gap, by analogy with an electronic band gap, originates from multiple interferences of waves scattered from the interfaces between layers of different dielectric constants. It creates a forbidden frequency range, within which no propagating electromagnetic modes exist. Thus, inside the material, emission at frequencies within the band gap is suppressed.

The simplest possible PhC is a multilayer film consisting of alternating layers of material with different dielectric constants (ϵ_1, ϵ_2). Fig. 3 illustrates a photonic band gap for this simple case of a multilayer film, which can be considered as a one-dimensional (1-D) PhC, with a period a (lattice constant).

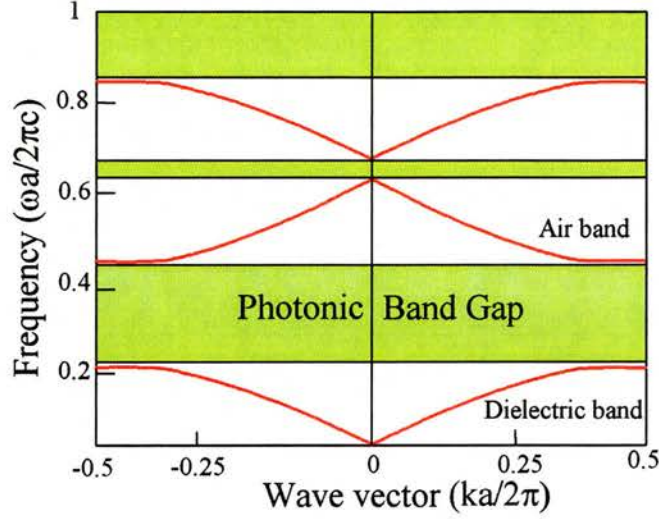


Fig. 3. The photonic band gap structure of a multilayer film. Layers have the dielectric constants of 13 and 1, and widths of $0.2a$ and $0.8a$, respectively [36].

In the case of a 1-D PhC, photonic band gaps appear under the condition of $\epsilon_1/\epsilon_2 \neq 1$ and the bigger the contrast, the bigger the gap. Thus having alternating layers of air ($n=1$) and semiconductor ($n= 3.2 \div 3.6$) gives the biggest possible photonic band gap in practice.

A PhC that is periodic along two of its axes and homogeneous along the third is described as a two-dimensional (2-D) PhC. In this case, photonic band gaps appear in the plane of periodicity with, in general, different band structures for the TE and TM modes. Transverse-electric (TE) modes have the magnetic field normal to the periodicity plane (the plane of propagation), and the electric field in the plane. Transverse-magnetic (TM) modes have the reverse situation.

The rule of “higher index contrast, larger band gap” valid for 1-D PhCs, is also valid for 2-D PhCs. As a consequence of this rule, one of the most promising PhCs configurations consists of either air-holes drilled in a semiconductor or semiconductor islands (e.g. pillars) surrounded by air, thus using maximum possible contrast index achieved.

In terms of polarization-dependent band gaps, a square lattice of dielectric columns (Fig. 4 a) is an example of a structure that has a complete band gap for the TM modes (Fig. 5 a), but not for the TE modes. It can be explained by introducing a “fill factor” parameter, which is the fraction of electrical energy located inside the high- ϵ regions. It is

well known that the mode tends to concentrate most of its displacement energy in the high- ϵ regions in order to lower its frequency. The contrast between the fill factors for the TM modes for the dielectric-band and air-band is larger than for the TE modes in the case of the square lattice of semiconductor pillars. This is due to the vectorial nature of the electromagnetic field where the scalar D_z displacement field of the TM modes can be localized within the dielectric columns, but the continuous field lines of the TE modes are forced to penetrate the air region to connect neighbouring pillows. This is the reason why the TE modes do not have markedly different fill factors, and as a consequence band gaps do not occur.

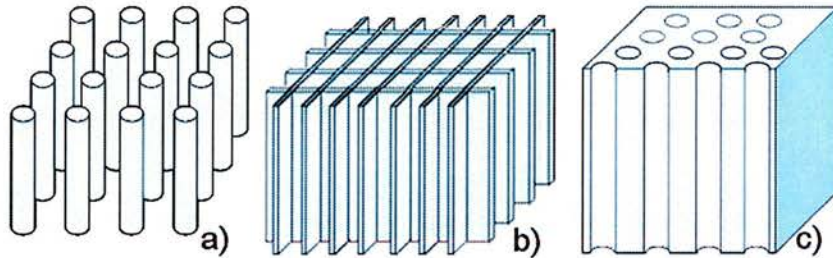


Fig. 4. a) a square lattice of dielectric columns; b) a square grid of dielectric veins; c) a triangular lattice of air columns in a dielectric.

In the case of a PhC structure consisting of high- ϵ regions in the shape of a square grid of dielectric veins (Fig.4 b), there is a gap in the TE band structure (Fig. 5 b), but not for the TM modes. As in this case, the continuous field lines of the transverse \mathbf{D} -field can extend to neighbouring lattices without leaving the high- ϵ regions.

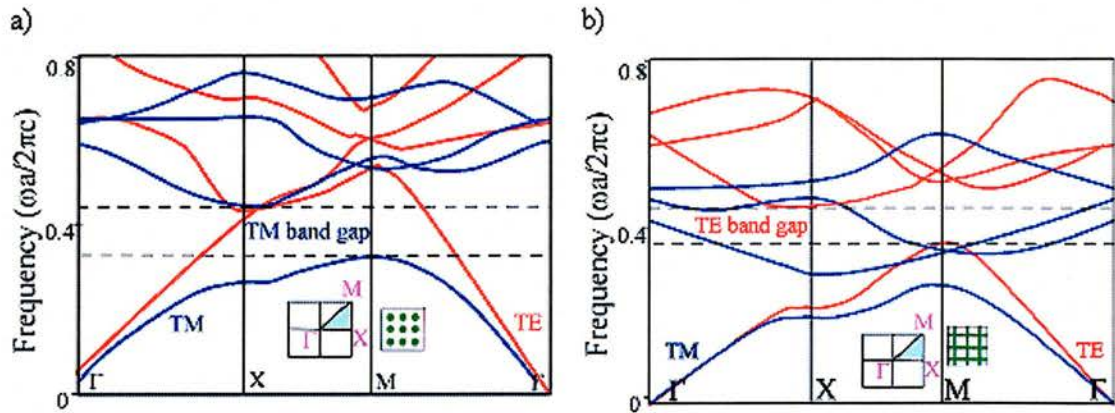


Fig. 5. The photonic band structures exhibiting: a) TM band gap for a square array of dielectric columns with $r=0.2a$; b) TE band gap for a square array of dielectric ($\epsilon=8.9$) veins in air [36].

Thus, summarising these two examples, we can state that TE and TM band gaps are supported by a connected lattice and a lattice of isolated high- ϵ regions, respectively. Thus, the crystals consisting of a hexagonal array of circular columns, each connected to its nearest neighbours by slender rectangular rods (see an inset of Fig. 6) will have a full band gap. Fig. 6 shows the photonic band structure for such type of a structure with TM and TE band gaps overlapping.

A 2-D PhC structure with a triangular lattice of air columns in a dielectric substrate (Fig. 4 c) also exhibits a complete band gap for all polarizations and for particular parameters, e.g. when $r/a = 0.48$ and $\epsilon = 13$, these gaps will overlap.

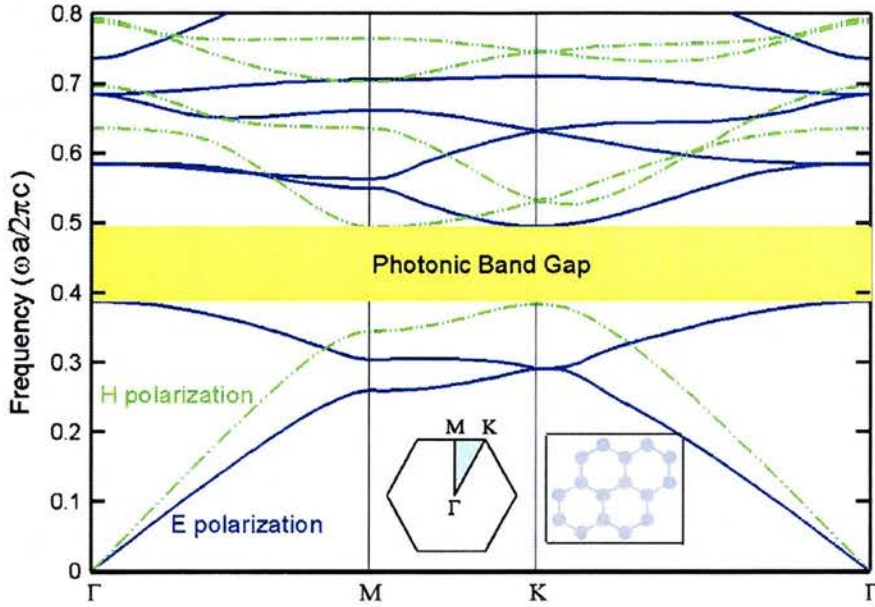


Fig. 6. The complete photonic band gap with overlapping TE and TM band gaps ($r/a = 0.155$ and $\epsilon = 13$). The insets show the high-symmetry points at the corners of the irreducible Brillouin zone (blue) [see Ref. 36, p.34] and a schematic view of a proposed structure [37].

1.3.2 Localization of light inside photonic crystals

Introducing defects inside the crystal structure (perturbing the periodicity) creates localized electromagnetic modes within the photonic band gap [38]. For example, removing rows of air holes (line defects) from the photonic crystal consisting of air columns in a dielectric substrate is one of the ways to create PhC planar waveguides. The PhC structure confines light only horizontally. Introducing a horizontal layer with different dielectric constant inside the slab creates an index-guiding layer which confines light vertically via total internal reflection. Such a slab-type of PhCs has only two-dimensional periodicity and uses index guiding to confine light in the third direction, thus it is still only a 2-D PhC.

Depending on the number of rows removed (1, 2, 3 ...) the PhC planar waveguides are referred to as W1, W2, W3 *etc* waveguides, respectively. Fig. 7 shows an example of W3. If instead of removing entire rows of holes, we just remove several holes in a row, compact high-Q cavities inside the PhC are created.

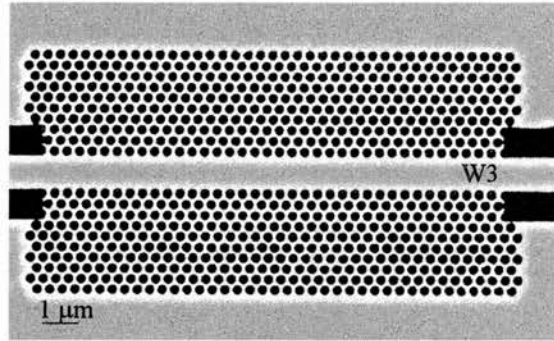


Fig. 7. A scanning electron microscope (SEM) image of W3 in InP.

Changing the size and shape of selected air holes and/or filling them with another dielectric material are other ways to introduce localised modes inside photonic band gaps.

This ability of photonic crystals to confine and guide light in very small volumes and their novel dispersive properties make them attractive for many applications in modern optical telecommunications.

1.3.3 Light-line

Despite the usefulness of the vertical confinement within a PhC, this confinement is imperfect. The typically weak vertical confinement being based on total internal reflection allows coupling to the continuum of radiation modes. These radiation modes are the source of out-of-plane losses that can compromise the performance of the waveguide itself.

The most important element that distinguishes PhC slabs from ideal three-dimensional PhCs is the light cone [39] (the area above the light line in Fig. 8). The light cone describes radiation modes that are extended infinitely in the region outside the slab. Fig. 8 shows a photonic band diagram of a W3 line defect in a 2-D PhC slab of triangular lattice air holes. Here, the slope of the light cone (cladding light line), c/n , is set by the refractive index of cladding material; a higher n implies a lower light cone boundary. The index contrast is an important parameter of PhC slabs, which influences its band gap structure.

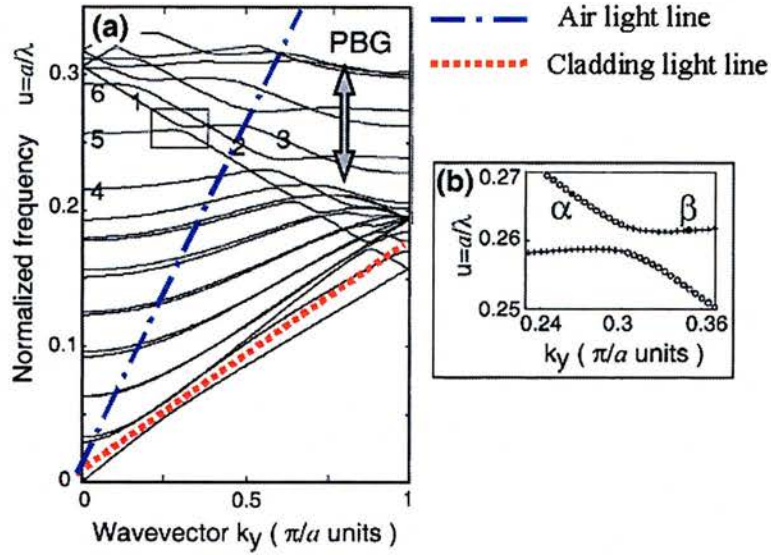


Fig. 8. (a) Photonic band diagram for TE-polarization of $W3^{(K)}$ (waveguides are defined along ΓK) in triangular lattice of air holes ($r/a=0.37$); (b) zoom on the anti-crossing between the fundamental mode and the fifth guided mode (due to multimode nature of $W3$) [40].

“Truly” guided modes (states localised inside the slab) exist only below the light line of the band diagram and do not couple with slab modes. If the waveguide mode of interest lies above the light line it suffers from radiation losses due to out-of-plane diffraction. This is an intrinsic type of loss. These losses can be tolerable if the length of the PhC waveguide is relatively short ($\sim 100 \mu\text{m}$). The origins of various other losses (extrinsic) in 2-D PhC slabs and the two different approaches typically employed (“membranes”-high refractive index contrast and “substrate-type”-low refractive index contrast) for minimizing these losses are discussed in greater detail in Chapter 4.

1.3.4 Three-dimensional photonic crystals

The 1- and 2-D PhC described above provide photonic band gaps only in one and two-dimensions, respectively. Three-dimensional (3-D) PhC (exhibiting periodicity in all three-dimensions) offer a unique opportunity of forming a complete photonic band gap in all three dimensions. This ability to confine and control light in three dimensions would

have important implications for quantum optics and quantum optical devices: the modification of black-body radiation, the localization of light to a fraction of a cubic wavelength, and thus the realization of single-mode light-emitting diodes, are but a few examples.

However, the fabrication of such 3-D structures has been a challenge due to the tendency to have complex 3-D connectivity and strict alignment requirements [41]. Despite these challenges such 3-D designs have been the subject of much recent research.

The first candidates for 3D PhCs were layer-by-layer periodic structures such as one that shown in Fig. 9 (a) [42]. Another simple route by which to fabricate 3-D PhCs with a photonic bandgap at optical wavelengths was through the self-assembly of colloidal microspheres [43]. Currently available colloidal crystals do not have a full photonic bandgap because of their low index contrast. However, these structures may be infiltrated with a high index material and after the removal of the original opal, a porous structure with a full photonic band gap can be created [44, 45].

The combination of the self-assembly approach with defect engineering is important for making PhC based devices. For example, it has been shown that by combining the colloidal crystal self-assembly technique and lithography, air-core line defects can be introduced [46] (Fig. 9 b). Three-dimensional holography may also be used to generate 3-D periodic microstructures by means of the interference of four non-coplanar laser beams in a film of photoresist [47].

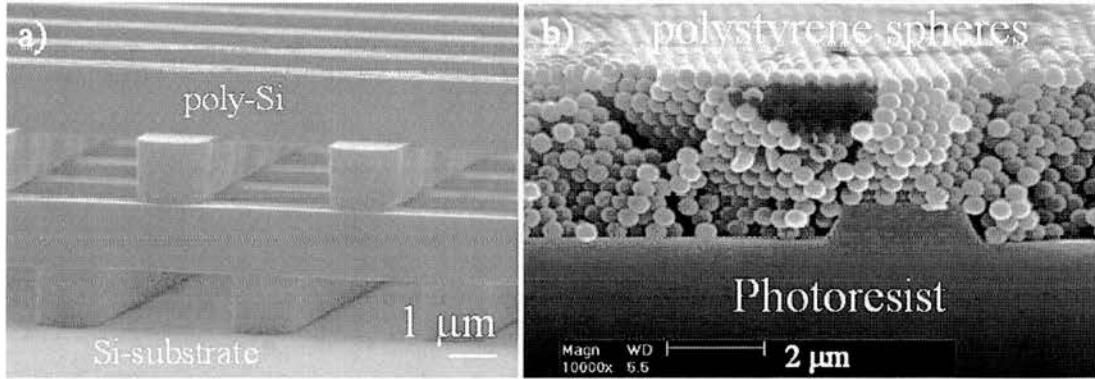


Fig. 9. SEM images of 3-D PhCs structures: a) layer-by-layer structure in polycrystalline silicon [42]; b) patterned colloidal crystal multilayers, assembled using $0.4\ \mu\text{m}$ polystyrene spheres. By removing photoresist stripe air core can be introduced [46].

Therefore, there are a number of methods of fabricating 3-D PhC. However, these techniques still remain rather complex and with many drawbacks. Thus, 2-D PhC slabs, which retain many of the desirable properties of true photonic crystals, offer an easier and more reliable alternative to these complex structures.

1.4 Passive photonic crystals devices

In terms of passive components for optical integrated circuits, various PhC-based devices have been successfully studied in the last two decades. PhC-based single and multi-moded waveguides (WGs) have been fabricated and characterised in various materials and configurations. The propagation loss is one of the main challenges of PhC planar waveguides. The most recent reported propagation losses are $7.6\ \text{dB/cm}$ for *monomode* (W1) PhC-based waveguides of the membrane-type [48] and $20\ \text{dB/cm}$ for multimode (W3) waveguide in substrate approach [49].

Compact 2-D PhC-based Y-junctions have been experimentally realised, in AlGaAs-based material operating at a wavelength of $1.3\ \mu\text{m}$, as efficient 50 % directional couplers [50]. One of the possible applications for PhC-based Y-junctions is as an ultrasmall and ultrafast all optical switching devices in Mach–Zehnder configuration [51]

(see below). Various passive PhC-based Mach-Zehnder interferometers have been already successfully realised [52].

Furthermore, point-like defects in photonic band gap materials behave as resonant microcavities [53] which exhibit high Q-factors (up to 100 000 [54]) that can be used as resonant add-drop filters for WDM systems [55]. Easy to fabricate and model, 1-D PhCs have also been used for creating high reflectivity mirrors for semiconductor lasers with low thresholds [56].

Another attractive feature of PhCs waveguides is their highly dispersive nature, which opens up additional possibilities for functional WGs. M. Notmi *et al.* [57] showed very low group velocity of line defect PhC waveguides with guided modes whose group velocity is 2 orders of magnitude slower than that in air. They also illustrated that group dispersion of PhC WGs can be controlled by changing the defect's width. However, it is challenging to achieve a low group velocity with zero dispersion. For this purpose, a chirped PhC waveguide, which smoothly shifts the photonic band along the waveguide channel, was proposed [58].

The superprism phenomenon is another interesting aspect of planar PhC waveguides. Kosaka *et al.* [59] demonstrated a highly dispersive photonic microstructure in 3-D ("autocloned") PhC, which was termed the "optical superprism". This 3-D structure has very favourable properties, but requires a specialised demanding fabrication technique. As an alternative, the superprism effect was demonstrated in planar 2-D PhCs [60] offering the potential realization of wavelength demultiplexing and light beam deflection.

Dispersion control is an important issue in high-bit-rate optical communication. Dispersion compensating fibres are the most commonly used dispersion compensators in optical communication systems. These are very long, however, and introduce significant latency. In the last ten years, fibre Bragg gratings have emerged [61] and are starting to be introduced into optical networks. However, both of these methods are bulky and hard to tune. Using photonic crystal waveguides as dispersion compensators, these two problems could potentially be overcome: coupled-cavities [62] and coupled waveguides [63] were proposed as compact PhC-based devices for dispersion compensation.

And finally, an easy application of PhCs is as an efficient light extractor in light emitting diodes (LEDs) [64], utilizing a two-dimensional surface grating PhC. The shallow grating and micron order lattice constant makes the fabrication process simple and applicable to most semiconductor devices.

Although PhCs offer great potential for ultra-miniaturization, the small dimensions are a source of severe problems when coupling in and out of the waveguide. In- and out-of-the-plane types of couplers have been proposed for efficient coupling between PhC waveguides and fibre (or dielectric waveguides) [65, 66].

In conclusion, all these PhC-based devices allow the reduction of the size of optical components, leading to their potential integration in large numbers and the possibility to combine the different functionalities by utilising the unique properties of PhCs on a single chip, much in the same way as electronic components have been integrated for improved functionality in microchips. Thus, at the start of the work described in this thesis there were two main tasks to be solved- achieving low propagation loss and adding active functionality.

1.5 Active photonic crystals devices

One of the motivations for using PhCs in integrated optics is their promise to provide additional functionality over conventional waveguide geometries as shown above. Making these novel functionalities active can offer tunable greatly miniaturised photonic components for integrated circuits.

Basically, tunable PhC-based devices utilise the same tuning mechanisms as conventional functional components for existing photonic circuits such as: electro-optic, thermo-optic, electric field and Kerr effects, and liquid crystals.

One of the most straightforward ways of realising tunable PhCs is via modulation, through thermo-optic effect, of the PhC's refractive index. For example, the above mentioned passive PhC-based MZIs have recently been realised with added active functionality by E. A. Camargo *et al.* via the thermo-optic effect [67].

Free carrier injection is another relatively easy way for the realisation of tunability in PhCs. It has also been shown that the intrinsic non-linearity of the material can be enhanced by a photonic resonance, which can be engineered for the desired wavelength.

For example, a wavelength shift of the photonic resonance of a 2-D PhC in AlGaAs induced by photo-created carriers and enhanced by the operation close to photonic resonance was experimentally observed [68] showing a fast decay time of ~ 8 ps. This is much faster than values for a bulk AlGaAs and silicon-based PhCs [69], (100 and 70 ps, respectively). The reduction in the decay time is due to the increased surface area (etched air-holes) providing non-radiative carrier recombination.

Implementing the same tuning mechanism, but in InP-based material instead of AlGaAs, gives an opportunity to produce fast optical PhC-based switchers at fibre optics' favourable wavelengths of 1.3 and 1.55 μm . Very fast (~ 7.3 ps) nonlinear response in InP-based 2D PhC has been recently experimentally demonstrated by F. Raineri *et al.* [70]. This carrier plasma effect has been also used to achieve shifts of the resonant peak (5.6 nm) of a point defect cavity in an InGaAsP PhC slab by photo-pumping (0.85 mW) [71].

By applying an electric field (60 kV/cm) to a 2-D photonic crystal fabricated in PLZT (ferroelectric lead lanthanum zirconate titanate) and thus modifying the band structure and the dispersion surfaces, D. Schrymgeour *et al.* [72] have theoretically shown the deflection of light propagating through the structure up to 49° .

A way to achieve ultra high-speed ($<100\text{fs}$) tunability of PhC-based devices is through the use of nonlinear Kerr materials. PhC-based tunable devices such as WDM channel add-drop filter [73], frequency converter [74] and angular deflector [75] were theoretically demonstrated. Kerr effect based devices are faster than the above-described free carrier injection based devices but much higher optical intensities are required.

The integration of liquid crystals and polymers into PhCs offers another opportunity of tuning photonic band gaps. An inverted opal (3-D PhC) filled with nematic liquid crystal showed complete opening/closing of photonic band gap through the application of an electric field [76]. As an application of this effect, an electrically tuned nematic liquid-crystal infiltrated PhC laser was demonstrated by B. Maune *et al.* [77] with a maximum blue shift of 1.2 nm with an applied 20 V. By optimizing the design, the tuning range of the laser can *potentially* be increased beyond 20 nm, allowing the laser to fulfil a variety of technical applications.

Basically, as described above, tunable PhC-based elements use the same tuning mechanisms as conventional tunable devices used in photonic integrated circuits. The advantages of making PhCs tunable, apart the miniaturisation argument, lie in their dispersion properties. For example, the interaction lengths may be increased through extremely low group velocities. For example, PhC-based all-optical switches can be realised by introducing optical nonlinear materials (e.g. media such as quantum dots) into the 2-D PhC waveguides (Fig. 10). In this situation, the PhC may enhance the nonlinearity due to enhanced light-matter interaction.

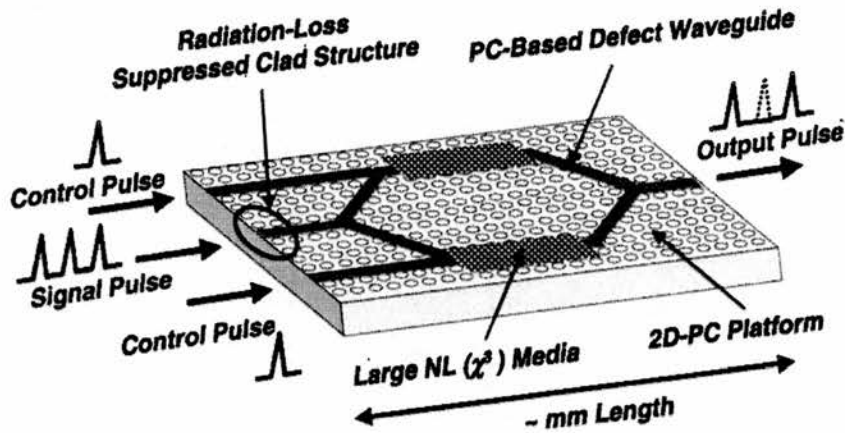


Fig. 10. 2-D PhC platform for demonstrating a Mach-Zehnder type all-optical switch [51].

The next generation of high capacity optical networks will rely on the availability of specific components with functionalities for high-bit-rate optical signal processing. PhC-based devices offer a means for the realization of ultra-compact tunable components for integrated optical circuits. At the same time, PhCs can enhance effects produced by tunable mechanisms resulting in shorter switching times and stronger interactions. Presently, the realization of such submicron scaled tunable devices is difficult due to very demanding and non-trivial fabrication processes involved. Thus, the implementation of active PhC based components within optical integrated circuits is only in its development stage.

As we have indicated before, for the tunable filters designed and fabricated in this thesis two tuning mechanisms were chosen- free carrier injection and QCSE. As we have seen from the above examples, tunable PhC-based devices using carrier-injection have been already implemented in PhCs via optical pumping. This is not practical for large scale circuit switching. Thus, electrical pumping will be used for our tunable filters making them more attractive for practical use in complex integrated circuits.

1.6 Work presented in this thesis

As a conclusion to Chapter 1, we will summarize the challenging areas of microphotonics arising from the current state of the progress in this area and their influence on the work described in this thesis. Here is a list of the motivations for our work:

- 1) III-V semiconductors are preferable materials for active devices in terms of their nonlinear properties and straight forward contacting techniques. InP-based alloys are especially attractive due to the potential of operating at wavelengths of 1.3 and 1.55 μm and, thus, they are promising for integration with optical circuits.

Conclusion: We use InP-based materials in this work.

- 2) The PhC concept, which has blossomed in the last decade, possesses unique properties which can improve conventional device performances with additional new functionalities. PhCs can also allow a higher degree of integration and cost reduction in optical integrated circuits.

Conclusion: PhCs are used as the base model for our devices.

- 3) Propagation losses are one of the main issues in the way of PhC implementation for mass-productions. At the beginning of this work there were only a few experimental quantitative figures on propagation losses in PhCs, especially semiconductor based.

Conclusion: Low-loss planar PhC waveguides were fabricated and characterised in InP.

- 4) The etching of high-aspect-ratio features in InP were a severe obstacle preventing the fabrication of PhCs in InP. The first promising results in etching deep PhCs in InP heterostructures started to appear only in 2001.

Conclusion: Improved etching conditions for dry etching of InP were developed in this thesis.

- 5) Tunable devices for photonic integrated circuits are greatly required. PhCs offers opportunities for realisation of tunability on a miniaturised scale.

Conclusion: Several different ways of realisation tunability in PhC-based devices were presented and analysed.

Thus, in this thesis, we have concentrated on the fabrication and characterization of active/passive 1- and 2-D photonic crystals in InP-based material. In Chapter 2 of this thesis, an overview of the fabrication of passive and active 1- and 2-D InP-based PhCs is presented. Chapter 3 resolves issues connected with difficulties of InP etching and presents new conditions for high-aspect-ratio dry etching of PhCs in InP heterostructure [78]. 2-D PhC planar waveguides (W3) are characterised in Chapter 4. A new method of defining propagation losses in PhC waveguides via the Fourier transform technique is presented. Propagation losses of 1.8 dB/mm were measured [79]. Chapter 5 presents electro-optic tunable 1-D PhCs filters. Two different methods of reverse and forward biasing of microcavities [80, 81] are compared and their capabilities and limitations highlighted. Conclusions and prospects for improving the tunability of these devices are given in Chapter 6.

References

- [1] J-P. Laude, *DWDM: fundamentals, components, and applications*, Artech House, Boston, London, 2002.
- [2] S. J. B. Yoo, "Wavelength conversion technologies for WDM network applications," *J. Lightwave Tech.*, vol. 14, pp. 955-966, June 1996.
- [3] M. K. Smit, "Now focusing and dispersive planar component based on an optical phased array," *Electron. Lett.*, vol. 24, pp. 385-386, Mar 1988.
- [4] Q. Wang, J. Lu, and S. He, "Optimal design method of a low-loss broadband Y branch with a multimode waveguide section," *Appl. Opt.*, vol. 41, pp. 7644-7649, Dec 2002.
- [5] P. D. Trinh, S. Yegnanarayanan, and B. Jalali, "Integrated optical directional couplers in silicon-on-insulator," *Electron. Lett.*, vol. 31, pp. 2097-2098, Nov 1995.
- [6] M. R. Amersfoort, J. B. D. Soole, H. P. Leblanc, N. C. Andreadakis, A. Rajhel, and C. Caneau, "Passband broadening of integrated arrayed waveguide filters using multimode interference couplers," *Electron. Lett.*, vol. 32, pp. 449-451, Feb 1996.
- [7] Meint K. Smit and Cor van Dam, "PHASAR-Based WDM-Devices: Principles, Design and Applications," *IEEE J. Select. Topics Quantum Electron.*, vol. 2, pp. 236-250, June 1996.
- [8] C. Dragone, "An NxN optical multiplexer using a planar arrangement of two star couplers," *IEEE Photon. Technol. Lett.*, vol. 3, pp. 812-815, Sept 1991.
- [9] B. Glance, I. P. Kaminow, and R. W. Wilson, "Applications of the integrated waveguide grating router," *J. Lightwave Technol.*, vol. 12, pp. 957-962, June 1994.
- [10] A. A. M. Staring, L. H. Spiekman, C. van Dam, E. J. Jansen, J. J. M. Binsma, M. K. Smit, and B. H. Verbeek, "Space-switching 2.5 Gbit/s signals using wavelength conversion and phased array routing," *Electron. Lett.*, vol. 32, pp. 377-379, Feb 1996.
- [11] C. Joergensen, S.L. Danielsen, T. Durhuus, B. Mikkelsen, K.E. Stubkjaer, N. Vodjdani, F. Ratovelomanana, A. Enard, G. Glastre, D. Rondi, and R. Blondeau, "Wavelength conversion by optimized monolithic integrated Mach-Zehnder interferometer," *IEEE Photon. Technol. Lett.*, vol. 8, pp. 521-523, Apr 1996.

- [12] H. K. Tsang, M. W. Mak, L. Y. Chan, J. B. D. Soole, C. Youtsey, and I. Adesida, "Etched cavity InGaAsP/InP Waveguide Fabry-Perot filter tunable by current injection" *J. Lightwave Technol.*, vol. 17, pp. 1890-1895, Oct 1999.
- [13] T. E. Murphy, J. T. Hastings, and H. I. Smith, "Fabrication and Characterization of Narrow-Band Bragg-Reflection Filters in Silicon-on-Insulator Ridge Waveguides," *J. Lightwave Technol.*, vol. 19, pp. 1938-1942, Dec 2001.
- [14] B. Jalali, S. Yegnanarayanan, T. Yoon, T. Yoshimoto, I. Rendina, and F. Coppinger, "Advances in Silicon-on-Insulator Optoelectronics," *IEEE J. Select. Topics Quantum Electron.*, vol. 4, pp. 938-947, Nov/Dec 1998.
- [15] A. Jourdan, F. Masetti, M. Garnot, G. Soulage, and M. Sotom, "Design and implementation of a fully reconfigurable all-optical crossconnect for high capacity multiwavelength transport networks," *J. Lightwave Technol.*, vol. 14, pp. 1198-1206, Jun 1996.
- [16] H.J.S. Dorren, X. Yang, D. Lenstra, H. de Waardt, G.D. Khoe, T. Simoyama, H. Ishikawa, H. Kawashima, and T. Hasama, "Ultrafast refractive-index dynamics in a multi-quantum-well semiconductor optical amplifier," *IEEE Photon. Technol. Lett.*, vol. 15, pp. 792-794, June 2003.
- [17] J. Yu, X. Zheng, C. Peucheret, A. T. Clausen, H. N. Poulsen, and P. Jeppesen, "All-Optical Wavelength Conversion of Short Pulses and NRZ Signals Based on a Nonlinear Optical Loop Mirror," *J. Lightwave Technol.*, vol. 18, pp. 1007-1017, July 2000.
- [18] N. El Dahdah, G. Aubin, J.-C. Harmand, A. Ramdane, A. Shen, F. Devaux, A. Garreau, and B.-E. Benkelfat, "Ultrafast InGaAs/InGaAlAs multiple-quantum-well electro-absorption modulator for wavelength conversion at high bit rates," *App. Phys. Lett.*, vol. 84, pp. 4268-4270, May 2004.
- [19] P. Tayebati, P.D. Wang, D. Vakhshoori, and R.N. Sacks, "Widely tunable Fabry-Perot filter using Ga(Al)As-AlOx deformable mirrors," *IEEE Photon. Technol. Lett.*, vol. 10, pp. 394-396, Mar 1998.
- [20] J. Pfeiffer, R. Riemenschneider, J. Peerlings, R. Genovese, M. Aziz, H. E. Goutain, K. Unzel, W. Görtz, G. Böhm, M. C. Amann, P. Meissner, and H. L. Hartnagel, "InGaAs bulk micromachined tunable Fabry-Perot filter for dense WDM systems," *Materials Science in Semic. Processing*, vol. 3, pp. 409-412, Dec 2000.

- [21] J. Daleiden, V. Rangelov, S. Irmer, F. Romer, M. Strassner, C. Prott, A. Tarraf and H. Hillmer, "Record tuning range of InP-based multiple air-gap MOEMS filter," *Electron. Lett.*, vol. 38, pp. 1270-1271, Oct 2002.
- [22] M. Hoffmann and E. Voges, "Bulk silicon micromachining for MEMS in optical communication systems," *J. Micromech. and Microengin.*, vol. 12, pp. 349-360, June 2002.
- [23] G. Pucker, A. Mezzetti, M. Crivellari, P. Bellutti, and A. Lui, "Silicon-based near-infrared tunable filters filled with positive or negative dielectric anisotropic liquid crystals," *J. Appl. Phys.*, vol. 95, pp. 767-769, Jan 2004.
- [24] S. Toyoda, N. Ohba, T. Kitou, T. Kurihara, and T. Maruno, "Wide tuning range and low operating power AWG-based thermo-optic wavelength tunable filter using polymer waveguides," *Electron. Lett.*, vol. 37, pp. 1130-1132, Aug 2001.
- [25] S. Matsuo, Y. Yoshikuni, T. Segawa, Y. Ohiso, and H. Okamoto, "A widely tunable optical filter using ladder-type structure," *IEEE Photon. Technol. Lett.*, vol. 15, pp. 1114-1116, Aug 2003.
- [26] S. J. Choi, Z. Peng, Q. Yang, S. J. Choi, and P. D. Dapkus, "Tunable microdisk resonators vertically coupled to bus waveguides using epitaxial regrowth and wafer bonding techniques," *Appl. Phys. Lett.*, vol. 84, pp. 651-653, Feb 2004.
- [27] R. Grover, T. A. Ibrahim, S. Kanakaraju, L. Lucas, L. C. Calhoun, and P.-T. Ho, "A tunable GaInAsP-InP optical microring notch filter," *IEEE Photon. Technol. Lett.*, vol. 16, pp. 467-469, Feb 2004.
- [28] C. A. Barrios, V. R. Almeida, R. R. Panepucci, B. S. Schmidt, and M. Lipson, "Compact Silicon Tunable Fabry-Perot Resonator with low power consumption," *IEEE Photon. Technol. Lett.*, vol. 16, pp. 506-508, Feb 2004.
- [29] J. E. Heebner, N. N. Lepeshkin, A. Schweinsberg, G. W. Wicks, R. W. Boyd, R. Grover, and P.-T. Ho, "Enhanced linear and nonlinear optical phase response of AlGaAs microring resonators," *Opt. Lett.*, vol. 29, pp. 769-771, Apr 2004.
- [30] L. H. Domash, M. Wu, N. Nemchuk, and E. Ma, "Tunable and Switchable Multiple-Cavity Thin Film Filters," *J. Lightwave Technol.*, vol. 22, pp. 126-135, Jan 2004.

- [31] S. Toyoda, N. Ooba, T. Kitoh, T. Kurihara, and T. Maruno, "Wide tuning range and low operating power AWG-based thermo-optic wavelength tunable filter using polymer waveguides," *Electr. Lett.*, vol. 37, pp. 1130-1131, Aug 2001.
- [32] B. Standish, "Optical-chip platform combines liquid crystals with nano-structures," *Lightwave*, Feb 2004.
- [33] S. J. B. Yoo, M. A. Koza, R. Bhat and C. Caneau, "1.5 μm asymmetric Fabry-Perot modulators with two distinct modulation and chirp characteristics," *Appl. Phys. Lett.*, vol. 72, pp. 3246-3248, June 1998.
- [34] S. John, "Strong localization of photons in certain disordered dielectric superlattices," *Phys. Rev. Lett.*, vol. 58, pp. 2486-2489, June 1987.
- [35] E. Yablonovitch, "Inhibited Spontaneous Emission in Solid-State Physics and Electronics," *Phys. Rev. Lett.*, vol. 58, pp. 2059-2062, May 1987.
- [36] J. D. Joannopoulos, R. D. Meade, and J. N. Winn, *Photonic crystals: molding the flow of light*, Princeton Univ. Press, 1995.
- [37] R. L. Chern, C. Chung Chang, Chien C. Chang, and R. R. Hwang, "Large full band gaps for photonic crystals in two dimensions computed by an inverse method with multigrid acceleration," *Phys. Rev. E*, vol. 68, p. 026704 (5), 2003.
- [38] E. Yablonovitch, T. J. Gmitter, R. D. Meade, A. M. Rappe, K. D. Brommer, and J. D. Joannopoulos, "Donor and acceptor modes in photonic band structure," *Phys. Rev. Lett.*, vol. 67, pp. 3380-3383, Dec 1991.
- [39] Johnson, "Guided modes in PhC slabs", *Phys. Rev. B*, vol. 60, pp. 5751-5758, Aug 1999.
- [40] S. Olivier, H. Benisty, C. J. M. Smith, M. Rattier, C. Weisbuch, and T. F. Krauss, "Transmission properties of two-dimensional photonic crystal channel waveguide," *Optical and Quantum Electronics*, vol. 34, pp. 171-181, Jan/Mar 2002.
- [41] E. Yablonovitch, T. J. Gmitter, and K. M. Leung, "Photonic band structure: The face-centered-cubic case employing nonspherical atoms," *Phys. Rev. Lett.*, vol. 67, pp. 2295-2298, Oct 1991.
- [42] S. Y. Lin, J. G. Fleming, D. L. Hetherington, B. K. Smith, R. Biswas, K. M. Ho, M. M. Sigalas, W. Zubrzycki, S. R. Kurtz and Jim Bur, "A three-dimensional photonic crystal operating at infrared wavelengths," *Nature*, vol. 394, pp. 251-253, July 1998.

- [43] Alfons van Blaaderen, R. Ruel, and P. Wiltzius, "Template-directed colloidal crystallization," *Nature*, vol. 385, pp. 321-324, Jan 1997.
- [44] O. D. Velev, P. M. Tessier, A. M. Lenhoff, and E. W. Kaler, "A class of porous metallic nanostructures," *Nature*, vol. 401, p. 548, Oct 1999.
- [45] P. Lodahl, A. Floris van Driel, I. S. Nikolaev, A. Irman, K. Overgaag, D. Vanmaekelbergh, and W. L. Vos, "Controlling the dynamics of spontaneous emission from quantum dots by photonic crystals," *Nature*, vol. 430, pp. 654-657, Aug 2004.
- [46] Y.-H. Ye, T. S. Mayer, I.-C. Khoo, I. B. Divliansky, N. Abrams, and T. E. Mallouk, "Self-assembly of three-dimensional photonic-crystals with air-core line defects," *J. Materials Chem.*, v.12, pp. 3637-3639, 2002.
- [47] M. Campbell, D. N. Sharp, M. T. Harrison, R. G. Denning, and A. J. Turberfield, "Fabrication of photonic crystals for the visible spectrum by holographic lithography," *Nature*, vol. 404, pp. 53-56, Mar 2000.
- [48] Y. Sugimoto, Y. Tanaka, N. Ikeda, Y. Nakamura, and K. Asakawa, " Low propagation loss of 0.76 dB/mm in GaAs-based single-line-defect two-dimensional photonic crystal slab waveguides up to 1 cm in length," *Opt. Express*, vol. 12, pp. 1090-1096, Mar 2004.
- [49] R. Ferrini, A. Berrier, L. A. Dunbar, R. Houdré, M. Mulot, S. Anand, S. de Rossi and A. Talneau, "Minimization of out-of-plane losses in planar photonic crystals by optimizing the vertical waveguide," *Appl. Phys. Lett.*, vol. 85, pp. 3998-3400, Nov 2004.
- [50] Y. Sugimoto, Y. Tanaka, N. Ikeda, T. Yang, H. Nakamura, K. Asakawa, K. Inoue, T. Maruyama, K. Miyashita, K. Ishida, and Y. Watanabe, "Design, fabrication, and characterization of coupling-strength-controlled directional coupler based on two-dimensional photonic-crystal slab waveguides," *Appl. Phys. Lett.*, vol. 83, pp. 3236-3238, Oct 2003.
- [51] Y. Sugimoto, N. Ikeda, N. Carlsson, K. Asakawa, N. Kawai and K. Inoue, "Fabrication and characterization of different types of two-dimensional AlGaAs photonic crystal slabs," *J. Appl. Phys.*, vol. 91, pp. 922-929, Feb 2002.
- [52] M.H. Shih, W.J. Kim, W. Kuang, J.R. Cao, H. Yukawa, S.J. Choi, J.D. O'Brien and W.K. Marshall, "Two dimensional photonic crystal Mach-Zehnder interferometers," *Appl. Phys. Lett.*, vol. 84, pp. 460-462, Jan 2004.

- [53] Y. Akahane, T. Asano, B.S. Song, and S. Noda, "High-Q photonic nanocavity in two-dimensional photonic crystal," *Nature*, vol. 425, pp. 944-947, Oct 2003.
- [54] Y. Akahane, T. Asano, B-S. Song, and S. Noda, "Demonstration of ultrahigh-Q photonic Nanocavity based on Gaussian-like optical confinement," *Proc. International Workshop on Photonic Electromagnetic Structures (PECS)*, Kyoto, Japan, 2004.
- [55] M. Notomi, A. Shinya, S. Mitsugi, E. Kuramochi, and H. -Y. Ryu, "Waveguides, resonators and their coupled elements in photonic crystal slabs," *Optics Express*, vol. 12, pp. 1551-1561, Apr 2004.
- [56] L. Raffaere, R. M. de La Rue, and T. Krauss, "Ultrashort in-plane semiconductor microlasers with high-reflectivity microstructured mirrors," *Opt. and Quantum. Electron.*, v. 34, pp. 101-111, Jan/Mar 2002.
- [57] M. Notomi, K. Yamada, A. Shinya, J. Takahashi, C. Takahashi, and I. Yokohama, "Extremely Large Group-Velocity Dispersion of Line-Defect Waveguides in Photonic Crystal Slabs," *Phys. Rev. Lett.*, vol. 87, p. 253902 (4), Dec 2001.
- [58] T. Baba, D. Mori, K. Inoshita, and Y. Kuroki, "Light localizations in photonic crystal line defect waveguides," *IEEE J. Select. Topics Quantum Electron.*, vol. 10, pp. 484-491, May/June 2004.
- [59] H. Kosaka, T. Kawashima, A. Tomita, M. Notomi, T. Tamamura, T. Sato, and S. Kawakami, "Superprism phenomena in photonic crystals: toward microscale lightwave circuits," *J. Lightwave Technol.*, vol. 17, pp. 2032-2038, Nov 1999.
- [60] L. Wu, M. Mazilu, T. Karle, and T. F. Krauss, "Superprism phenomena in planar photonic crystals," *IEEE J. Quantum Electron.*, vol. 38, pp. 915-918, July 2002.
- [61] R. Feced, M. N. Zervas, and M. A. Muriel, "An Efficient Inverse Scattering Algorithm for the Design of Nonuniform Fibre Bragg Gratings," *IEEE J. Quantum Electron.*, vol. 35, pp.1105-1115, Aug 1999.
- [62] A. Martinez, A. Garcia, P. Sanchis, and J. Marti, "Group velocity and dispersion model of coupled-cavity waveguides in photonic crystals," *J. Opt. Soc. Am. A*, vol. 20, pp. 147-150, Jan 2003.
- [63] U. Peschel, T. Peschel, and F. Lederer, "A compact device for highly efficient dispersion compensation in fiber transmission," *Appl. Phys. Lett.*, vol. 67, pp. 2111-2113, 1995.

- [64] H. Ichikawa and T. Baba, "Efficiency enhancement in a light-emitting diode with a two-dimensional surface grating photonic crystal," *Appl. Phys. Lett.*, vol. 84, pp. 457-459, Jan 2004.
- [65] P. Pottier, I. Ntakis, and R. M. De La Rue, "Photonic crystal continuous taper for low-loss direct coupling into 2D photonic crystal channel waveguides and further device functionality," *Optics Communications*, vol. 223, pp. 339-347, 2003.
- [66] D. Taillaert, W. Bogaerts, P. Bienstman, T.F. Krauss, P. Van Daele, I. Moerman, S. Verstyuyft, K. De Mesel, and R. Baets, "An out-of-plane grating coupler for efficient butt-coupling between compact planar waveguides and single-mode fibers," *IEEE J. Quantum Electron.*, vol. 38, pp. 949-955, July 2002.
- [67] E. A. Camargo, H. M. H. Chong, and R. M. De La Rue, "2-D Photonic crystal thermo-optic switch based on AlGaAs/GaAs epitaxial structure," *Opt. Express*, vol. 12, pp. 588-593, Feb 2004.
- [68] A. D. Bristow, J.-P. R. Wells, W. H. Fan, A. M. Fox, M. S. Skolnick, D. M. Whittaker, A. Tahraoui, T. F. Krauss, and J. S. Roberts, "Ultrafast nonlinear response of AlGaAs two-dimensional photonic crystal waveguides," *Appl. Phys. Lett.*, vol. 83, pp. 851-853, Aug 2003.
- [69] S. W. Leonard, H. M. van Driel, J. Schilling and R. B. Wehrspohn, "Ultrafast band-edge tuning of a two-dimensional silicon photonic crystal via free-carrier injection," *Phys. Rev. B*, vol. 66, p. 161102 (4), 2002.
- [70] F. Raineri, Crina Cojocar, P. Monnier, A. Levenson, R. Raj, C. Seassal, X. Letartre, and P. Viktorovitch, "Ultrafast dynamics of the third-order nonlinear response in a two-dimensional InP-based photonic crystal," *Appl. Phys. Lett.*, vol. 85, pp.1880-1882, Sep 2004.
- [71] T. Baba, M. Shiga, K. Inoshita and F. Koyama, "Carrier plasma shift in GaInAsP photonic crystal point defect cavity," *Electr. Lett.*, vol. 39, pp. 1516-1517, Oct 2003.
- [72] D. Scrymgeour, N. Malkova, S. Kim, and V. Gopalan, "Electro-optic control of the superprism effect in photonic crystals," *Appl. Phys. Lett.*, vol. 82, pp. 3176-3178, May 2003.
- [73] M. Soljacic, C. Luo, J. D. Joannopoulos, and S. Fan, "Nonlinear photonic crystal microdevices for optical integration," *Opt. Lett.*, vol. 28, pp. 637-639, Apr 2003.

- [74] M. Bahl, N. C. Panoiu, and R. M. Osgood, "Nonlinear optical effects in a two-dimensional photonic crystal containing one-dimensional Kerr defects," *Phys. Rev. E*, vol. 67, p. 056604 (9), 2003.
- [75] N. C. Panoiu, M. Bahl, and R. M. Osgood, Jr. "Ultrafast optical tuning of a superprism effect in nonlinear photonic crystals," *J. Opt. Soc. Am. B*, vol. 21, pp. 1500-1508, Aug 2004.
- [76] K. Busch and S. John, "Liquid-Crystal Photonic-Band-Gap Materials: The Tunable Electromagnetic Vacuum," *Phys. Rev. Lett.*, vol. 83, pp. 967-970, Aug 1999.
- [77] B. Maune, M. Loncar, J. Witzens, M. Hochberg, T. Baehr-Jones, D. Psaltis, and A. Scherer, "Liquid-crystal electric tuning of a photonic crystal laser," *Appl. Phys. Lett.*, vol. 85, pp. 360-362, Jul 2004.
- [78] M. V. Kotlyar, L. O'Faolain, R. Wilson, and T. F. Krauss, "High-aspect-ratio chemically assisted ion-beam etching for photonic crystals using a high beam voltage-current ratio," *J. Vac. Scien. Technol. B*, vol. 22, pp. 1788-1791, July 2004.
- [79] M. V. Kotlyar, T. Karle, M. D. Settle, L. O'Faolain, and T. F. Krauss, "Low-loss photonic crystal defect waveguides in InP," *Appl. Phys. Lett.*, vol. 84, pp. 3588-3590, May 2004.
- [80] M. V. Kotlyar, L. O'Faolain, A. Krysa and T. F. Krauss, "Electro-optic tuning of InP-based microphotonic Fabry-Perot filters," *J. Lightwave Technol.*, accepted for publications, 2005.
- [81] M. V. Kotlyar, L. O'Faolain, A. Krysa and T. F. Krauss, "Electrically tunable Multiquantum-Well InGaAsP/InGaAsP microphotonic filter," *IEEE Phot. Technol. Lett.*, vol. 17, pp. 837-839, Apr 2005.

Chapter 2

Fabrication of One- and Two-Dimensional Photonic Crystals

In this chapter we give a detailed description of passive two-dimensional and both active and passive one-dimensional photonic crystals. Fabrication processes such as photo- and electron-beam-lithography, reactive ion etching, and briefly chemically assisted ion-beam etching are studied.

2.1 Passive one-dimensional photonic crystals

Fabrication of modern optical and semiconductor devices requires the use of many complex systems such as chemically assisted ion beam etching (CAIBE), reactive ion etching (RIE), scanning electron microscope (SEM) (including e-beam lithography). This is particularly true in the case of photonic crystal structures. Devices of high quality have to be produced to allow manipulation of light on the submicron scale. The PhCs examined in this thesis consist of high-aspect-ratio features: sub-micron features etched to the depth of several microns. There are two crucial steps: firstly, submicron features require e-beam lithography for its definition, and, secondly, in order to achieve a required etch depth (up to 5 μm) of the narrow features, sophisticated etching technology such as CAIBE or inductive coupled plasma (ICP) etching is needed.

This chapter is dedicated to the description of the processes and the tools involved in fabrication of 1- and 2-D, passive and active PhCs in InP-based material. We present a description of processes such as e-beam lithography (for writing sub-micron features), RIE (for transferring patterns from soft e-beam resist to harder masks), photo-lithography (for optically writing 2-3 μm features such as waveguides) and briefly CAIBE (for deep and shallow etching, in greater details this process is described in Chapter 3).

All facilities for PhC fabrication are available at the University of St Andrews, apart from material growth (which was performed at the University of Sheffield).

The fabrication of the passive components of 1-D PhCs is a less complicated process than active and/or 2-D PhCs. Thus, we start from a description of these components¹.

2.1.1 Electron-beam lithography

Electron-beam (e-beam) lithography is required for fabrication of submicron features (100-400 nm features). Conventional optical photolithography is currently limited to $\sim 1 \mu\text{m}$ resolution due to the effects of diffraction. Although, new advanced optical photolithography machines are currently being developed that allow the fabrication of submicron features, these methods are still very expensive and not suitable for use at research level at this stage [1].

For e-beam writing, the machine used in our laboratory is a hybrid of a conventional scanning electron microscope (SEM) and electron-beam writing software and hardware. Purpose-built e-beam writers are also available, giving the advantages of higher throughput and easier use. However, this hybrid machine is ideal for research purposes and offers the flexibility of double use for both inspection and lithography.

Typical electron beam exposure systems feature the following main parts: an electron gun, electron optical column (the beam-forming system, magnets), sample stage, vacuum system and a computer that controls all parts of the machine and transfers pattern information to the beam deflection coils (Fig. 1).

¹ Filters, described in Chapter 5, are referred to in this chapter as 1-D PhCs (active/passive).

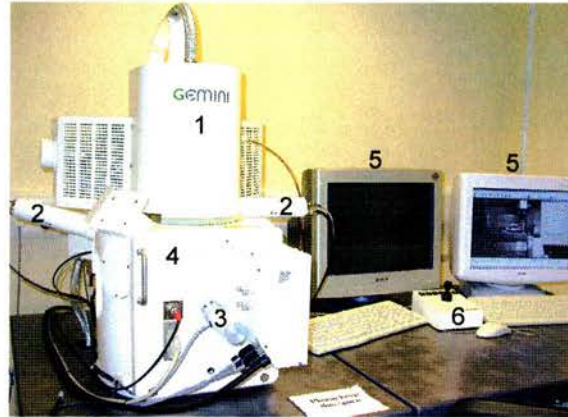


Fig. 1. The Hybrid LEO 1530 SEM/RAITH ELPHY electron-beam writer used for the work described in this thesis. The marked parts are as follows: 1) the beam-column, 2) the detectors, 3) the stage controller, 4) the main chamber, 5) the control computers, 6) joystick for stage control.

2.1.1.1 Electron-beam resists

There are two different types of e-beam resist- positive and negative [2]. For example, polymethylmethacrylate (PMMA) is a positive resist and SU-8 is negative. Both of these resists are polymers.

When positive resist is exposed, the polymer chains are broken; while chains are created in negative. These processes change the solubility of exposed parts. In the case of positive resist, the exposed parts will be dissolved in the developer, whereas for negative resist, they become less soluble and stay. For example, for writing the narrow slots (~ 100 nm) needed for filters described in Chapter 5, a positive resist (PMMA) was used. The use of negative resist will be mentioned later in this chapter with regards to insulation in active components.

The “clearing dose” [3] is an important parameter for e-beam writing. In order to explain this parameter, Fig.2 shows e-beam resist thickness as a function of the applied dose. The clearing dose (d_c) is the dose necessary to give complete clearing after development (when almost the entire thickness of the resist is removed).

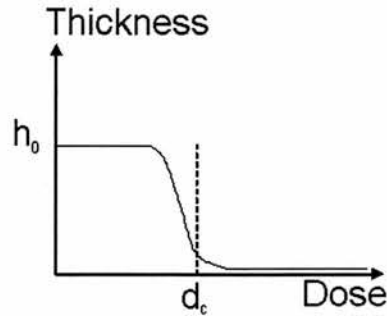


Fig. 2. The relationship between exposure dose and resist thickness.

The quality of the resist is crucial for e-beam writing. For different types of resist, different exposure doses are required. For example, base doses of 300-400, 100 and 1.5 $\mu\text{A s/cm}^2$ are required for exposure of FOX-12 (flowable glass, a negative resist), PMMA and SU-8 resists, respectively.

The substrate material is also important as different materials have different back-scattering coefficients and therefore lead to different background exposures. The correct dose should be found for each material and resist.

2.1.1.2 The proximity effect

As the electrons interact with the e-beam resist and the substrate, they scatter into small forward angles (by the resist) but some of them are scattered into large angles known as backscattering (by the substrate). This creates additional exposure of neighbouring sections, which is referred to as the proximity effect [4]. As the primary electrons slow down, they dissipate energy in the form of secondary electrons (which are knocked out of atoms in the substrate) with the energies below 50 eV. These electrons contribute little to the proximity effect (due to their low penetrating power) but are responsible for the bulk of the exposure of the resist. The small numbers of secondary electrons with energies of the order 1 keV, however, significantly contribute to the proximity effect and lead to secondary exposure on a 0.5-5 μm length scale, depending on the acceleration voltage.

In order to compensate for the proximity effect the pattern should be adjusted. Proximity correction basically consists of either an automatic or manual process of dose

distribution for patterns with interacting features. These are features that are situated at a distance of the backscattered electron range (2-5 μm) and thus electrons writing these features produce overexposure. Proximity correction is a vital feature when writing 1- and 2-D PhCs, in particular designs containing ridge waveguides. It was, thus, widely used in our work (see section 2.3).

2.1.1.3 Different methods of producing 100-nm wide lines

To realise the filters (described in Chapter 5), which are one of the main objects of this work, we choose Bragg mirrors consisting of 100 nm wide air-slots and 540 nm wide semiconductor regions. The wider the air regions, the greater the diffraction losses, so 100-nm air-slots were chosen as the practical minimum that can be etched deep enough to keep scattering losses to the substrate low. The ELPHY software package was used to design the pattern and to translate it into machine-code suitable for e-beam writing. In order to achieve high-quality 100 nm lines, we studied two different methods. These are referred to as “boxes” and “single-pixel lines” in the following.

Boxes:

When the design file contains a “box”, the software breaks this shape up into a grid of discrete exposure points that are then exposed in a snake-like motion. If one wants to write features of a given shape, one can use boxes of exactly these dimensions. However, in this case one has to work just above clearing dose. Increasing the dose can easily lead to overexposure, up to 150 nm. One of the disadvantages of working directly above the clearing dose is that rough edges may be produced. Using boxes of 30-50 nm less than desired feature size, smoother edges can be achieved as the overexposure smoothes the edges out.

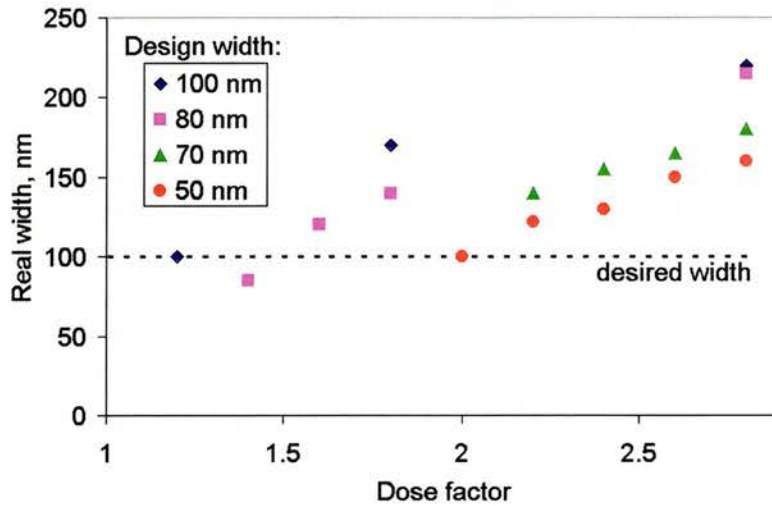


Fig.3. The width of exposed features versus dose factor (the base dose is $100 \mu\text{A s/cm}^2$) for boxes of different design sizes.

Fig. 3 shows the dependence of the slot width, obtained via exposing boxes of different sizes, on the dose applied. As one can see from this figure, different doses need to be used for boxes of different widths, in order to achieve a 100-nm wide exposed feature. For example, using 50 nm wide boxes, one should apply a dose of $200 \mu\text{A s/cm}^2$ to overexpose this feature to become 100-nm wide. Using a 100-nm wide box in the design a dose of $120 \mu\text{A s/cm}^2$ should be used to produce desired 100-nm feature. In this case, the dose of $120 \mu\text{A s/cm}^2$ is very close to the clearing dose, making edges undesirably rough.

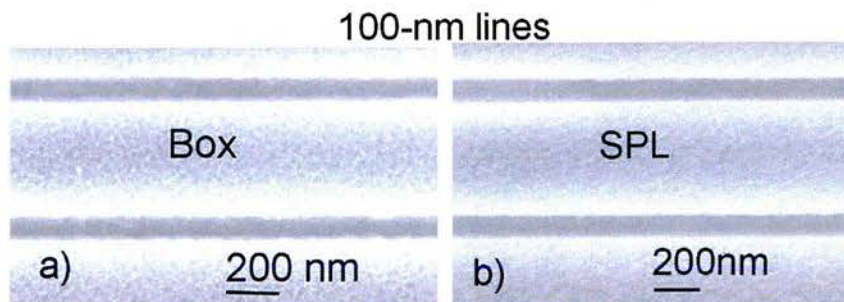


Fig. 4. Achieving 100-nm lines using box (a) and SPL (b) design.

In Fig. 4 (a) a 100-nm line was written using an 80-nm wide box, but roughness of the edges leaves much to be desired. There are several ways to get smoother edges. One way is to go to a design with boxes of smaller size (~50 nm) and to overexpose them; another way is to use single pixel lines instead (Fig. 4 b).

Single pixel line (SPL):

A SPL is a line of zero width. The machine writes it in a single pass of the desired length. Typically, the base dose for using SPL is 1000 $\mu\text{A}\cdot\text{s}/\text{cm}$. By varying the dose factor from 0.2 to 3, features of different sizes can be achieved using SPLs. Fig. 5 shows the width of exposed features for different dose factors using SPL and 80-nm boxes.

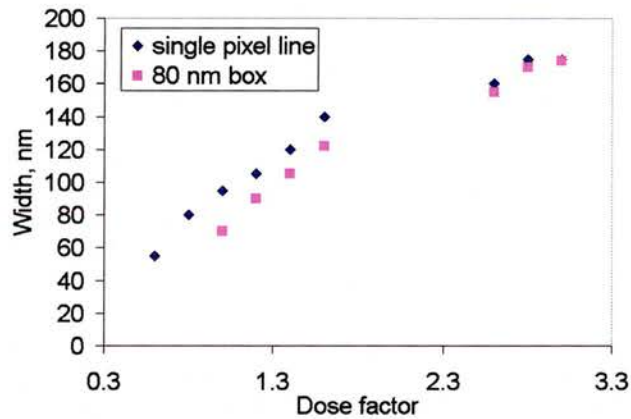


Fig. 5. The width of exposed lines (using SPLs and boxes) as a function of exposure dose. The base doses for SPL and boxes are 1000 $\mu\text{A}\cdot\text{s}/\text{cm}$ and 100 $\mu\text{A}\cdot\text{s}/\text{cm}^2$, respectively.

A base dose for a box is 100 $\mu\text{A}\cdot\text{s}/\text{cm}^2$. E.g. in order to reach a 90-100 nm feature size a dose factor of 1 and 1.2 should be applied for SPL and box design, respectively. The resultant lines are illustrated in Fig. 4, showing that smoother edges were obtained using the SPL design.

Fig. 6 shows a more detailed comparison of the quality of lines at different doses written via SPL or boxes (all from the same sample).

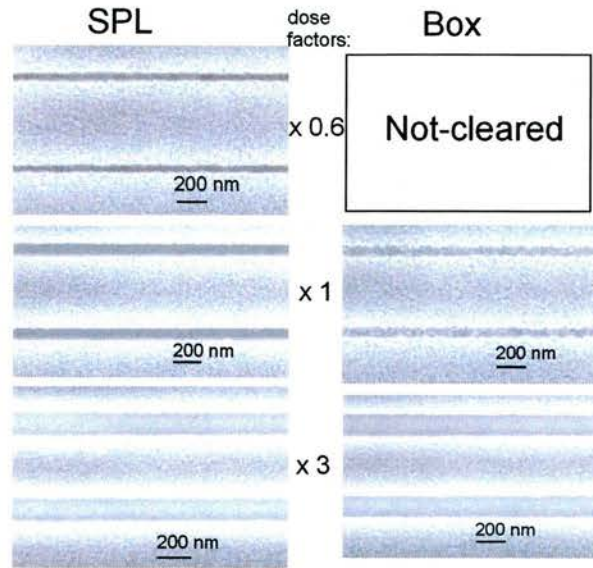


Fig. 6. SEM images of lines between 70 and 175 nm wide written using SPL and box designs. Base doses were $1000 \mu\text{A s/cm}$ and $100 \mu\text{A s/cm}^2$ for lines and boxes, respectively.

As one can see from this figure, SPL requires smaller doses compared with boxes to clear the resist and create smooth edges. When the dose factor reaches 3, both designs reach saturation with a line width of 175 nm, which does not increase much further for higher doses (see Fig. 5).

In conclusion, SPL allows better control over the feature size with reduced roughness, thus making it the preferred method.

Most of our filter gratings, characterised in Chapter 5, were hence written using SPL designs, resulting in 100-nm wide slots with smooth edges.

2.1.1.4 Summary of the e-beam writing process

The steps involved in e-beam writing of 1- and 2-D PhCs:

- 1) Spin PMMA on a top of the sample at 5000 rpm (revolutions per minute)
- 2) Bake on the hot-plate at 180°C for 5 minutes
- 3) Repeat for a second layer of the PMMA (the second layer of the PMMA is necessary in order to reach the necessary thickness of 200-300 nm for dry etch transfer into the SiO_2 hard mask)

- 4) Prepare suitable design using ELPHY software
- 5) Expose using the desired design using e-beam writing system
- 6) Develop the sample for 30 sec in IMBK developer, rinse in isopropanol and blow dry with nitrogen.

2.1.2 Reactive ion etching

Reactive Ion Etching (RIE) [5] was one of the first plasma etching techniques to be developed. RIE is a general-purposes technique used in the semiconductor industry but its possibilities are limited for the production of high-aspect-ratio PhC features. The main problem of an RIE system is the absence of independent control of ion-energies and plasma. In our process, we use RIE for the pattern transfer from resist to mask. Using appropriate chemistries, RIE is used in various applications, including etching of semiconductors, SiO₂ and resists. RIE uses kinetically assisted chemical etching and can produce high directionality.

A schematic view of an RIE system is presented in Fig. 7. The source used in an RIE system consists of a parallel plate design where one plate is grounded (Fig.7. part 1) and another is radio-frequency (RF) powered, giving an oscillating voltage at radio frequency (Fig.7 part 2). The sample (Fig.7 part 3) is directly placed on the oscillating electrode. A pipe in the shape of a ring (Fig.7 part 4) introduces various gases (Ar, CHF₃, SF₆, O₂, H₂, etc) inside the chamber. Under correct conditions of applied power and gas pressure, the plasma ignites (Fig.7 part 5).

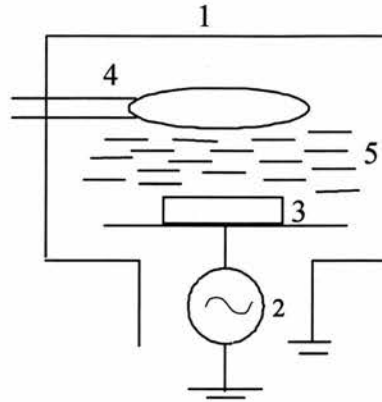


Fig. 7. A schematic view of the RIE system: 1- chamber, 2-RF power, 3- sample, 4-gas pipe, 5- plasma.

Different gas types, RF powers and chamber pressures give control over the etching conditions. Increasing the RF power (leads to higher plasma density) increases the etch rate via increased physical sputtering.

As PMMA is relatively soft as an etch mask and erodes very quickly during CAIBE, the pattern has to be transferred into a hard mask. In our case, SiO₂ is chosen as a hard mask, which was deposited using plasma enhanced chemical vapour deposition (PECVD) [6] at the University of Glasgow. The transformation process is performed via RIE using CH₃ chemistry. The PMMA etch rate during RIE is slightly lower than that of SiO₂ in CHF₃ environment, making mask transformation possible. Typical etch rates of SiO₂ experienced during our experiments are between 15-20 nm/min.

After a pattern is transformed into the SiO₂ layer (typically of 200-300 nm thickness) the remaining layer of PMMA can be dissolved in acetone.

2.1.3 Chemically assisted ion beam etching

The next step in our fabrication process is CAIBE, where the pattern will be deeply etched (3-5 μm) into semiconductor using a SiO₂ mask of a 300-nm thickness. From our experience, we know that even after etching holes as deep as 5 μm, there is still some SiO₂ mask is left (around 50-100 nm) which allows us to use the remaining SiO₂ as an etch mask for the shallow etching of waveguides.

Details of deep etching of air-slots are given in the next chapter. Here we summarize the fabrication of slots processes by a schematic diagram presented in Fig. 8.

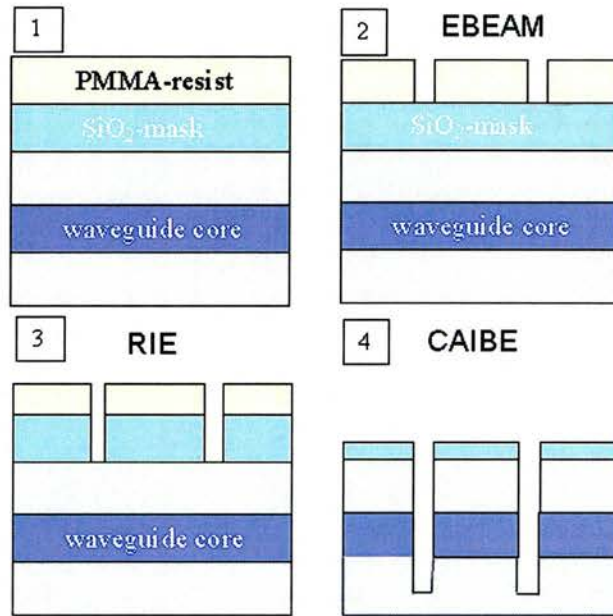


Fig. 8. Air-slots fabrication: 1) PMMA is spun on top of a SiO₂ mask, 2) E-beam exposure and development of a pattern in PMMA, 3) RIE pattern transfer into SiO₂ mask
4) CAIBE etching of pattern in semiconductor.

Let us consider some specific features of shallow etching in this section. The main difference between narrow slots (100 nm) and waveguide (3-10 μm) etching is the amount of gas (Cl₂) used. It has been noticed that for the etching of broad areas, a higher amount of Cl₂ is required during etching. This is obviously connected with the amount of semiconductor that has to be etched away. In the case of broad areas (more than a micron wide), a higher amount of chemical reactions is needed to produce the full chemical reaction. Otherwise, portions of the etched semiconductor are deposited back on the etched surface creating “grass”-like features. Therefore, the Cl₂ flow has to be increased up to 5 sccm (standard cubic centimetres per minute) in comparison with the 1 sccm used for high-aspect-ratio features (see Chapter 3).

Another difference between waveguide etching and slot etching is the etch depth. As we describe in Chapter 5, a shallow etch depth of around 200-700 nm depending on

the waveguide layout and ridge width is required to create single-mode waveguides. This small depth means that etching of deep filter-slots and waveguide ridges has to be carried out in two separate steps.

High-aspect ratio etching conditions generate a 350 nm/min etch rate. Hence, the required accuracy for shallow etching of 50 nm becomes difficult to achieve. In order to minimize the etch rate (with the amount of chlorine greatly increased), the beam current and substrate temperature were lowered down to 8 mA and 165° C, respectively. This reduced the etch rate to 150 nm/min. A cross-section image of a 5- μm wide shallow etched waveguide is presented in Fig. 9. The sample was etched for 2 minutes at 1200 V, 8 mA, 165° C and 5 sccm of Cl_2 , achieving a depth of ~ 300 nm.

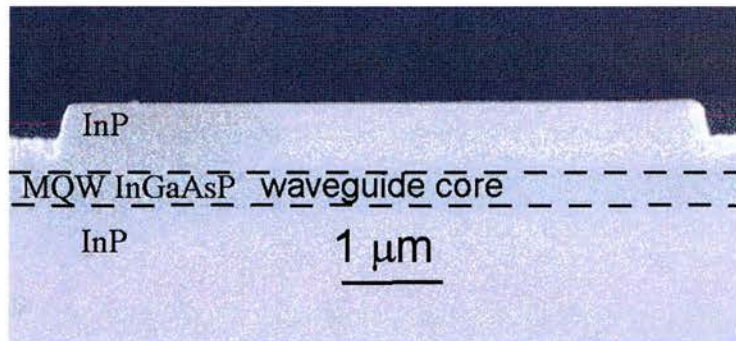


Fig. 9. A SEM image of a WG cross-section. The resultant etch depth is 300 nm. This etch depth is sufficient to keep this 5- μm wide WG (with a core size of 380 nm) single-moded.

As we mentioned above, SiO_2 is a protective mask for both cases of deep and shallow etching, but in order to create the waveguides in SiO_2 , optical photolithography is used.

2.1.4 Photolithography process

Optical photolithography is the most common and frequently used way of producing patterns for semiconductor photonic components. The resolution of the most

common optical photolithography systems is limited by diffraction of the light used for an exposure and is around 1-2 microns.

In our process, photolithography was mainly used for patterning waveguide regions, insulation pads and contact pads (thus for all features bigger than 2 μm). In order to carry out the patterning with photolithography, photo-masks were designed using the ELPHY software package and then generated at the University of Glasgow.

The typical process flow is as follows: 1818 photo-resist is spun on the surface of the wafer at 5000 revolutions per minute during one minute. Then, in order to drive off the solvent we heat the sample for 1 minute at 100° C. The thickness of the film is about 1.8 μm . For good quality photolithography, good contact between mask and wafer is required in order to minimise diffraction. The pattern can be over/underexposed, resulting in rounded edges and increased/decreased width of exposed features, respectively. Thus the exposure time for a given type or thickness of photo-resist, material and source lamp needs to be found. Typical exposure times for our process are around 20 seconds. Exposed portions are then dissolved in the developer MF-319 leaving, areas unprotected by photo-resist. In order to transfer the waveguide pattern into the SiO₂ mask, an RIE step is used. As a final step, CAIBE is performed for shallow etching of waveguide trenches. If we do not wash the photo-resist away after RIE in acetone, it can serve as a protection layer above the etched (unprotected by the SiO₂ mask) air-slots during the second CAIBE. The only problem of using the photo-resist is that it becomes permanent (cross-linked) at temperatures above 160° C (the minimal temperatures for InP etching). Thus a sample on which photo-resist has been cross-linked after CAIBE must be etched in O₂ environment with RIE. This process removes any organic materials from the surface of the InP material and/or SiO₂ mask.

Next steps of photo-lithography were used to fabricate active devices described in the next section of this chapter.

2.2 Fabrication of active filters

All of the processes described above are necessary for active filter fabrication. In addition, the negative resist SU-8 was used as an insulation layer. SU-8 is sensitive to UV

and electron radiation, so it can be used for any of those processes. As it has already been mentioned, SU-8 is a negative resist, which means it is rendered unsolvable by exposure.

2.2.1 Insulation and contact pads fabrication

Two designs of contacts were used in this work: squares and “T-shaped” designs. A device with a “T-shaped” type contact is shown in Fig. 10. Insulation and contact pads were laid down using a photolithography process. SU-8 (for insulation) was spun and exposed, so it remained everywhere except on top of the waveguide, with some gaps left to account for alignment tolerances.

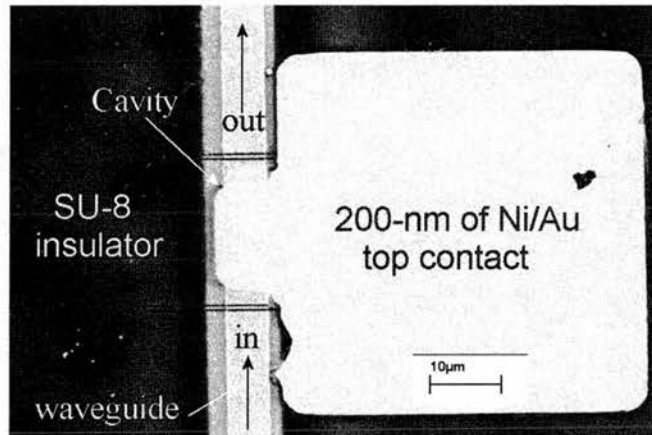


Fig. 10. An SEM image of a finished active filter. A “t-shaped” contact is used. All patterns were written using optical lithography with the exception of the air-slots that appear as narrow dark lines in the center of the waveguide.

In order to prepare the electrical contacts the following procedure was performed. The photo-resist SR-1818 was spun on top of the insulator and then soaked in chlorobenzene for 5-10 minutes. This renders the photo-resist surface harder and produces an under-cut when developed (see Fig. 11). The photo-resist was exposed using photo-lithography. The contact pad was smaller than the cavity to allow for tolerances of the lithographic process.

After the SR-1818 mask was prepared for contacts, the sample was put into an e-beam evaporator where 20/200 nm of Ni/Au for the top contact and 14/14/14/11/200 nm

of Au/Ge/Au/Ni/Au for the bottom contact were evaporated. A lift-off process was performed in order to leave Au on top of the sample as, sketched in Fig. 11. The specific undercut in a photo-resist (created after development and pre-soaking in chlorobenzene) depicted in Fig. 11 allows acetone to dissolve the remaining photo-resist, leaving only the gold on the surface of the semiconductor.

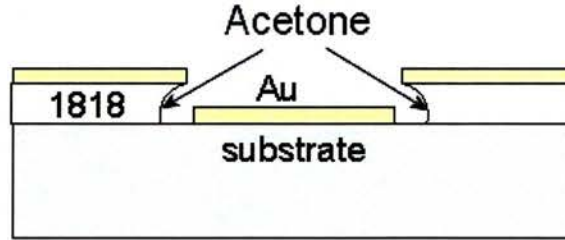


Fig. 11. A schematic view of the “lift-off” process. Acetone dissolves the photo-resist leaving only gold on top of the cavity.

Using photo-lithography to fabricate the structure, tolerances of only 2-3 μm were achieved. An alternative method of electron-beam lithography alignment was used for the fabrication of active devices with less tolerance.

2.2.2 Three-point alignment for the fabrication of active devices

This section is dedicated to multiple-step electron-beam lithography for writing complex active devices with improved accuracy (up to 100 nm alignment tolerance compared with 1-3 μm for photolithography). Another reason for using multiple e-beam lithography is that photolithography requires optical masks to be made up. Thus, e-beam lithography gives us more freedom for experimentation, as a design may be quickly changed as desired.

The main method used for multiple e-beam exposures is the technique of three-point alignment. This process consists of writing three alignment marks in three corners of the pattern area (700x800 μm). These marks have to be present on all layers of the pattern layout.

The marks used were complex-crosses with points in the centre (see Fig. 12). When crosses were successfully exposed, the centre of the small middle cross was used

for alignment purposes, otherwise, the centre of the big cross or any sharp corner of the squares can be used.

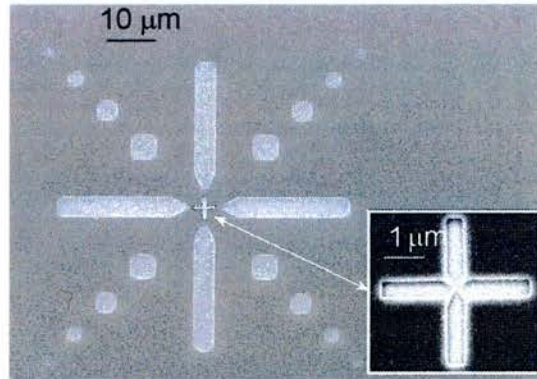


Fig. 12. An SEM image of a single alignment mark.

The idea of using alignment marks is as follows: a file is created containing the alignment marks and this part of the design is written first. Each successive stage is added sequentially choosing a new layer; in each step of the design 3 crosses on the surface of the sample have to be aligned with 3 crosses in the design (as the first step is deeply etched using CAIBE, it is possible to see crosses even underneath several layers of PMMA); the coordinate system is then defined according to the position of these crosses.

Following these principles, active filters were fabricated. Several series of 100-nm slots arranged into cavities of 20, 40, 80-μm sizes and alignment cross were e-beam written and etched using CAIBE to the depth of around 5 μm. The next step was to write the waveguide ridges on top of the slots, as illustrated in Fig. 13.

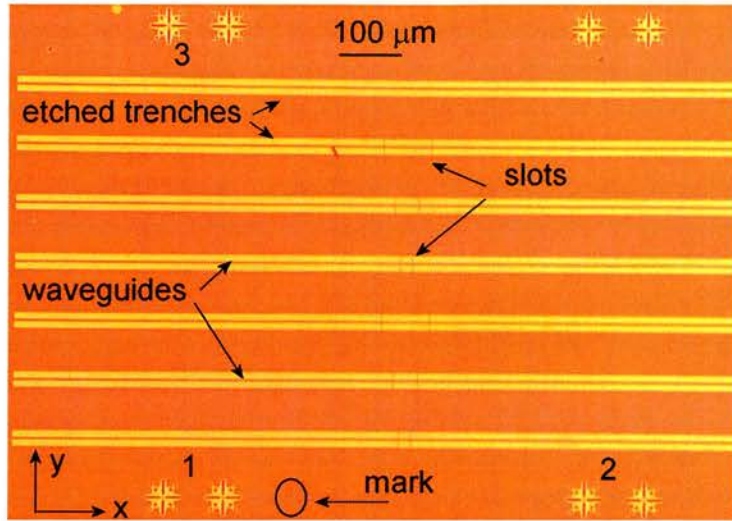


Fig. 13. Optical micrograph of the sample following a 3-point alignment. Filter slots and alignment marks were written first (using e.g. 1st layer in the software) and waveguides were aligned to them (using 2d layer).

As shown in Fig. 13, there are eight crosses in total, to give some redundancy in case of errors (sometimes crosses can be overexposed/underexposed/damaged). An additional mark was placed on the mask indicating the crosses closest to the origin in order to distinguish between different sets of crosses.

The right part of Fig. 14 illustrates that there can sometimes be imperfections in the waveguide area above the slots. This is connected with the difficulty of the resist (depending on viscosity) to evenly distribute over small deeply etched areas (air-slots region). As a consequence, the waveguides may not be written in the area of mirrors. This means that areas between the slots will be etched away during the shallow step, reducing the performance of the filter. This problem can be avoided by adjusting the thickness of e-beam resist via spinning at different speeds.

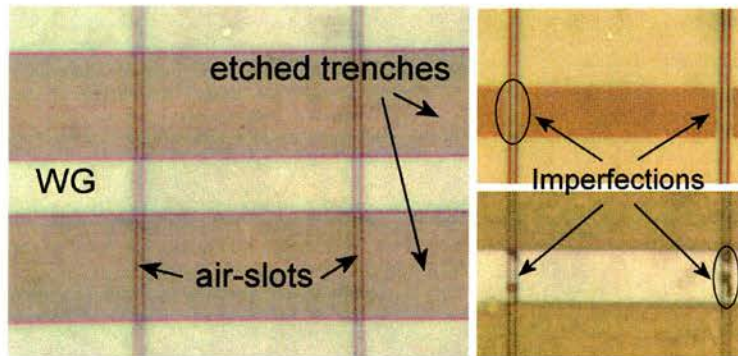


Fig. 14. A top-view of a filter cavity area following the 3 point alignment as well as deep and shallow etchings. The top and bottom right part of the figure illustrates fully removed and partially damaged areas, respectively, inside the Bragg mirrors after shallow etching as discussed in the text.

The next step consists of putting down the insulation. For this we use SU-8, because SU-8 can be used at 180-200° C and it forms a durable film. Since SU-8 works as a negative resist, we expose 120 by 100 μm insulation pads for each cavity, leaving small windows inside each filter cavity (Fig. 15).

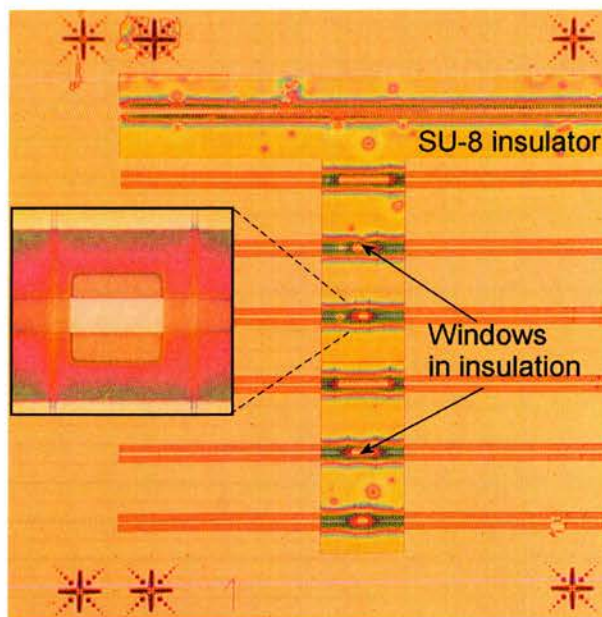


Fig. 15. A third stage of three-point alignment. Insulation pads were created. The inset shows a close-up image for a 20- μm long cavity with a window in the insulation.

The windows were reduced in size to account for alignment tolerances, which were not always as good as the ideal 100 nm.

As a final step, contact pads were e-beam written in a thicker than normal PMMA (in order to perform successful lift-off). The contact pads were designed in the shape of squares with sizes slightly less than those of the insulation pads (100 by 80 μm wide). Square-shaped contact pads were chosen due to the fragility of the T-shaped (see above) contacts of the initial designs. These used to burn out very easily at the interface of the broad and narrow parts due to resistive overheating. Developed PMMA has a specific undercut at its edges (in the same way as the optical resist has after chlorobenzene, see Fig. 9 above) making it possible to use it for lift-off of the metal, leaving Ni/Au contact pads on top of the sample after evaporation. A filter with a 20- μm cavity and evaporated Ni/Au contacts is presented in Fig. 16.

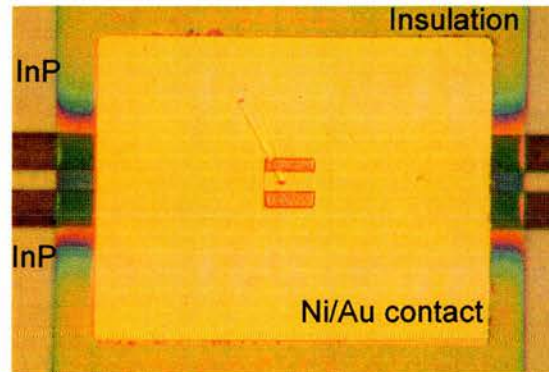


Fig. 16. A finished device. The picture illustrates the fourth step of 3 point alignment and successful lift-off after Ni/Au was evaporated on top of the sample. The dark orange areas in the middle of the cavity are regions that were left uninsulated to account for alignment tolerances, compare with the inset of figure 15 (note the probe mark on top of the contact).

In conclusion, in order to write active filters, e-beam lithography was performed 4 times, using the three-point alignment and both positive (thick and thin) and negative resists. A set of devices consists of filters with three different cavity sizes, i.e. 20-, 40- and 80- μm long. On the top and bottom of the devices, Ni/Au contacts were evaporated

using SU-8 as an electrical insulation layer. In order to characterise these devices, simple facet cleaving was performed creating final devices of the lengths between 400-1000 μm . The devices were then mounted on an aluminium block using silver epoxy for testing.

2.3 Two-dimensional photonic crystal fabrication

In the final section of this chapter, some specific aspects of 2-D PhCs fabrication will be described. The difficulties of creating high-aspect-ratio 2-D PhCs will be highlighted in the Chapter 3. This section will illustrate an importance of a proximity correction for fabrication of 2-D PhCs.

Proximity correction, which we briefly mentioned in the first section of this chapter, is vital for 2-D PhCs fabrication as they consist of many small features separated at distances below 1 μm (for such small distances the overlap between doses from the different features is high).

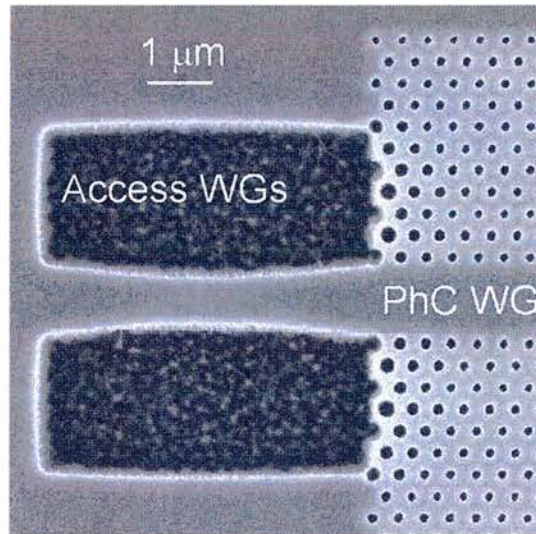


Fig. 17. A SEM image of 2-D PhC waveguide (WG) in InP-material after poorly applied proximity correction. The holes have different diameters depending on their position.

The PhC presented in Fig. 17 was proximity corrected but this proximity correction was not conducted well enough to distribute all the doses correctly. As one can see from the figure, the holes are biggest at the interface with the access waveguide. Obviously, as

the waveguide has the biggest area, its dose has the strongest effect on the surrounding small features. The holes at furthest edges have the smallest size. This happens because the holes at the edges have less neighbours and as a result receive a smaller overall dose. Therefore, the task of the proximity correction is to give the smallest doses to the holes at the interface with the WG and the biggest doses to the holes along the edges, while gradually distributing doses in middle. Fig. 18 is an illustration of successfully e-beam written 2-D PhCs in InP-based material, after correct proximity correction was achieved. A more detailed description of proximity correction and its parameters for fabricating 2-D PhCs in GaAs-based material is given in [6].

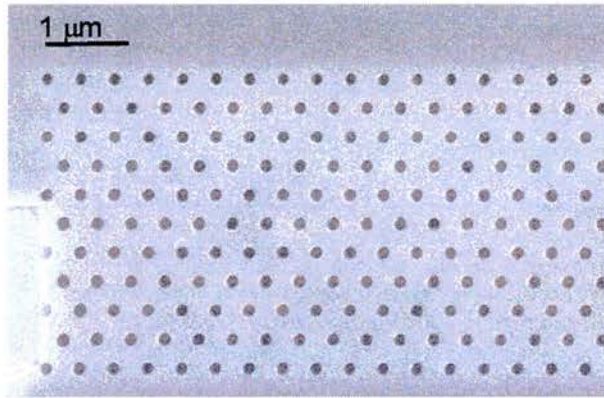


Fig. 18. An SEM image of 2-D PhCs in InP-material after successfully applied proximity correction. All holes have the same diameter.

2.4 Summary

As a conclusion to this chapter, a short resume of the work described here will be given. Fabrication of 1- and 2-D PhCs requires the use of state-of-the-art equipment. Some complex machines such as CAIBE, RIE, SEM with e-beam writing tool were used in this chapter. A description of the basics principles of operation of these machines was given. A step-by-step fabrication process of devices was described.

The fabrication of high quality 1- and 2-D PhCs in InP-based material was realised during this thesis. For example, features as small as 50-nm can be fabricated using our facilities. Proximity correction was applied in order to produce 2-D planar PhC

waveguides. More complicated active devices were also successfully fabricated using a several-stage e-beam alignment process.

The fabrication processes described here together with deep etching via CAIBE, which is presented in the next chapter, were used in order to produce the 2-D PhCs characterised in Chapter 4 and tunable filters in Chapter 5.

References

- [1] R. H. Stulen and D. W. Sweeney, "Extreme ultraviolet lithography," *IEEE J. Quantum. Electron.*, vol. 35, pp. 694-699, May 1999.
- [2] P. Rai-Choudhury, *The SPIE handbook on Microlithography, Micromachining and Microfabrication*, Chapter 2, SPIE-International society for optical engineering, 1997.
- [3] S. Buhling, F. Wyrowski, E-B. Kley, A. J. M. Nellissen, L. Wang, and M. Dirkwager, "Resolution enhanced proximity printing by phase and amplitude modulating masks," *J. Micromech. Microeng.*, vol. 11, pp. 603-611, Aug 2001.
- [4] M. Parikh, "Corrections to proximity effects in electron beam lithography. II. Implementation," *J. Appl. Phys.*, vol. 50, pp. 4378-4382, June 1979.
- [5] R. J. Shul and S. J. Pearton, *Handbook of Advanced Plasma Processing Techniques*, Chapter 11&12, Springer-Verlag, Berlin, Germany, 2000.
- [6] L. O'Faolain, "Fabrication of microstructures for ultra-short pulse production in semiconductor lasers," *PhD thesis*, University of St Andrews, 2005.

Chapter 3

Dry Etching of One- and Two-Dimensional InP- and GaAs-Based Photonic Crystals

In this chapter, chemically assisted ion beam etching is studied for etching InP- and GaAs-based one- and two-dimensional features. The importance of striking a good balance between chemical and physical components is highlighted. A chemically assisted ion beam etching regime for etching high-aspect-ratio photonic crystals is suggested. Using high beam voltage, low beam current etching conditions, deep ($\sim 5 \mu\text{m}$), vertical, low-roughness holes were produced. High-quality low-loss two-dimensional photonic crystal planar waveguides were fabricated using this regime.

N.B. The favourable high voltage low current regime was developed together with Dr. Rab Wilson and William Whelan-Curtin (L. O'Faolain).

3.1 Overview of advanced plasma processing etching systems

The fabrication technology of high-quality high-aspect-ratio features is one of the key technologies for realization of miniaturized photonic and optoelectronic components such as: PhC-based waveguides, lasers, cavities, and superprisms as well as conventional deeply etched Bragg reflectors. The fabrication process for producing 1- and 2-D PhCs has been well developed but some important refinements are still required.

Conventional reactive-ion etching (RIE) has been pushed to its limits; so more advanced plasma-processing technologies are required. The main principles of RIE system were given in Chapter 2. As more advanced alternatives to RIE systems, several different approaches have been explored: reactive-ion beam etching (RIBE), chemically assisted ion beam etching (CAIBE), inductively coupled plasma etching (ICP), and electron-cyclotron resonance (ECR) RIE. All these systems are described in great depth in [1]. Here we will only draw a brief comparison between the different approaches and discuss some features of these technologies.

RIBE and CAIBE derive their advantages over conventional RIE from introducing ion beams to add directionality to the etching process. In the RIBE mode, either only chemically reactive ions or a mixture of inert and reactive ions are used in the beam. In CAIBE, the ion-beam is usually inert (e.g. Ar), while a chemically reactive gas (e.g. Cl₂) is introduced near the target.

ICP and ECR-RIE also allows independent control of ion-energies and plasma properties compared to RIE. Such systems can combine high charge densities with low ion energies. The main difference in ICP and ECR-RIE systems is the way they sustain the plasma. The first system uses inductively coupled Radio Frequency (RF) power and the second one uses ECR microwave power.

CAIBE and ICP etching are some of the most effective and widely used etching processes for photonic crystals [2, 3]. The independent access to the plasma generation and etching conditions, provided during CAIBE and ICP, is critical for the etching of high-aspect-ratio features, as we will demonstrate below.

These technologies need to satisfy the following criteria: extremely anisotropic etching of heterostructures (low variation in etch rate and profile for different materials); high fidelity in pattern transfer (low mask erosion); good selectivity between the semiconductor and the masking layer; and low damage (minimal reduction in the internal quantum efficiency of any active layer in the heterostructure).

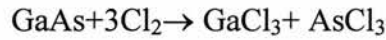
In photonic crystal structures, one of the major sources of losses (see Chapter 4) is insufficient etch-depth and/or non-vertical, rough walls. High-quality GaAs etching has already been achieved [4], whereas InP etching was to be developed to the same level. InP etching typically produces tapered holes [5], whereby the taper may compromise device performance. In addition, InP/InGaAsP heterostructures typically have lower confinement due to the lower refractive index contrast. As a result, the mode has a larger vertical extent and a greater depth ($\sim 3 \mu\text{m}$) is required to prevent coupling to substrate modes when working with InP [6].

In this chapter, we etch GaAs/AlGaAs and InP/InGaAsP “laser-like” waveguiding heterostructures using the CAIBE system.

3.2 Chemically assisted ion-beam etching system

3.2.1 Basics of operation

The material removal during CAIBE is a result of collisions of Argon ions accelerated by the voltage applied in a vacuum chamber. This process is aided by the introduction of chlorine, which reacts chemically with the semiconductor substrate. GaAs/InP will react with Cl₂ to form volatile products via the following chemical reactions, which in a somewhat simplified form are given by [1, 7]:



These reactions do not occur spontaneously, but require some activation energy, which can be supplied by an ion flux. It is important to note that InCl_x by-products are not volatile at room temperature as they require a very low vapour pressure of $\sim 10^{-8}$ Torr. To obtain high enough etch rate for InCl_x the substrate must be heated up to at least 150 °C [8].

During etching the material must be removed only from selected portions of the wafer. This is achieved by masking certain portions of the wafer with a mask (photoresist/SiO₂/SiN_x). That is, photo/e-beam lithography is used to create a pattern in the mask on the wafer (see Chapter 2). The wafer will be etched by CAIBE wherever it is exposed (unprotected by the mask).

In CAIBE, an ion beam is directed onto a sample in a reactive gas ambience (Cl₂) (Fig. 1). The ion energy, beam current, flow of the reactive gas, and substrate temperature can be controlled independently.

3.2.2 Special features of the machine used in our work

Our CAIBE system uses a 3-cm gridded broad-beam ion source, also known as a Kaufman-type ion source [9]. Two-grid graphite optics with argon gas is used. The emitter consists of the cathode and the anode. The ions are accelerated through the screen grid by the negative accelerator grid. The apertures of these two grids are precisely aligned to direct the beam towards the sample. A neutralizer filament adds electrons to the ion beam. These electrons offset the mutual repulsion of ions, a process that is called “charge neutralization”. Chlorine is supplied via the ring over the sample holder. A schematic view of the CAIBE system is presented in Fig.1.

This version of the source provides a high degree of beam-profile stability and reproducibility.

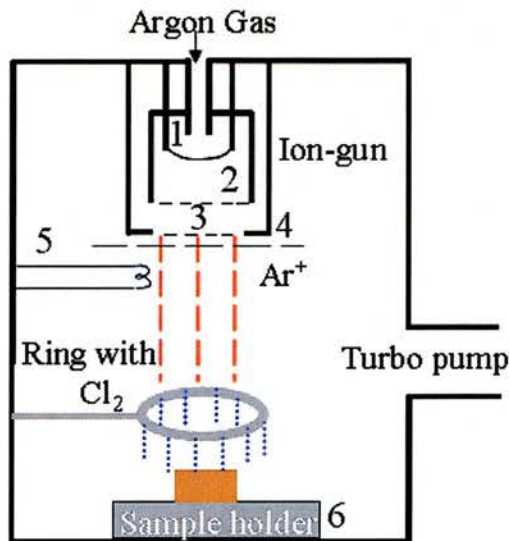


Fig. 1. A schematic view of the CAIBE system used in our work: 1-4 ion source; 1-cathode; 2-anode; 3-4-accelerator and screen grid; 5-neutralizer; 6-stage.

3.2.3 Nature of chemical/physical balance with respect to large features

Several characteristics of the dry etching technique are essential to the production of high quality features: particularly important are the etching selectivity between various materials, the etching rate and the aspect ratio. By controlling these components, as well as the chemical and ion fluxes, the etching characteristics can be determined.

Our main task was to achieve a high aspect ratio, which is so desirable for fabrication of photonic crystals. To achieve this aspect ratio, vertical and smooth sidewalls are necessary. In route to this goal, we met several problems but the reason for all these problems was the same— an incorrect balance between the physical and chemical components in the course of the etching. Fig. 2 shows the influence of these components on the etching process in the etching of large features, i.e. where the effect of neighbouring walls is negligible.

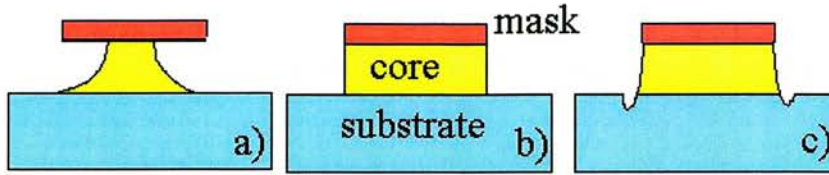


Fig. 2. A schematic view of the different etching profiles encountered in CAIBE: a) chemical, b) chemical-physical, c) physical.

So, according to Fig. 2, we get three different etching profiles in the etching process. Fig. 2 (a) shows an undercut profile that is symptomatic of a strong chemical (Cl_2 , T) etch component, thus etching process becomes isotropic. An overcut profile is presented in Fig. 2 (c). Together with the “ricochet” features at the wall’s base, they are symptoms of physical (argon sputtering) etching. The effect of “ricochet” results from the increased flux of ions at the trenches due to reflection from the side walls, and, perhaps, also from the material sputtered from the side wall onto the base of the hole. By carefully balancing the chemical and physical etching components, vertical smooth walls can be obtained (Fig. 2 b).

A GaAs-based material was used in the following section. Let us define the parameters allowing us to see which process (chemical or physical) is dominant in the etching process. The process pressure (2.7×10^{-4} mBar), the flow of chlorine (10 sccm=standard cubic centimetres per minute) and argon (5 sccm) as well as the beam current of 30 mA were kept constant for all the etches described in this section.

Fig. 3 shows the etching profile obtained for a beam voltage of 500 V. The shape of the profile indicates that for such a beam voltage the dominant component of the etching process was physical. The symptomatic “ricochet” feature can be easily seen at the bottom of the etched trench.

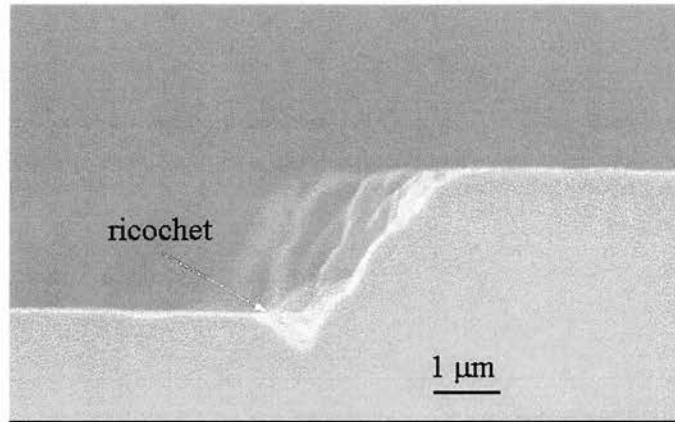


Fig. 3. A SEM image of the GaAs sample etched under the beam voltage of 500 V, $T=70^{\circ}\text{C}$.

Decreasing the ion energy (controlled by beam voltage) can correct for this effect. Using the beam voltage of 300 V it was possible to eliminate these defects and obtain vertical walls (Fig. 4). Both samples were etched at a substrate temperature of 70°C .

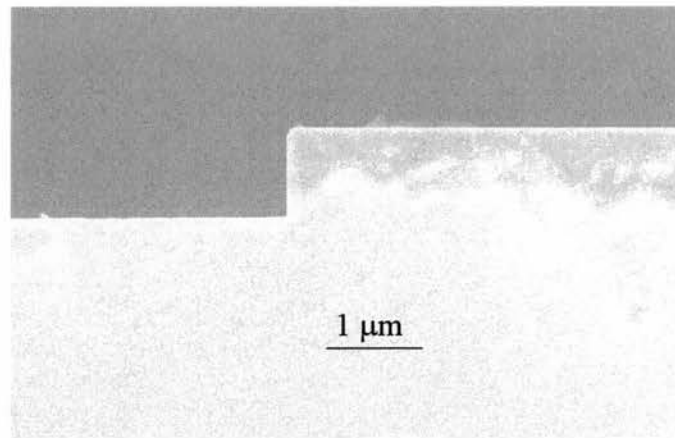


Fig. 4. A SEM image of the GaAs sample etched under the beam voltage of 300 V, $T=70^{\circ}\text{C}$

Increasing the temperature to 140°C , one can see that the chemical component begins to dominate the etching process, as depicted in Fig. 5. Chemical interaction means that excited particles from plasma react with the surface and form volatile reaction products, thus leading to isotropic etching.

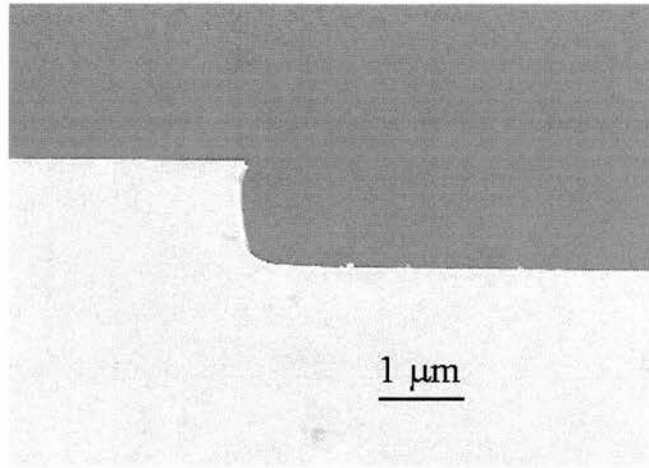


Fig. 5. A SEM image of the GaAs sample etched under the beam voltage of 300 V, $T= 140^{\circ}$ C.

Fig. 6 shows the profile obtained in AlGaAs/GaAs material, as an example of well balanced etching of big features.

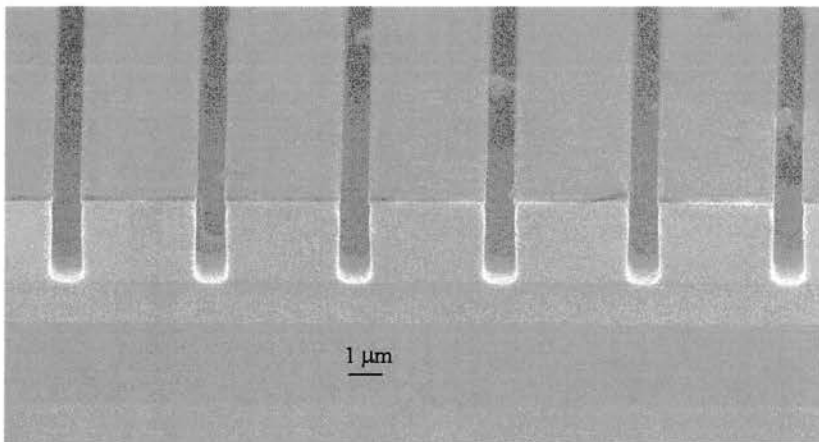


Fig.6. A SEM image of the GaAs sample etched under the beam voltage of 300 V, $T= 80^{\circ}$ C.

In this section, we have only adjusted the beam voltage and substrate temperature. The beauty of the CAIBE system is the number of parameters that may be independently adjusted (voltage, current, gas flow, temperature, pressure). In the next section we change the current and chlorine flow to great effect.

3. 3 High-voltage low-current etching regime

This section considers a new etching regime adapted for etching 2-D and 1-D PhCs features. This high voltage, low current etching regime turned out to be

extremely favourable for etching high aspect-ratio features. Deep holes can be achieved under such conditions, taking advantage of high semiconductor-mask selectivity. A comparison of etching performed with this CAIBE regime against other etching systems/regimes is presented at the end of this section.

3.3.1 Conditions for balanced etching process for high-aspect-ratio features

As we mentioned earlier, InP by-products (InCl_x) are not volatile at room temperature. Thus etching InP with chlorine has a threshold temperature of approx. 150°C . As a result, we heat the sample up to $185\text{-}220^\circ\text{C}$. This temperature is sufficient to allow the chemical etching to counter-balance the physical etching.

A waveguide heterostructure is shown in Fig. 7. Since etching of InP takes place at high temperature ($\sim 185^\circ\text{C}$; compare to $\sim 80^\circ\text{C}$ for etching of AlGaAs), the process is very sensitive to the amount of chlorine present. Therefore, we kept the chlorine flow low, i.e. between 0.9-1.7 sccm. This is more than 5 times lower than for etching the GaAs-based material mentioned above. The pressure in the chamber also becomes lower (1.6×10^{-4} mBar), making the process of removing InCl_x products from the etched holes easier than in the case with AlGaAs. This allows very high-aspect-ratio etching.

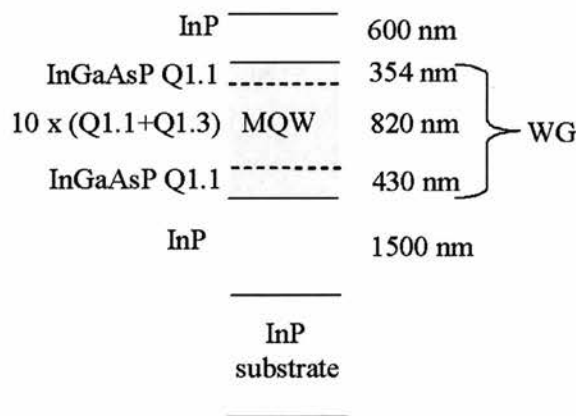


Fig. 7. A schematic view of a waveguide (WG) heterostructure with 10 wells used for etching high aspect-ratio features.

Thus, going to the regime of high temperature (210°C) and decreasing the chlorine flow to 1 sccm, while leaving the beam current and voltage at the same values

of 30 mA and 300 V, respectively, we initially obtain chemically over-etched side walls (Fig. 8 (a)). Decreasing the Cl_2 flow to 0.8 sccm partially eliminates the problem (Fig. 8 (b)), but the effect of “wobbling” remains.

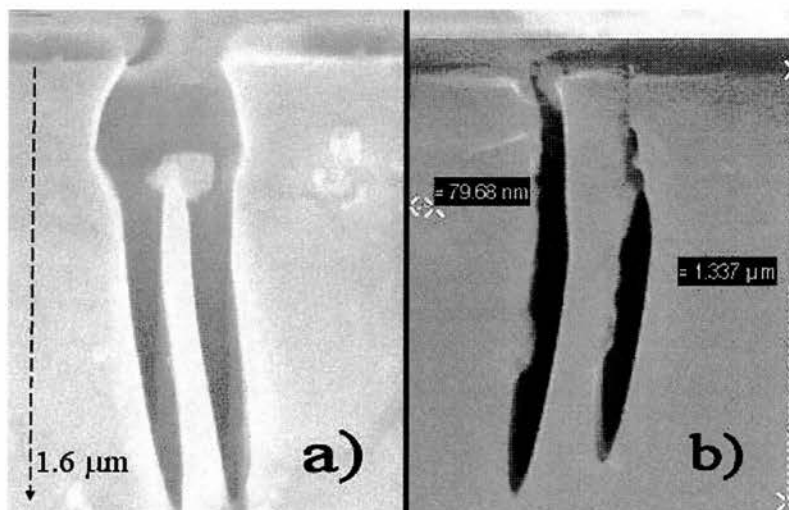


Fig. 8. SEM images of etched slots (~ 100 nm wide): a) chemically over-etched profile; b) strong “wobbling”, which is defined as poor etching directionality of high aspect ratio features in InP; the reason for this phenomenon is not fully understood.

Figure 9 (a) shows etching results for an InP-based sample with the following etching conditions: substrate temperature of 185°C , beam current of 30 mA, beam voltage of 900 V, and Cl_2 flow of 0.8 sccm. These conditions lead to a physically dominant etching process. This causes an overcut wall profile with widening at the top of the hole and a poorly formed hole bottom. By increasing the Cl_2 flow, the chemical and physical components of the etching process should become better balanced. However, we never managed to achieve a satisfactory profile with these conditions.

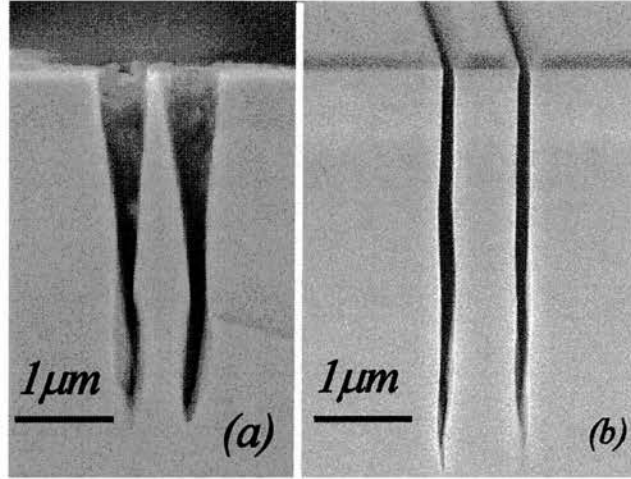


Fig 9. SEM images of one-dimensional features of 90-nm size in InP-based material: a) physically dominant etching process, b) a good chemical-physical balance; a 35:1 aspect ratio was achieved with mask selectivity of 18:1.

For high-quality, high-aspect-ratio etching, a different solution is therefore required. To this end, we modified the physical etching conditions.

In Fig. 9 (b), we reduced the beam current from 30 mA to 12 mA and increased the beam voltage from 900 V to 1200 V, thus entering a much more favourable etching regime. The flow of chlorine was increased up to 1.6 sccm. The reason for increasing the beam voltage was that “bending” was observed (also reported by Ferrini *et al.* [5]) at lower voltages (Fig. 8 (a, b)). It appears that a higher voltage gives a stronger directionality to the ion beam, thereby overcoming the tendency to etch sideways, which causes such a “bend.” The feature shown in Fig. 9 (b) is a 1-dimensional PhC in InP-based material with air slots of 90 nm and an etch depth of 3.5 μm (aspect ratio of 35:1). The conditions were the following: beam voltage- 1200 V, beam current- 12 mA, chlorine flow- 0.9 sccm, substrate temperature- 185 °C.

For GaAs etching of high-aspect-ratio features, a lower temperature is used (typically 120 °C), but otherwise, the same principles apply. In our experience, the margins for error in etching high verticality features are larger in GaAs than in InP, and the general quality is somewhat better (it is very rare to observe bending or wobbling in GaAs features, and tapering toward the bottom of the hole is more easily cured).

3.3.2 Semiconductor/mask selectivity

Once the process is correctly balanced, the main factor limiting the achievable depth of the etched holes is the mask etch rate relative to the material etch rate, i.e., the mask selectivity.

In Fig. 10, we show the relationship between the mask selectivity and the beam voltage. In this graph, we only plot points corresponding to a balanced etching process.

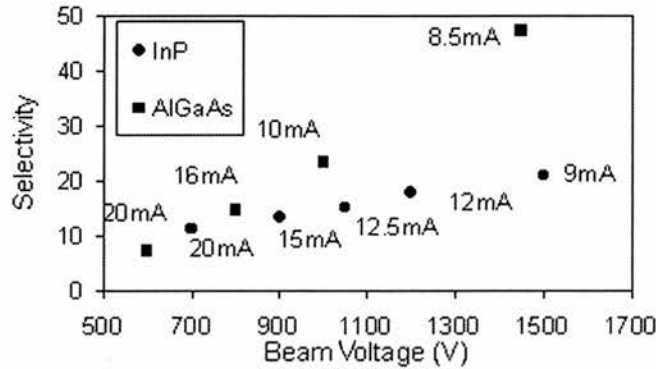


Fig. 10. The dependence of the semiconductor/mask selectivity on the beam voltage-current ratio for InGaAsP/InP and AlGaAs/GaAs materials. All values are given for 100 nm wide slots.

As can be seen, these points lie approximately on a straight line and fulfil the condition of constant beam power, i.e., a constant beam voltage-current product. For such constant beam power and balanced etching, a mask selectivity as high as 50:1 was achieved in AlGaAs/GaAs for air slots with a width of 100 nm. These conditions also enabled us to etch air slots as small as 40 nm in width to a depth of 1.1 μm with a semiconductor/mask selectivity of 27:1 (Fig. 11).

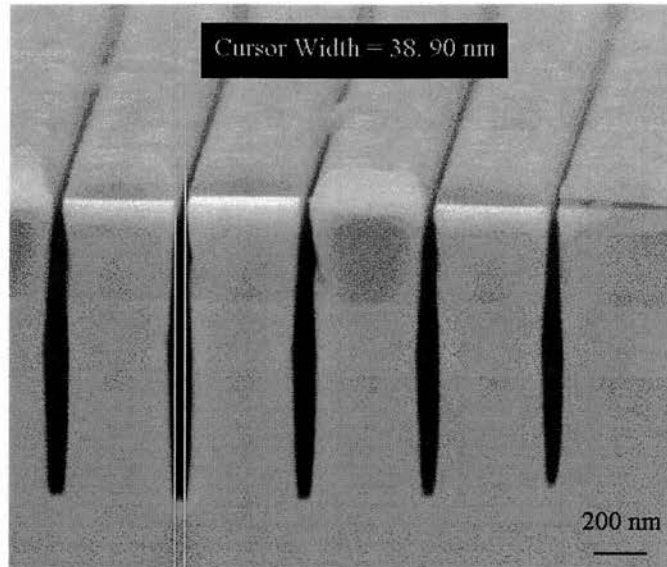


Fig. 11. An SEM image of extremely narrow (40 nm wide) slots in GaAs/AlGaAs etched to the depth of 1.1 μm with less than $\frac{1}{4}$ of the mask etched away, gaining a selectivity of 27:1. These features are slightly chemically over-etched [10].

To understand this increase in selectivity with beam voltage, we need to examine both the etch rate of the III-V material and that of the silica mask.

The silica mask etch rate is constant for a given beam voltage and current, i.e., it is independent of the chemical etching component, as it doesn't react with the chlorine. The III-V material etch rate, on the other hand, is strongly dependent on the chemical etch conditions (chlorine flow and temperature). Thus, the selectivity of chemically overetched features lies above the balanced line and that of chemically underetched (physically overetched) features lies below (Fig. 12).

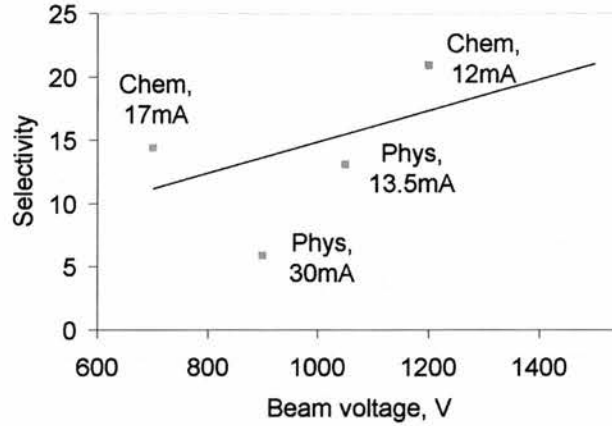


Fig. 12. The selectivity of chemically over-etched and physically over-etched holes with respect to an “in-balance” line (InP etching).

We believe that the observed improvement in selectivity for etching at a high voltage-current ratio is due to a hardening of the mask under the impact of high-energy ions. Fig. 13 shows a significant reduction in the silica mask etch rate with increasing beam voltage. We have also observed that the remaining silica mask after a CAIBE etch is more resistant to RIE than before. This is poorly understood- we assume that this hardening occurs as a consequence of the high-energy ion impact.

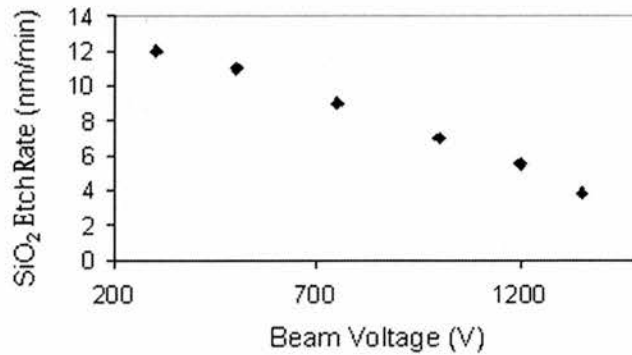


Fig. 13. The dependence of silica mask etch rate on the beam voltage. All other conditions were held constant.

The equivalent graph for the semiconductor, i.e., etch rate vs. beam voltage, is approximately flat. Due to the strong dependence of the semiconductor etch rate on

the physical-chemical balance, it is difficult to determine the semiconductor etch rate exactly, making a direct comparison between the two etch rates problematic.

What is clear, however, is that the selectivity increases with the beam voltage when the etch conditions are on the “balanced” line, as shown in Figs. 10 and 12.

We also observe that the etch rate (and selectivity) decreases with decreasing feature size (see Fig. 14). This is a well-documented phenomenon that is believed to be a form of RIE lag [11].

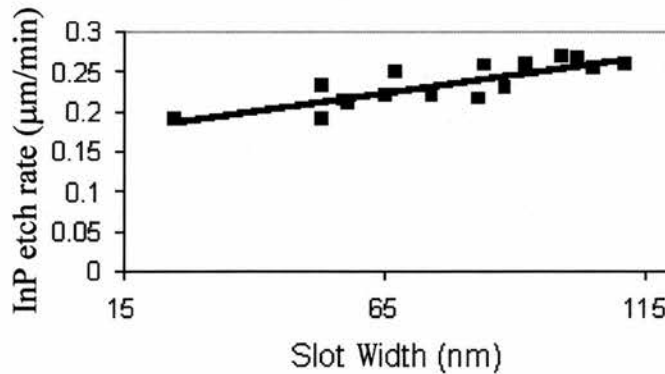


Fig. 14. The dependence of the InP etch rate on the hole size under optimized etching conditions. All measurements are taken from the same sample.

3.3.3 “Neck” formation

The formation of a “neck” [11] just below the surface in InP etching was observed at times (see Fig. 15). “Neck” formation takes place when the chemical component of the etching process is slightly in excess. The increased surface temperature due to heating by the ion beam, coupled with the effects of ions ricocheting off the mask edges, increases the isotropic etch rate in the vicinity of the surface. Even a small deviation from a good “chemical-physical” balance is enough for such a “neck” to be formed.

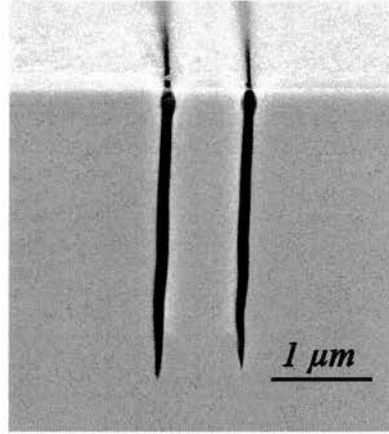


Fig. 15. A 100-nm feature-size etched in InP-based material. The “neck” observed at the top of the hole is due to a small “chemical-physical” unbalance.

The higher the amount of Cl_2 or the substrate temperature (with the rest of the parameters unchanged), the bigger “neck” is observed. In accordance with this argument, the “neck” shown in Fig. 15 could be easily removed by increasing the beam current from 8.5 mA to 9 mA, thus slightly increasing the amount of physical etching and returning to the perfect “physical-chemical” balance. This feature is rarely observed in GaAs.

3.3.4 Low sidewall roughness

One of the concerns with CAIBE is that the high ion energies lead to more violent impacts, resulting in increased sidewall roughness. We did not observe any such behaviour for the conditions described here.

In our case, due to the low beam current, we believe that there is a large ion-induced chemical-etching yield. The initial impact of an ion causes roughness, which is then largely erased by the chlorine, which reacts faster in the region of the impact due to the localized heating caused by the impact. The top part of figure 16 is a scanning electron microscope (SEM) image of an etched hole showing low sidewall roughness. Furthermore, the low measured propagation losses [12] of PhC devices etched using high beam voltage and low current proves that the sidewall roughness was not high. This agrees qualitatively with the results of Daleiden *et al.* [13], who show that CAIBE causes less damage than IBE. Thus, by extension, it is plausible that a strong chemical component may reduce damage caused by the physical component.

However, despite the smooth wall profiles observed in Fig 16, we can not determine the degree of damage produced by high energy ion impacts in terms of the electrical properties of material. However, we believe that the low-threshold narrow stripes ($\sim 5 \mu\text{m}$) quantum dot lasers in AlGaAs tested independently by S. Moore *et al.* [18] and fabricated using this high voltage low current regime indicate that the amount of this side wall damage is low.

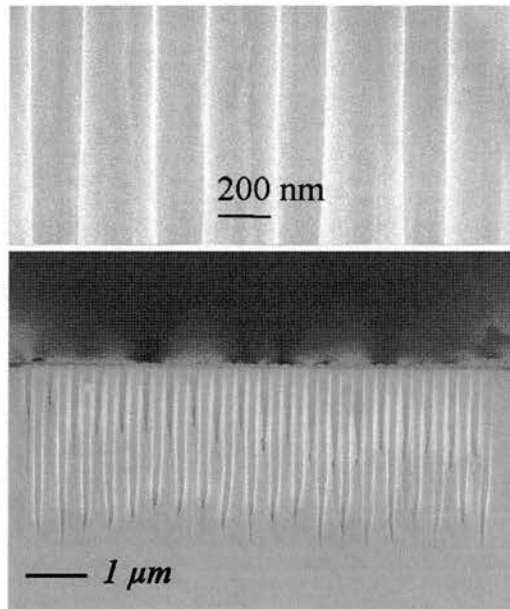


Fig. 16. SEM images of InGaAsP/InP photonic crystals etched under high-voltage conditions to a depth of $3.7 \mu\text{m}$ (a hole diameter of 195 nm). The top image demonstrates the low level of sidewall roughness of the PhCs.

3.3.5 Etching of two-dimensional photonic crystals

InGaAsP/InP and AlGaAs/GaAs 2-dimensional photonic crystals have also been etched successfully using these guidelines. GaAs-based PhCs were etched to a depth of $1.6 \mu\text{m}$ with a mask/semiconductor selectivity of 32:1 for a hole diameter of 200 nm . InP/SiO₂ mask etching ratios of 27:1 and 34:1 were achieved for 195-nm and

270-nm diameter holes, respectively, with corresponding hole depths of 3.5 μm and 5.5 μm , i.e., aspect ratios of 17:1 and 20:1 (Fig. 16, 17). The etching was done for the same conditions as used for air slots (1200 V, 12 mA, 1.6 sccm Cl_2 , 185 $^\circ\text{C}$).

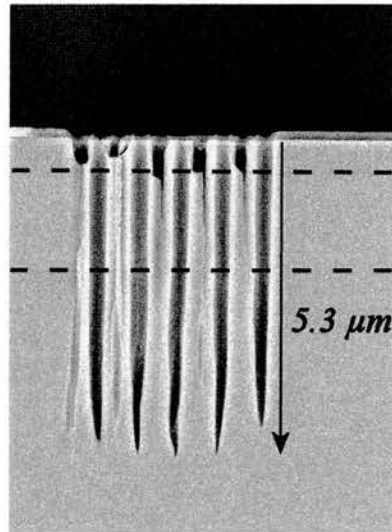


Fig. 17. SEM image of deep PhCs etched in InGaAsP/InP material. The hole diameter is 270 nm. Losses of 1.8-3.5 dB/mm were measured for this sample. The dashed lines have been added to highlight the position of the waveguiding layer (1.6 μm thick).

Propagation losses as small as 1.8-3.5 dB/mm were measured (Chapter 4) for the planar PhC waveguides in InP-based material etched under these conditions. These PhCs were etched to the depth of 5.3 μm (Fig. 17). To date, these are the best-reported results for etching the InP-based PhCs [14].

There is also a technical advantage of using high voltage-current ratio regime. Decreasing the beam current from 30 mA to about 10 mA significantly increases the life of the neutralizer inside the CAIBE machine.

3.3.6 Comparison of achieved etch depths

Table 1 presents a comparison between the etched profiles of 2-D PhCs in InP-based material achieved in our work and the best results available in the literature at that time (the year 2003).

Table 1. A comparison between the etched profiles¹

References	Etching method	Etch depth, μm	Hole diameter, nm	Effective etching depth, μm	Aspect-ratio
Ref. 14, KTH (2003)	CAIBE	~ 3	300	~ 2	10:1
Ref. 3, Alcatel (2002)	ICP	~ 3	240	2.8	13:3
Ref. 15, Wuerzburg (2002)	ECR~RIE	~ 4	240	~ 2.5	16:1
Our work (2003)	CAIBE	~ 5	250	3.5	21:1

NB. It has been observed that in general the narrower the hole the more difficult it is to etch (see above – the “RIE Lag” effect).

As one can see from the table, the results achieved in our work were some of the best etching results at that time, giving an aspect ratio of 21:1. Despite such promising etching results, there are still some problems left. For example, tapering of etched bottoms is still an issue, although it was possible to minimise the influence of such shape on propagating light by etching deeper [16]. A trivial explanation for tapered bottoms is as follows: for narrow and deep slots/holes it becomes more difficult to vaporise all InCl_x by-products which redeposit back on the bottom forming tapered bottoms of the etched features. There are possibly several ways for solving this

¹ Please note that the comparison of the etched profiles is rather relative here, and refers to the absolute etch depths achieved, neglecting material composition/layout etc

problem- going to higher temperatures ($> 250\text{ }^{\circ}\text{C}$) and/or lower etch pressures ($< 0.7 \cdot 10^{-4}\text{ mBar}$).

Another problem of etching high aspect-ratio features in InP heterostructures is “wobbling”. Although, it was possible to partly overcome this problem by going to higher beam voltages and, thus, gaining stronger beam directionality and reducing wobbling, some weak wobbling of etched features still remained. This “wobbling” mechanism has not been fully understood yet and requires additional research.

3.4 Summary

We have examined different regimes of CAIBE operation for the fabrication of semiconductor devices, such as Bragg gratings and 2-D PhCs.

Optimal etching conditions were found for chemically-physically balanced processes. Such conditions were investigated for GaAs- and InP- based materials for:

- a) waveguides;
- b) air/semiconductor Bragg gratings (1-D PhCs);
- c) 2-D PhCs.

We have also examined a new regime of CAIBE operation. We discussed the consequences of a “chemical-physical” unbalanced etching process and found that this balance is achieved for an approximately constant beam power, i.e., beam voltage-current product. The selectivity of the etch process increases with increasing beam voltage/current ratio, due to an increased mask resistance to high-energy ions. The high mask selectivity allows us to use a relatively thin silica mask (200-300 nm) that can be patterned with high resolution and good control over feature sizes. This regime can be used for both InP- and GaAs- based photonic crystal etching because no increase in sidewall roughness is observed, even at high-voltage etching conditions. Therefore, we were able to take advantage of the increased directionality of high beam voltage etching to produce high-quality InP-based photonic crystals with an etch depth of up to $5.3\text{ }\mu\text{m}$ [17].

We also believe that the limits of InP etching have not been reached yet and with further research better profiles may be possible¹.

¹ However, one has to bear in mind that there is a critical etch depth/shape for each wafer layout necessary for low loss photonic crystals and once this depth/shape is reached, further improvements in etch depth have less and less of an impact.

References

- [1] R. J. Shul and S. J. Pearton, *Handbook of Advanced Plasma Processing Techniques*, Chapter 11&12, Springer-Verlag, Berlin, Germany, 2000.
- [2] M. Mulot, S. Anand, M. Swillo, M. Qiu, B. Jaskorzynska, and A. Talneau, "Low-loss InP-based photonic-crystal waveguides etched with Ar/Cl₂ chemically assisted ion beam etching," *J. Vac. Scien. Technol. B*, vol. 21, pp. 900-903, Mar/Apr 2003.
- [3] R. Ferrini, B. Lombardet, B. Wild, R. Houdre, S. Olivier, H. Benisty, A. Djoudi, L. Legouezigou, S. Hubert, S. Sainson, J.-P. Chandouineau, S. Fabre, F. Pommereau, and G.-H. Duan, "Optical characterisation of 2D InP-based photonic crystals fabricated by inductively coupled plasma etching," *Electron. Lett.*, vol. 38, pp. 962-964, Aug 2002.
- [4] K. Avary, J. P. Reithmaier, F. Klopff, T. Happ, M. Kamp, and A. Forchel, "Deeply etched two-dimensional photonic crystals fabricated on GaAs/AlGaAs slab waveguides by using chemically assisted ion beam etching," *Microelectron. Engineer.*, vol. 61-62, pp. 875-880, 2002.
- [5] R. Ferrini, D. Leuenberger, M. Mulot, M. Qui, J. Moosburger, M. Kamp, A. Forchel, S. Anand, and R. Houdre, "Optical study of two dimensional InP-based photonic crystals by internal light source technique," *IEEE J. Quantum Electron.*, vol. 38, pp. 786-799, July 2002.
- [6] R. Ferrini, R. Houdre, H. Benisty, M. Qui, and J. Moosburger, "Radiation losses in planar photonic crystals: two-dimensional representation of hole depth and shape by an imaginary dielectric constant," *J. Opt. Soc. Am. B*, vol. 20, pp. 469-478, Mar 2003.
- [7] H. S. Fogler and N. M. Gurmen, *Elements of chemical reaction engineering*, Univ. of Michigan (<http://www.engin.umich.edu/~cre/>), Chapter 10.3, 2005.
- [8] K. Asakawa, T. Yoshikawa, S. Kohmoto, and Y. Nambu, "Chlorine-based dry etching of III/V compound semiconductors for optoelectronic applications," *Jpn. J. Appl. Phys.*, vol. 37, pp. 373-387, Feb 1998.
- [9] J. J. Cuomo, S. M. Rossnagel, and H. R. Kaufman, *Handbook of ion beam processing technology: principles, deposition, film modification and synthesis*, Noyes publications, Chapter 2, 1989.
- [10] L. O'Faolain, "Fabrication of microstructures for ultra-short pulse production in semiconductor lasers," *PhD thesis*, University of St Andrews, 2005.

- [11] M. Mulot, S. Anand, C. F. Carlstrom, M. Swillo, and A. Talneau, "Dry etching of photonic crystals in InP based materials," *Physica Scripta*, vol. 101, pp. 106-109, 2002.
- [12] M. V. Kotlyar, T. Karle, M. D. Settle, L. O'Faolain, and T. F. Krauss, "Low-loss photonic crystal defect waveguides in InP," *Appl. Phys. Lett.*, vol. 84, pp. 3588-3590, May 2004.
- [13] J. Daleiden, R. Keifer, S. Klusmann, M. Kunzer, C. Manz, M. Wailher, J. Braunstein, and G. Weimann, "Chemically-assisted ion-beam etching of (AlGa)As/GaAs: lattice damage and removal by in-situ Cl₂ treatment," *Microelect. Engineer.*, vol. 45, pp. 9-14, 1999.
- [14] M. Mulot, M. Qui, M. Swilo, B. Jaskorzynska, S. Anand, and A. Talneu, "In-plane resonant cavities with photonic crystal boundaries etched in InP-based heterostructure," *Appl. Phys. Lett.*, vol. 83, pp. 1095-1097, Aug 2003.
- [15] J. Moosburger, M. Kamp, A. Forchel, R. Ferrini, D. Leuenberger, R. Houdre, S. Anand, and J. Berggren, "Nanofabrication of high quality photonic crystals for integrated optics circuits," *Nanotechnology*, vol. 13, pp. 341-345, May 2002.
- [16] R. Ferrini, B. Lombardet, B. Wild, R. Houdre, and G.-H. Duan, "Hole depth- and shape-induced radiation losses in two-dimensional photonic crystals," *Appl. Phys. Lett.*, vol. 82, pp. 1009-1011, Feb 2003.
- [17] M. V. Kotlyar, L. O'Faolain, R. Wilson, and T. F. Krauss, "High-aspect-ratio chemically assisted ion-beam etching for photonic crystals using a high beam voltage-current ratio," *J. Vac. Scien. Technol. B*, vol. 22, pp. 1788-1791, July 2004.
- [18] S. A. Moore, L. O'Faolain, M. A. Cataluna, M. V. Kotlyar, and T. F. Krauss, "Reduced surface sidewall recombination and diffusion in quantum dot lasers," submitted to *Appl. Phys. Lett.*, 2005.

Chapter 4

Propagation Losses

The propagation losses of two-dimensional (2-D) planar photonic crystal (PhC) waveguides are the subject of this chapter. In order to extract PhC propagation losses a Fourier transform technique was used. This technique was studied using examples of numerically simulated Fabry-Perot fringes. Following this, the planar PhC waveguides in InP-based material, with three air rows removed, were characterised using the “end-fire” technique. Low-losses (1.8 dB/mm) were extracted for PhC waveguides with a period of 400 nm.

4.1 Origin of propagation losses in photonic crystal waveguides

The issue of the light line in the dispersion spectrum of a PhC (see Chapter 1) is very important when one considers propagation losses in 2-D PhC slab waveguides. When electromagnetic modes of PhC-based devices lie above the light line of the cladding they are affected by out-of-plane diffraction. This causes intrinsic radiation losses [1], i.e., they occur even for perfect crystals.

Two approaches have been suggested in order to keep out-of-plane scattering low: structures with very high and low index contrast in the slab waveguide. PhC slabs based on two these approaches are referred to as “membranes” (very high index contrast) and “substrate approach” (low index contrast).

A practical example of very high refractive index contrast structure is silicon on insulator (SOI). In these systems, some photonic modes may operate below the light line of the cladding. This means that no coupling to the radiation modes is allowed for these modes. However, structures fabricated in practice are not perfect (roughness, *etc*) and out-of-plane scattering may occur. Recently, SOI PhC waveguides have demonstrated very low loss [2].

As far as the “substrate approach” is concerned, it has been demonstrated that deeply etched PhCs in low-contrast waveguide structures are favourable for out-of-plane loss reduction [3, 4]. An example for such a structure is a conventional

heterostructure in III-V semiconductors (InP/InGaAsP or GaAs/AlGaAs). However, weaker guiding makes the etching process critical, as etch depth must be increased in order to minimize out-of-plane scattering losses. A scalar analytical perturbative approach [5] shows that losses scale as $(\Delta\epsilon)^2$, where $\Delta\epsilon$ is the dielectric constant step in the waveguide. The guided mode extends further into the cladding for decreasing $\Delta\epsilon$, approaching the behaviour of plane waves incident normally to arrays of infinitely deep holes. Thus, if the etch depth can be increased sufficiently, extension of the optical wave may remove out-of-plane loss altogether. The devices examined in this chapter are fabricated in low-contrast index InP/InGaAsP heterostructures with a relatively thick core of 1.6 μm .

Losses in PhC waveguides that are due to fabrication imperfections, such as roughness, can be regarded as extrinsic losses. Due to the strong interaction between the light and the PhC, the hole shape, depth and hole smoothness strongly affect the light propagation [6, 7]. Finite hole depth affects the light propagating through PhC by coupling it to substrate modes— as does an imperfect hole shape. Although an “infinite” hole depth is desirable for loss reduction, it has been shown by Ferrini *et al.* that there is a depth limit for a given waveguide beyond which further increases in depth cause only negligible improvement [6].

A particular problem in InP etching is that the etched holes often show a taper towards the bottom (a conical shape), which compromises performance and creates a further source of out-of-plane losses. A lot of modelling has been carried out examining this effect [6, 8]. It has been shown that depending on the shape of the hole (strong or weak tapering) there are two regimes where losses are influenced either by the hole depth (weak tapering) or by its shape (strong tapering- tapering starts early and tapers down very fast). These results demonstrate that both depth and shape of the hole has to be improved to get low-loss propagation.

In Chapter 3, we have shown how the overall quality of the etched holes may be improved. This regime allows etching of very deep, smooth holes. Thus, tapering occurs far away from the waveguide core, minimising its effect (and thus loss). Also, deeply etched holes extending the optical wave partly reduce out-of-plane loss. All devices analyzed in this chapter were etched using this favourable regime of CAIBE.

4.2 Propagation losses analysis (theory)

The extraction of the total internal loss in Fabry-Perot (F-P) resonators through The Fourier analysis of the Fabry-Perot fringes obtained in transmission was proposed by D. Hofstetter and R. I. Thornton in 1997 [9]. This generalised method was used to extract total losses/gain of low- and high-finesse resonators. It also works for active as well as passive resonators. In [9] the expression for Fourier transform (FT) of a F-P spectrum was analytically derived.

We now apply this method to analyzing propagation losses of 2-D PhCs in InP-based material. Instead of using an analytical formula like Hofstetter *et al.*, we use a numerical fast Fourier transform function (MATLAB) and apply it to both the experimentally obtained PhC transmission spectra and numerically simulated transmission spectra¹.

4.2.1 Theoretically simulated Fabry-Perot fringes

In order to understand this technique in detail, we will apply it to a theoretically simulated fringe spectrum.

Let us consider a F-P resonator of length L and consisting of a piece of material with refractive and absorption indexes n and k , respectively, with two parallel facets of reflectivity, R . The transmitted intensity of the electrical field experiencing multiple reflections between the facets is given by [9]:

$$I(\beta) = \frac{(1 - R)^2 \exp(-2kL\beta) + 4 \sin^2(\psi)}{[1 - R * \exp(-2kL\beta)]^2 + 4R * \exp(-2kL\beta) \sin^2(\psi + nL\beta)} . \quad (1)$$

In equation (1), $\beta = \frac{2\pi}{\lambda}$ is the wave number and $\psi = \arctan(-2k/(n^2 + k^2 - 1))$

is the phase change of the light that is due to the facet reflection.

Fig. 1 shows the transmitted intensity according to Eq. (1) for $R=0.3$, $n=3.388$, $\alpha=10 \text{ cm}^{-1}$. The absorption coefficient α is connected with the absorption index k by

the expression $\alpha = \frac{4\pi k}{\lambda}$. The cavity length is $500 \text{ }\mu\text{m}$.

¹ We use a numeric rather than analytic formula, as this mimics the discrete points given by a spectrometer.

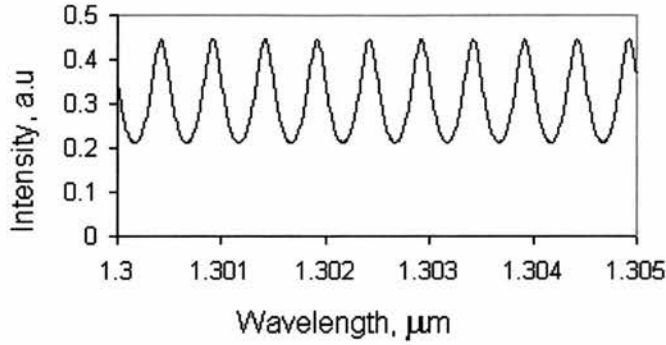


Fig.1. Theoretically simulated FP spectrum for a cavity of 500 μm long ($R=0.3$, $n=3.388$, $\alpha=10 \text{ cm}^{-1}$)

4.2.2 Fourier transform of Fabry-Perot fringes

The Fabry-Perot fringe spectrum contains information on light making multiple roundtrips of the cavity. Taking a Fourier transform of this gives a series of harmonics/peaks, where each harmonic corresponds to a roundtrip of light inside the cavity. Figure 2 represents, *on a logarithmic scale*, the FT of theoretically simulated F-P fringes from Fig. 1. The two axes y and x represent the amplitude of harmonics and the number of points used to calculate the FT numerically (we present only half of the points of the FT spectrum, as it is symmetric around the origin), respectively.

The finesse of the resonator, defined by $F = \frac{\pi\sqrt{R}}{1-R}$, is relatively low ($F = 2.46$) but the

F-P fringe shape (Fig.1) already deviates from sinusoidal shape. Therefore, there are higher-order harmonics (see Fig. 2) in the FT.

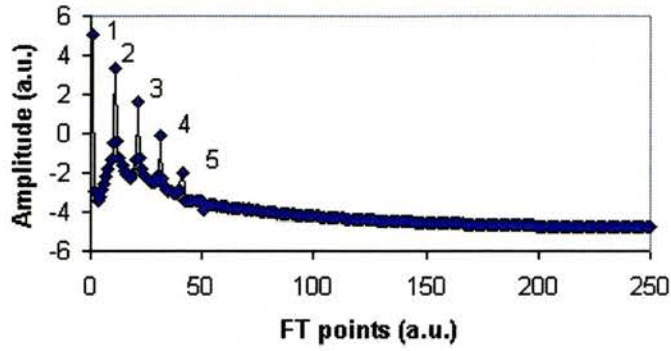


Fig. 2. The numerical FT (on a logarithmic scale) of the transmission spectrum given in Fig. 1. Only the first 4 peaks are sufficiently clear for use in the calculation, the 5th peak is not fully resolved. Each peak corresponds to the intensity of light for a round-trip and the distance between peaks is proportional to the optical path length ($2Ln$).

The propagation loss of the cavity is related to the ratio between the amplitudes of adjacent harmonics. The FWHM of a single peak is inversely proportional to the width of the wavelength range of the transmission spectrum analyzed (5 nm in our case).

The advantage of this method is that the Fourier transform contains information on the overall shape of the Fabry-Perot fringes and determines not only their visibility [10] but also their finesse to a high degree of accuracy. Furthermore, the method is independent of insertion loss, thereby removing a major source of uncertainty encountered with other methods.

The Fourier transform of the FP spectrum basically describes a function with peaks that are arranged symmetrically to the origin (there is only one half of the peaks in Fig. 2). The values on the x-axes can also be expressed in the units of inverse length using the following formula: $\Delta\nu * \Delta L = M^{-1}$, where ΔL is the resolution (0.01nm) of the Fabry-Perot spectrum in microns, $\Delta\nu$ is the space frequency in inverse microns (which means the number of periods per micron), and M is the number of the points (500 in our case). Knowing this formula, the numbers on the x-axis (1, 2, 3... 500) can be replaced by the space frequency values ($\Delta\nu, 2\Delta\nu, 3\Delta\nu...500\Delta\nu$).

The distance between two adjacent harmonics peaks in μm^{-1} (x-axis) is proportional to the resonator length ($2Ln/\lambda^2$), where “n” is the refractive index of the

medium and λ is the wavelength. The height of the peaks decreases exponentially with increasing order. The total cavity loss is related to the harmonic amplitude ratio (*HAR*). It includes both the cavity propagation loss and the mirror loss:

$$HAR = R * \exp\left(-\frac{\alpha}{2} * 2L\right), \quad (2)$$

where $R = \sqrt{r_1 * r_2}$ and $r_{1,2}$ are the reflectivity at each facet.

The facet reflectivity is usually known (or can be easily calculated), so the resonator loss can be extracted from formula (2). For all described examples the reflectivity at each facet is assumed to be equal.

In order to find propagation loss via formula (2) the following fitting formula was introduced:

$$y = P_0 + (\ln(R) - (\alpha * L)) * x, \quad (3)$$

where P_0 is an amplitude of the first harmonic and x is the peak number. Fitting this formula to the harmonic amplitudes of the FT on a logarithmic scale versus peak number, a propagation loss of 10.06 cm^{-1} may be extracted. The fitting error of the answer is about $\pm 0.078 \text{ cm}^{-1}$ (less than 1 %). Thus, the discrepancy of 0.061 between found value (10.061 cm^{-1}) and initial value (10 cm^{-1}) lies within the error. This error is the result of a loss of information due to the finite resolution. The resolution of the FP fringes was 0.01 nm (comparable with the practically achievable values) and the length of the examined spectrum was 5 nm. The influence of these two parameters on the accuracy of the results will be discussed below in this section.

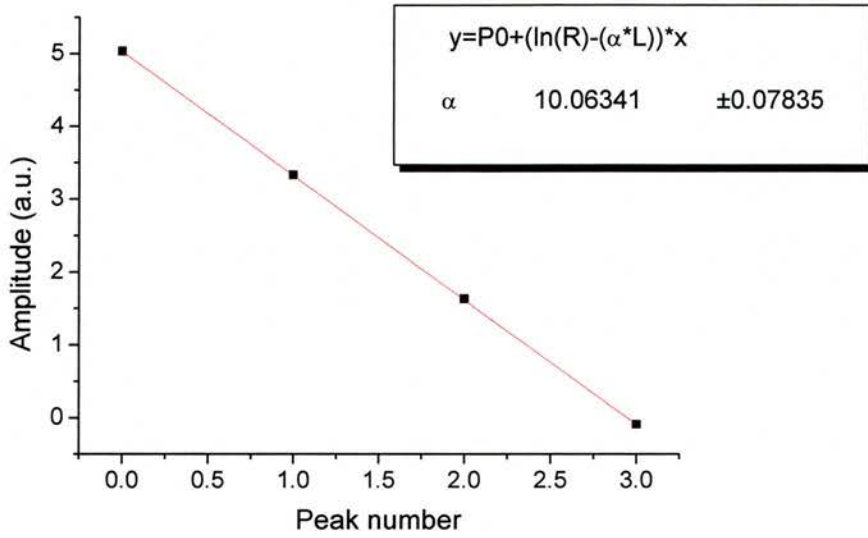


Fig. 3. Amplitude of the FT harmonics via their number. The line is fitted via formula (3).

4.2.3 Limitations and errors of the method

There are several important parameters that should be taken into account obtaining losses via the Fourier transform of the F-P spectrum. These parameters are as follows:

- 1) Length of the spectrum taken.

The required spectrum should be between 3 and 7 nm of wavelength range. There are two reasons for it- the fringe separation naturally increases with increasing wavelength and the fringe separation is affected by dispersion. The first effect is taken into account in the theoretical formula (1). Both effects are present the experimental data, and distort the FT spectrum. They appear as an increased loss, though it is information not light that is lost, as through dispersion and stretching the FT fails to pick out points which it should. Thus, for high accuracy, the fringe separation should be kept as constant as possible, i.e. a narrow wavelength window should be used. Taking the frequency spectrum (instead of wavelength) will avoid some of this smearing, however, material dispersion-induced smear will still remain.

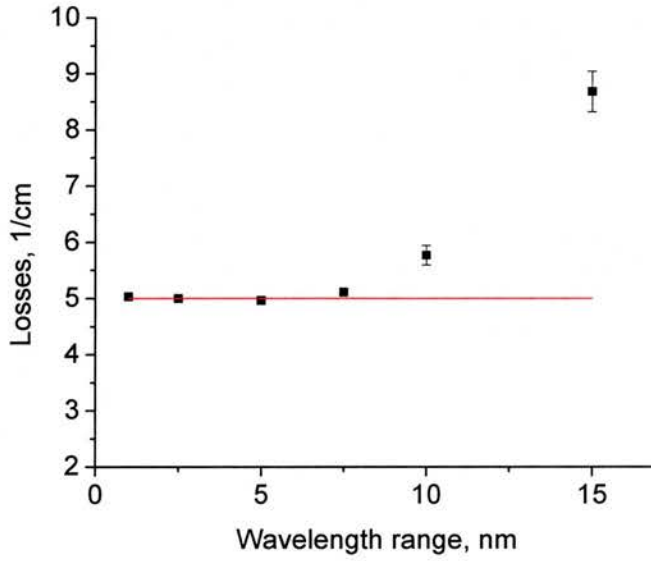


Fig.4. Losses extracted from the FT for theoretically simulated fringes.

Fig.4 represents the dependence of obtained losses on the length of transmission spectrum. The initial loss used in formula (1) was 5 cm^{-1} for this case.

The losses for each wavelength range were found fitting the function described in formula (3). As one can see, the derived values lie close to the theoretical value inside a wavelength range less than 8 nm. The error increases rapidly for a wavelength range more than 10 nm.

Thus, all theoretical (previous) and experimental (in the next sections) FP fringes are taken over a 5 nm wavelength range.

2) Resolution.

As large wavelength scans cannot be used (see above), the accuracy of the result becomes dependent on the resolution (it is proportional to the amount of information that is Fourier transformed). For a given wavelength and refractive index, the relationship between the cavity length and the fringe separation (Δl) is as follows:

$$\Delta l = \frac{\lambda^2}{2 * L * n}. \quad (4)$$

(Note the dependence of fringe width on wavelength).

Thus, at 1300 nm the fringe separation is 0.5 nm, for the L and n used previously, equation (1).

Table 1 presents comparative data for extracted loss via the FT of transmission spectrum for different scan resolutions. The theoretical value was 10 cm^{-1} .

We see that with 50 points per fringe and above an accuracy of better than 1% may be achieved. This is of practical use.

Table 1. The relationship between loss, accuracy and resolution

Resolution, nm	Loss, 1/cm	Fitting error, 1/cm	Discrepancy from the theoretical value error, %
0.001	10.01134	+/- 0.054	0.1
0.01	10.06341	+/- 0.07835	0.6
0.02	10.12259	+/- 0.10618	1.2
0.05	10.31326	+/- 0.19378	3.1
0.1	9.27371	+/- 0.377	7.3

The errors for resolutions of 0.001 nm and 0.01 nm lie within the fitting error values and are less than 1 % of the initial value. The errors for 0.02 nm and 0.05 nm exceed 4 % of the theoretical value and lies outside the fitting error region. The error reaches 7 % for the scan step of 0.1 nm. The error values achieved here represent the errors imposed by different parameters applied to the method. Real experimental data would have larger errors due to noise, etc.

- 3) Facet reflectivity. The method relies on the facet reflectivity being constant. In experimental data, this may not be the case, e.g. due to imperfect cleaving.

4.3 Photonic crystal propagation losses measurements

We now apply this FT technique to experimentally obtained transmission spectra of the PhC waveguide. These waveguides are formed by removing three rows of holes (W3). Losses of between 1.8-3.5 dB/mm for W3 waveguides were measured. The previous best was a result from Mulot *et al.* [11], which reports 5 dB/mm propagation loss in a W3 waveguide.

In the fabrication of these crystals, we made use of the highly effective regime of CAIBE discussed in Chapter 3.

4.3.1 Description of photonic crystals used in this work

In contrast to W1 waveguides, where one row of holes is removed, W3 waveguides can support the fundamental mode as well as higher-order modes. The existence of mini-stop bands [12] between these higher-order modes, offers interesting opportunities for spectral and dispersive functionalities, thus making the W3 waveguides advantageous for practical applications. Due to their larger width, the propagation loss is also much lower than of the W1 waveguides.

The InGaAsP heterostructure used in the experiments consisted of a 0.6- μm -thick InP top cladding layer and a 1.6 μm InGaAsP core layer, followed by 1.5- μm -thick lower cladding of InP (the details are given in Chapter 5). Such a thick core was chosen to yield a greater overlap with a single-mode fibre core, thus increasing the input coupling, and we believe it may also reduce diffraction losses due to a flatter mode profile in the vertical direction [4, 1]. Fig 6 shows a top view of PhCs of 320 nm period. Adiabatically tapered ridge waveguides were used to access these guides. The patterns were e-beam written at the University of Glasgow.

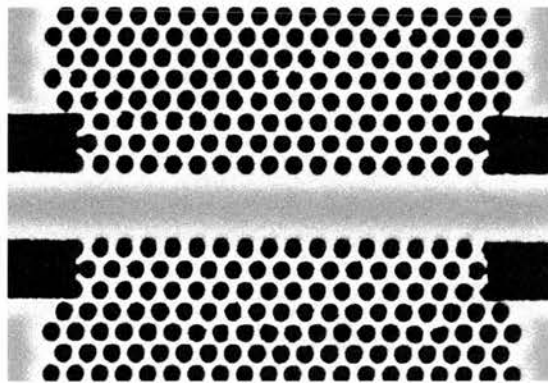


Fig.6. A SEM image of the PhC (top view). It is a triangular lattice with a period of 320 nm. The pattern was e-beam written at the University of Glasgow.

A high voltage-current ratio was used for etching PhCs in CAIBE, using Cl_2 as the reactive gas. The conditions were the following: beam voltage- 1200 V, beam current- 12 mA, chlorine flow- 1.6 sccm, substrate temperature- 185 $^\circ\text{C}$ [13]. The resulting PhC holes have vertical walls and a relatively large depth (4.4-5.4 μm) [Fig.

7]. This ensures almost complete overlap of the propagating mode with the etched holes. As Fig. 7 shows, the effective etch depth (without bending or tapering of the holes) is as large as $3.5\ \mu\text{m}$ or above.

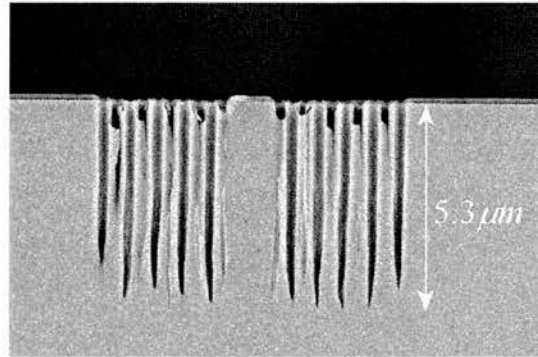


Fig.7. A SEM image of an actual device examined in this chapter. The etch depth is more than $5\ \mu\text{m}$ for a hole diameter of $250\ \text{nm}$. The apparent surface damage resulted from the cleaving process.

4.3.2 Fourier transform of photonic crystal transmission spectrum

Following fabrication, the waveguides were characterised optically using the Fourier transform technique. In this case, the Fabry-Perot fringes originate from the cavity defined by the cleaved facets at each end of the device. This cavity length (i.e., the sample length of $750\ \mu\text{m}$) was constant while the length of PhCs was varied from 20 to $110\ \mu\text{m}$. As discussed below, we can ignore the cavity formed by the PhC waveguide due to the small reflection at the PhC-ridge waveguide interface. PhC waveguides of $340\ \text{nm}$ period with three different lengths ($6.215\ \mu\text{m}$, $12.43\ \mu\text{m}$ and $26.555\ \mu\text{m}$) are presented in Fig. 8.

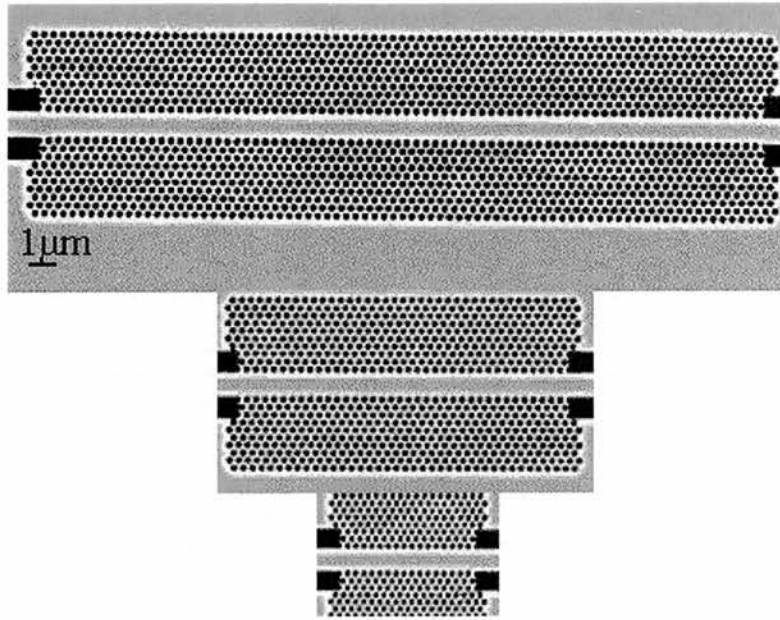


Fig.8. A SEM image of three different lengths PhC waveguides of 340 nm period.

Two broadband light-emitting diode (LED) sources were used to characterize the samples. The first was centred at 1330 nm and the second at 1410 nm with a full width at half maximum of ~ 100 nm and ~ 50 nm, respectively, allowing us to compare the PhC structures with different lattice constants at the same normalized frequency. The measurement set-up is presented in Fig. 9. A lensed-fibre was used to access the sample. The output signal was collected via the lens (with 40 times magnification) and sent to the input of the optical spectrum analyzer (OSA). A polarizer was used to select TE-polarization. A flipper mirror was used to check the mode profile via an infrared viewer. A small aperture before OSA helped to cut-off noise (substrate and air modes).

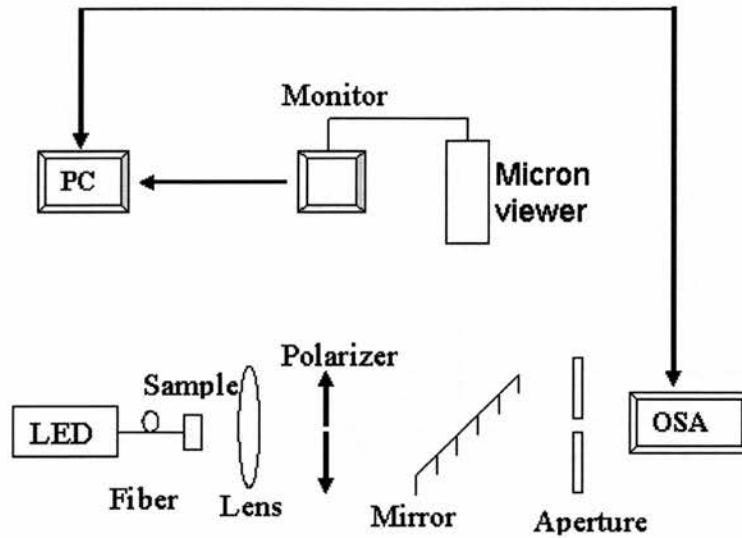


Fig.9. The transmission measurement set-up.

The transmission spectrum was taken each time over a wavelength range of 5 nm around the peak emission wavelength of the LEDs. The scan step size was 0.01 nm to ensure fully resolved fringes for the FT analysis. The transmission spectrum for a 340 nm period PhC of length 26.55 μm (see Fig. 8 above) is shown in Fig. 10.

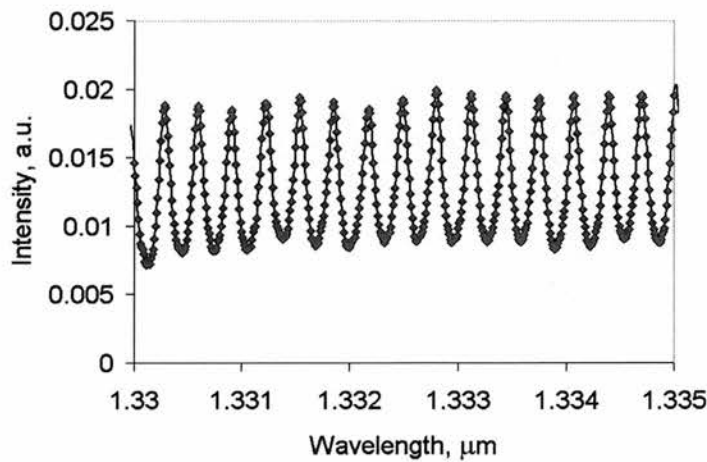


Fig.10. Experimental FP spectrum over 5 nm for a PhC waveguide of 340 nm period and 26.55 μm length.

The Fourier transform of this transmission spectrum is presented in Fig.11. The FT for a longer PhC of the same period is represented by the line lying below and shows a higher total loss as expected. As one can see there are only 3 peaks fully

resolved for a 112 μm long PhC as compared to the 4 resolved peaks of the 26 μm long PhC. This is connected to the higher loss of the longer PhC waveguide. Thus by taking the transmission spectrum of PhCs of different lengths but with the same period, one can extract propagation losses of PhC itself.

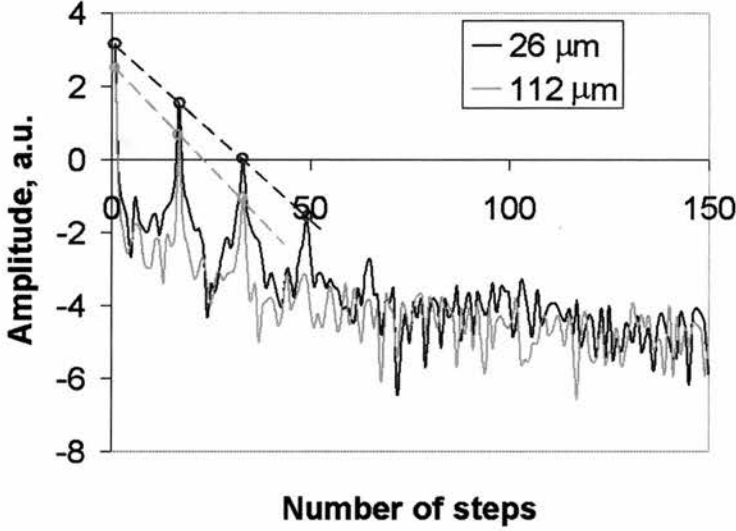


Fig.11. The numerical Fourier transform (FT) of the PhC transmission spectrum (340-nm period) for two different lengths of 112 and 26.55 μm .

In order to extract losses from the FT graph, the above-mentioned formula (3) is used. But now instead of a simple “ αL ” term, a new parameter P is introduced due to the complexity of our experimental structure which includes conventional and PhC waveguides simultaneously. The parameter P is connected with the photonic crystal and access waveguides losses via the following expression:

$$P = \alpha_{WG} * [L_{total} - L_{PhC}] + \alpha_{PhC} * L_{PhC}, \quad (5)$$

where $\alpha_{WG,PhC}$ are losses of the access waveguides or PhC, respectively, and the physical meaning of this parameter is simply the propagation loss per device.

Thus, by varying L_{PhC} , the propagation losses of the PhC waveguides can be derived from the slope of the $P-L_{PhC}$ curve. Fig. 12 presents the dependence of parameter P on the length of the embedded PhC waveguides. The overall length of the structure (ridge waveguides, tapers and the PhC waveguide) was 0.75 mm. The period of the PhC, in this case, was 340 nm. Losses in the access waveguides were calculated from the intercept ($L_{PhC} = 0$) of the graph. Thus, we have:

$$\alpha_{PhC} = \alpha_{WG} + \frac{P_2 - P_1}{L_2 - L_1} . \quad (6)$$

A propagation loss of 0.52 mm^{-1} was extracted from the slope of this graph, assuming that mirror losses along the sample stay constant.

The mirror losses were calculated to be $\sim 30 \%$ (this is a usual value for the air/semiconductor III-V interface).

In the literature, two measures of propagation loss are typically used, namely, [dB/length] and [1/length]. They are connected by the following relationship:

$$\alpha[\text{dB/length}] = 4.31 * \alpha[1/\text{length}] \quad (7)$$

Therefore, the loss of 0.52 mm^{-1} obtained via formula (6) corresponds to 2.2 dB/mm using formula (7).

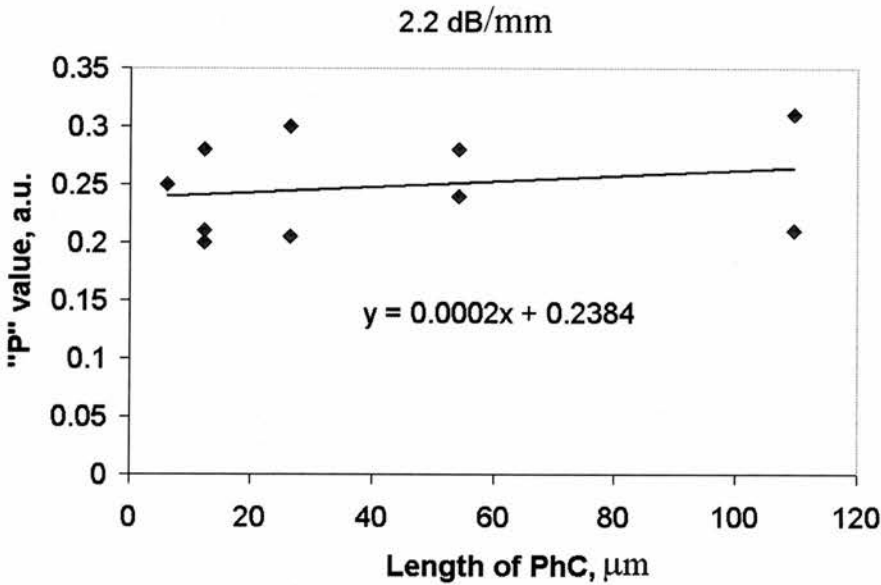


Fig.12. Losses per device extracted from the Fourier transforms for the 340-nm period PhC. The transmission spectra were measured over the wavelength range of 1330-1335 nm.

Multiple data points for each PhC length present the data from the different sets of the nominally identical PhC waveguides, which gives an indication of the measurement error. The main factor causing the data scatter is a small variation in the facet quality along the sample, which changes the reflection coefficient for the calculation. Fabrication imperfections also contribute to the error by slightly varying waveguide loss for different devices.

The propagation losses derived from this graph agree well with the losses derived from a similar graph for a wavelength range of 1410- 1430 nm. The loss in this case is 2.6 dB/mm. Although for a longer wavelength slightly higher loss was extracted, we cannot make any further conclusions due to the experimental error, apart from the consistency of the losses obtained.

The PhCs of different periods were also measured. A larger PhC period results in a smaller propagation loss. A loss of 1.8 dB/mm was extracted for a period of 400 nm, whereas losses of 3.5 dB/mm were derived for a period of 320 nm.

One of the reasons for the increased loss with decreasing PhC period is that smaller holes have a smaller etch depth (Fig. 13) due to the well-known phenomenon of RIE lag (see Chapter 3), so tapering and bending effects occur closer to the waveguide, resulting in higher losses [8].

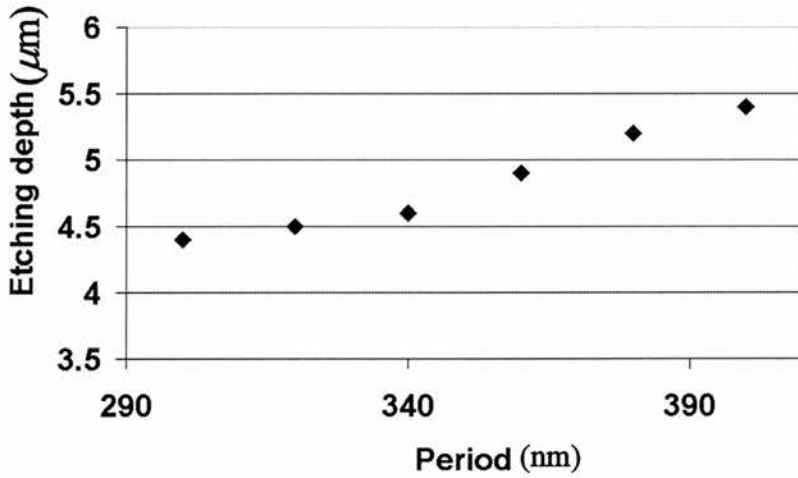


Fig.13. Etch depth dependence on the period a , with hole radius r kept constant at $r = a/3$. Measurements were taken from the same sample that was analysed in this work.

The same dependence of the loss on the width of the spectrum as previously described (Fig. 4) was observed in practice. This dependence is depicted in Fig. 14. As one can see, the loss stays constant for a wavelength window of 5-10 nm and increases rapidly with increasing the width of this window. This graph was plotted for a straight waveguide 750 μm long and 1.2 μm wide. For the windows between 4 and 10 nm, an average loss value is around 2.2 cm^{-1} (0.95 dB/mm).

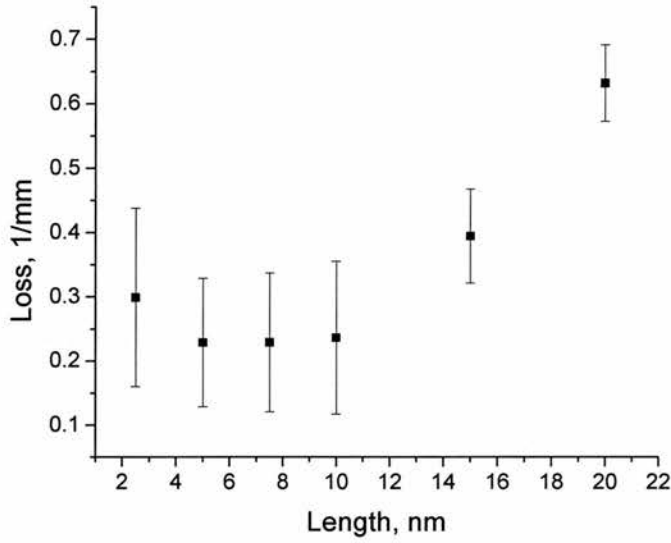


Fig.14. The dependence of the calculated loss of experimental propagation data on the width of the examined spectrum.

4.3.3. Finding losses via interference technique

As an alternative, we compared the losses measured by the FT with those obtained via the interference-technique [14]. This is a well-documented technique widely used in optics to measure precisely the reflection and transmission coefficients of mirrors. This technique is based on F-P fringe contrast measurements and often used to measure propagation losses in PhC waveguides [10, 15]. The visibility of the F-P fringes is defined by the following formula:

$$V = \frac{I_{\max} - I_{\min}}{I_{\max} + I_{\min}} \quad (8)$$

where $I_{\max, \min}$ are the maximum and minimum, respectively, total intensities of the F-P resonator. The visibility relates to the propagation loss according to:

$$V = R^2 \exp(-\alpha * L) \quad (9)$$

Thus, plotting the visibility on the logarithmic scale for PhC waveguides of different lengths, the propagation loss can be extracted from the slope of the curve. Fig. 15 illustrates the visibility of the fringes extracted for a PhC of 340 nm period.

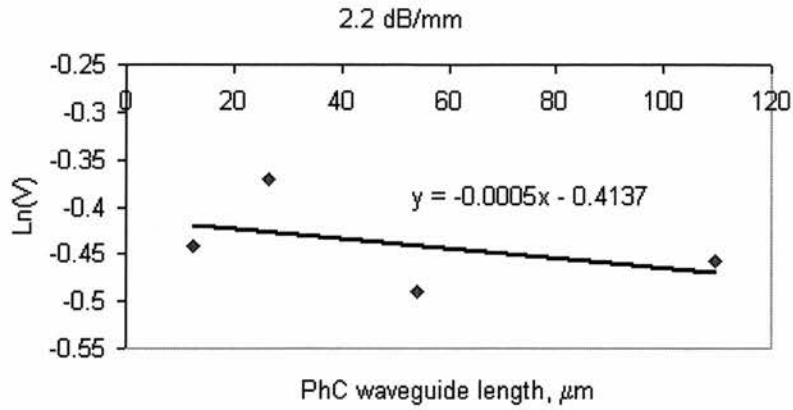


Fig.15. The visibility of the FP fringes vs. length of the PhC waveguide of 340 nm period. The transmission spectrum was taken in the range of 1330-1335 nm.

The measurements are carried out for the transmission spectrum taken over 5 nm wavelength range (as for the above-described FT technique). As one can see, similar losses of 2.2 dB/mm are derived using this method. This is consistent with the losses obtained via the FT. The FT technique is more reliable as it contains information on peak shape as well as peak's visibility.

4.4 Summary

To summarize this chapter's results, we have discussed in detail the Fourier transform technique applied to the Fabry-Perot cavity transmission spectrum. The errors and limitations of the method were discussed. Propagation losses were determined by applying this Fourier transform technique to experimental PhC data. Data for losses in the PhCs of different length and different periods were taken and analyzed. Losses as small as 1.8 dB/mm were measured for a period of 400 nm. This was the smallest loss, to the best of our knowledge, for the planar PhC waveguides in III-V semiconductor-based materials reported to date.

We believe that the improvement in transmission is due to higher-quality PhC holes etched using high beam voltage-current ratio CAIBE. The ability to achieve large etch depths allows the use of a relatively thick waveguide, which reduces diffraction losses in the air sections. We believe these to be the main causes of the improvement relative to the previous work [11], allowing us to almost reach the intrinsic loss limit [16] of 1.8 dB/mm for PhCs of 400 nm period. At the same time,

further improvement in the etching technique and better waveguide design promises to lead to smaller losses (~ 2 dB/mm) for PhCs with smaller periods (300 nm). For example, it has been recently demonstrated that the out-of-plane losses can be minimized by optimizing the planar waveguide for a given etching process and/or for a given hole shape [16], allowing one to reach the intrinsic loss limit.

References

- [1] L. C. Andreani and M. Ajo, "Intrinsic diffraction losses in photonic crystal waveguides with line defects", *Appl. Phys. Lett.*, vol. 82, pp. 2011-2013, Mar 2003.
- [2] E. Kuramochi, A. Shinya, M. Notomi, T. Tsuchizawa, T. Watanabe, H. Fukuda, and K. Yamada, "Low propagation loss Si-based photonic crystal slab waveguides," *Proc. International Workshop on Photonic Electromagnetic Structures (PECS)*, Kyoto, Japan, 2004.
- [3] H. Benisty, C. Weisbuch, D. Labilloy, M. Rattier, C.J.M. Smith, T.F. Krauss, R.M. De la Rue, R. Houdre, U. Oesterle, C. Jouanin, and D. Cassagne, "Optical and confinement properties of two-dimensional photonic crystals," *J. Lightwave Technol.*, vol. 17, pp. 2063-2077, Nov 1999.
- [4] W. Bogaerts, P. Bienstman, D. Taillaert, R. Baets, and D. De Zutter, "Out-of-plane scattering in photonic crystal slabs", *IEEE Photon. Technol. Lett.*, vol. 13, pp. 565-567, Jun 2001.
- [5] H. Benisty, D. Labilloy, C. Weisbuch, C. J. M. Smith, T. F. Krauss, D. Cassagne. A. Beraud, and C. Jouanin, "Radiation losses of waveguide-based two-dimensional photonic crystals: positive role of the substrate," *Appl. Phys. Lett.*, vol. 76, pp. 532-534, Jan 2000.
- [6] R. Ferrini, B. Lombardet, B. Wild, R. Houdre, and G.-H. Duan, "Hole depth- and shape-induced radiation losses in two-dimensional photonic crystals," *Appl. Phys. Lett.*, vol. 82, pp. 1009-1011, Feb 2003.
- [7] M. Palamaru and P. Lalanne, "Photonic crystal waveguides: out-of-plane losses and adiabatic modal conversion," *Appl. Phys. Lett.*, vol. 78, pp. 1466-1468, Mar 2001.
- [8] R. Ferrini, R. Houdre, H. Benisty, M. Qui, and J. Moosburger, "Radiation losses in planar photonic crystals: two-dimensional representation of hole depth and shape by an imaginary dielectric constant," *J. Opt. Soc. Am. B*, vol. 20, pp. 469-478, Mar 2003.

- [9] D. Hofstetter and R. Thornton, "Theory of loss measurements of Fabry-Perot resonators by Fourier analysis of the transmission spectra," *Opt. Lett.*, vol. 22, pp. 1831-1833, Dec 1997.
- [10] E. Schwoob, H. Benisty, S. Olivier, C. Weisbuch, C. Smith, T. Krauss, R. Houdré, and U. Oesterle, "Two-mode fringes in planar photonic crystal waveguides with constrictions: a probe that is sensitive to propagation losses," *J. Opt. Soc. Am. B*, vol. 19, pp. 2403-2412, Oct 2002.
- [11] M. Mulot, M. Qui, M. Swillo, B. Jaskorynska, S. Anand, and A. Talneau, "In-plane resonant cavities with photonic crystal boundaries etched in InP-based heterostructure," *Appl. Phys. Lett.*, vol. 83, pp. 1095-1097, Aug 2003.
- [12] C. J. M. Smith, R. M. De La Rue, T. F. Krauss, H. Benisty, S. Olivier, M. Rattier, C. Weisbuch, R. Houdré, and U. Oesterle, "Low-loss channel waveguides with two-dimensional photonic crystal boundaries," *Appl. Phys. Lett.*, vol. 77, pp. 2813-2815, Oct 2000.
- [13] M. V. Kotlyar, L. O'Faolain, R. Wilson, and T. F. Krauss, "High-aspect-ratio chemically assisted ion-beam etching for photonic crystals using a high beam voltage-current ratio," *J. Vac. Scien. Technol. B*, vol. 22, pp. 1788-1791, Jul 2004.
- [14] I. P. Kaminow and L. W. Stulz, "Loss in cleaved Ti-diffused LiNbO₃ waveguides," *Appl. Phys. Lett.*, vol. 33, pp. 62-64, Jul 1978.
- [15] A. Talneau, L. Le Gouezigou and N. Bouadma, "Quantitative measurement of low propagation losses at 1.55 μm on planar photonic crystal waveguides," *Opt. Lett.*, vol. 26, pp. 1259-1261, Aug 2001.
- [16] R. Ferrini, A. Berrier, L. A. Dunbar, R. Houdré, M. Mulot, S. Anand, S. de Rossi and A. Talneau, "Minimization of out-of-plane losses in planar photonic crystals by optimizing the vertical waveguide," *Appl. Phys. Lett.*, vol. 85, pp. 3998-3400, Nov 2004.

Chapter 5

Tunable filters in one-dimensional photonic crystals in InP heterostructure

This chapter is dedicated to the realisation of tunable devices. A Fabry-Perot cavity with one-dimensional photonic crystal mirrors is used. Filters with full width at half maximum of less than 2 nm are realised. The quantum confined Stark effect and free carrier-injection were both implemented as means of realising tunability. Two wafers with 10 and 5 InGaAsP/InGaAsP multiple quantum wells were designed. The wafers were grown at the University of Sheffield. Fabricated active devices have shown a tuning range of about ± 2 nm.

5.1 Introduction

Compact tunable devices are essential components for microphotonic circuits. III-V semiconductors are attractive in terms of device miniaturization due to their high refractive indexes (above 3). InP-based materials make it possible to work around 1.3 and 1.55 μm , which are the favourable wavelengths of fibre optics.

The use of microcavities such as micro-rings [1], micro-discs [2] and Fabry-Perot (F-P) type resonators [3] allows for the confinement of the optical mode to very small regions. Thus, microcavity-based devices typically consume only small levels of external power to produce the desired tunability and can be potentially very fast due to small parasitic capacitances. A further advantage of microcavities is that their transmission at the resonance wavelength becomes very sensitive to small refractive index changes, so cavities with high Q-factor are preferable, especially for applications in switching. The most common ways of realizing tunability in photonics are the quantum confined Stark effect (QCSE), carrier-injection, thermal tuning and the Kerr-effect. Of these, QCSE and carrier injection are the most promising in the microphotonics context; ultrafast tuning via the Kerr effect provides too small a refractive index change and requires much higher

optical intensities [4], whereas thermal tuning [5] is typically too slow (ms – regime) and generates excessive heat loads for densely integrated circuits. The present chapter therefore focuses on QCSE and carrier injection.

These effects cannot be considered in isolation, however; thermal effects are especially relevant for carrier-injection devices, because the carrier-related heating leads to a thermo-optic refractive index shift that is of the opposite sign to the electro-optic shift [3]. Electro-optic and thermal effects may, therefore, counteract one another, which is highly undesirable. Thermal conductivity is thus another reason for choosing a III-V substrate (as opposed to SiO₂ or air cladding as in silicon on insulator (SOI) and membrane-type devices, respectively, both of which lead to much higher thermal resistances).

Fabry-Perot type resonators are frequently used as filters in such systems. For example, a tunable F-P resonator was recently realized in silicon on insulator and experimentally tuned by carrier-injection [3]. Tuning of 0.8 nm was achieved for 20 mW of consumed power. The tuning mechanism, however, was thermo-optical rather than electronic, due to the relatively high thermal resistance of the examined device of around 1 K/mW.

The etching of high-aspect-ratio features in InP has traditionally been very difficult, preventing the realisation of InP one- and two-dimensional (1-, 2-D) photonic crystals (PhCs). However, the new etching regime introduced in Chapter 3 allows the successful etching of InP material. In Chapter 4, we have described the fabrication and characterisation of low-loss InP photonic crystal waveguides using this technique.

In this chapter, we fabricate deeply etched tunable InP-based filters of the F-P resonator type. Deeply etched narrow air-slots were used in order to reach high reflectivity using only few pairs of Bragg mirrors, while keeping diffraction losses at minimum. Red and blue-shifts of resonance transmission peaks were observed for QCSE- and carrier-injection tuned devices, respectively. The tuning results are analyzed, highlighting advantages and disadvantages of both mechanisms, as well as limitations due to carrier-induced heating. Critical aspects of these electro-optically tuned microcavities are then discussed.

5.2 Passive filter design

5.2.1 Filter parameters

Modern optical telecommunication systems require compact passive filters with full widths at half maximum (FWHM) of less than 2 nm, large free spectral ranges (FSR > 10 nm) and high transmitted power (close to 100%).

Our filter is comprised of a Fabry-Perot (F-P) resonant cavity formed between high-reflectance Bragg mirrors. The dominant parameters for the design of Fabry-Perot filters are given by this formula [6]:

$$T = \frac{(1 - R)^2 \cdot \exp(-\alpha \cdot L)}{(1 - R \cdot \exp(-\alpha \cdot L))^2 + 4 \cdot R \cdot \exp(-\alpha \cdot L) \cdot \sin^2(2 \cdot \pi \cdot n \cdot L / \lambda)}, \quad (1)$$

where T is the transmission, R is the reflectivity of the mirrors, α is the cavity losses, L is the resonator length, n is the refractive index of the medium, and λ is the wavelength. The transmission spectrum calculated according to this formula for a 20- μm long cavity is shown in Fig. 1.

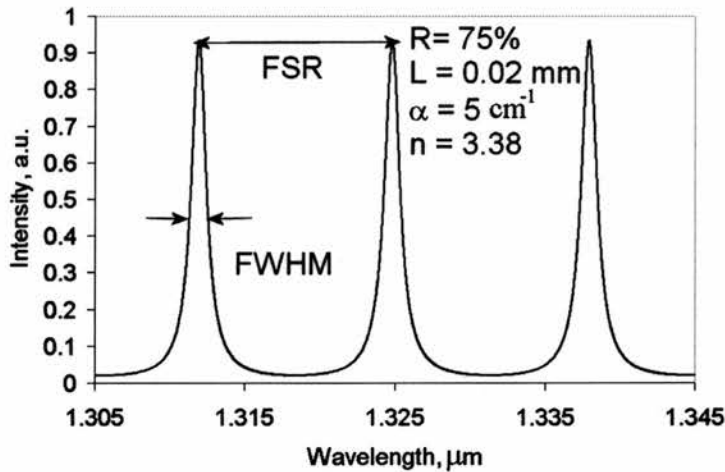


Fig. 1. The theoretical transmission spectrum of a 20- μm long F-P cavity (the other parameters are indicated in the picture) calculated according to the formula (1).

The FSR corresponds to the distance between two successive transmission maxima. The FSR for a given optical resonator length can be approximated as follows:

$$FSR \approx \frac{1}{2 \cdot L \cdot n} \lambda_0^2, \quad (2)$$

where λ_0 is the wavelength of the transmission maximum.

The FWHM for symmetric mirrors can be estimated as

$$FWHM \approx \frac{(1 - R \cdot \exp(-\alpha \cdot L)) \cdot \lambda_0^2}{2 \cdot \pi \cdot L \cdot n \cdot \sqrt{R \cdot \exp(-\alpha \cdot L)}}. \quad (3)$$

The Q-factor is a figure of merit for the quality of the filter:

$$Q - factor = \frac{\lambda_0}{FWHM}. \quad (4)$$

The bigger the Q-factor, the greater the sensitivity of the transmission at the resonance wavelength to even small refractive index changes, so cavities with high Q-factor are desirable, especially for the realisation of active devices.

5.2.2 Bragg resonator as a model for a filter design

As the basic design for the filter, a resonator with deeply etched Bragg mirrors was chosen. The higher the refractive index contrast, the larger the band gap achieved. The maximum refractive index contrast is that between semiconductor and air. Thus, Bragg mirrors comprising air-slots etched in InP were chosen. The well-known “ $\lambda/4$ ” criterion for dielectric Bragg resonators states that each layer in a Bragg mirror should be $\lambda/4n$ thick in order to reach the highest reflectivity. However, using such Bragg mirrors results in very high losses due to diffraction and out-of-plane scattering in the air sections [7]. Fortunately, due to the very high refractive index contrast achievable in these deeply etched structures, one can deviate from this condition and still obtain near 100% reflectivity. Thus, we choose a third order stop-band with air slots of 100 nm according to

$$l_1 n_1 + l_2 n_2 = \frac{3\lambda}{2}, \quad (5)$$

where $l_{1,2}$ is the length of the air/semiconductor section, $n_{1,2}$ is the refractive index in the air/semiconductor section, λ is the free-space wavelength. This method has the side effect of reducing the stop-band width (~ 250 nm); however, for this application it is still well in excess of that necessary. Air slots as small as possible are desirable- we choose

100-nm air-slots as the current practical minimum (this depends not only on the lithography but also on the etching, plus reflection drops if the air-slots are too narrow).

The cavity length must be an integral multiple of $\lambda/2n$, however it must also be sufficiently long to be contacted. Therefore, we start with a design with a 20-um cavity with 2 pairs of air/InP mirrors, in which the air slot is 100 nm. Due to the high index contrast between the air ($n_1 = 1$) and InP-based material ($n_2 = 3.38$), high reflectivity can be achieved with even 2 pairs of Bragg mirrors on each side of the cavity. Fig. 2 presents a schematic view of the filter based on the Bragg mirrors described above (5).

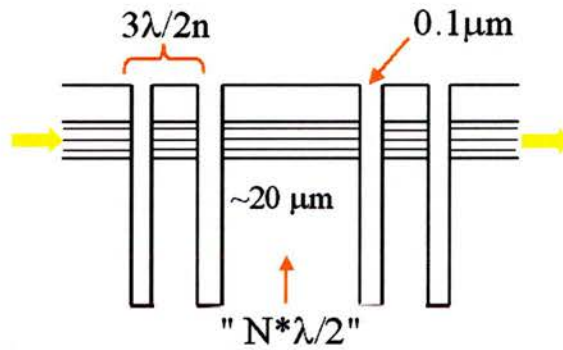


Fig. 2. A schematic view of the filter consisting of the third-order Bragg gratings.

The theoretically calculated (using a transfer matrices MATLAB program) transmission and reflection spectrum for such a resonator with 4 pairs of Bragg mirrors (no cavity) is presented in Fig. 3. The band gap was 250 nm (1225 nm- 1475 nm). Despite having only 4 pairs of the Bragg mirrors, a reflectivity of 97.7 % was obtained.

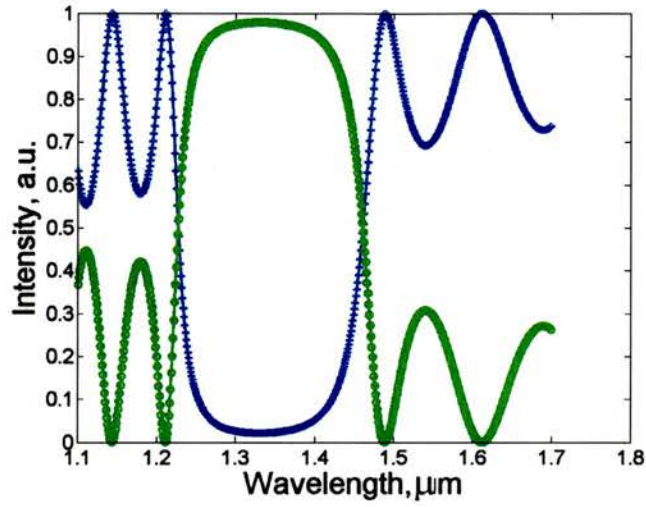


Fig. 3. Theoretical transmission (blue) and reflection (green) spectra for 4 pairs of Bragg mirrors.

In order to create transmission peaks, a semiconductor cavity with a length of $M*\lambda/2n$ ($M=1, 2, 3\dots$) is added. The corresponding transmission spectrum is presented in Fig. 4. The higher the value of M (the longer the cavity), the more transmission peaks are allowed inside the stop-band.

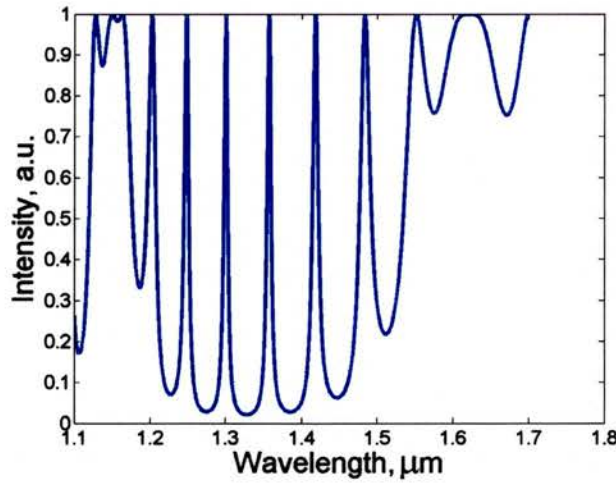


Fig. 4. Allowed transmission peaks for Bragg mirrors with a cavity equal to $M*\lambda/2n$ ($M=15$).

For a cavity of 3 μm length, the FWHM is 7 nm and FSR is 49 nm for the transmission peaks in Fig. 4. A thicker cavity section gives a smaller FWHM. Thus, to comply with the WDM systems criterion of FWHM less than 2 nm [32], the cavity of the filter shall be around 20 μm or longer. However, a longer cavity leads to a smaller FSR, which is undesirable, so a trade-off between minimum possible FWHM and maximum possible FSR shall be found. For a 20 μm cavity ($M=22$) the FWHM is 1.2 nm, the FSR is 12.5 nm and about 16 transmission peaks are present in the stop-band. Note that the same values for filter parameters (FWHM, FSR) can be found from the F-P model described above (see equation (1)) for a 20- μm cavity with 75 % of facets reflectivity (see Fig. 1).

We now make a comparison between the various methods of achieving the desired filter. The allowed tolerance of a fabrication process was estimated to be around + 40/- 20 nm for l_1 in equation (5). In the case of the air-slots with increased widths the FWHM decreases but diffraction losses will increase. If the width of the air-slots is decreased down to 50-nm it results in a large FWHM of 4 nm, losing reflectivity. This is undesirable.

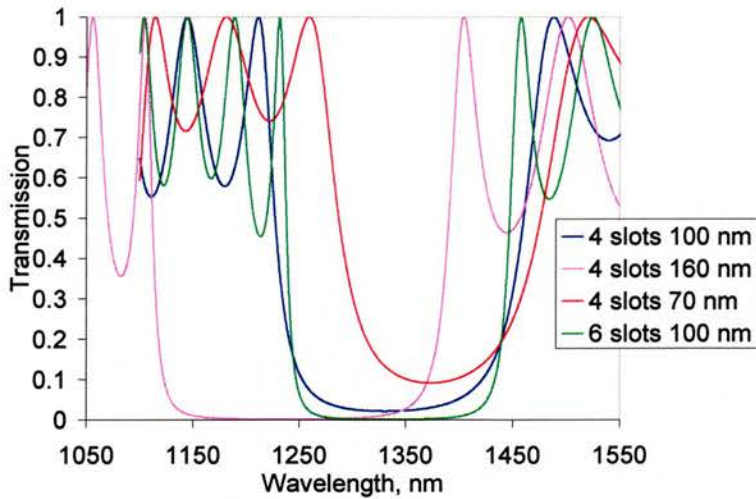


Fig. 5. Band-gaps in transmission spectra for different Bragg mirrors.

The band-gaps in transmission spectrum for different Bragg gratings are presented in Fig. 5, showing changes in the band-gap width and band-gap position for a different number of slots and air slot widths. A summary of the filter parameters for the filters with varying

number of slots and slots widths is given in Table 1. In Fig. 5 and Table 1, the period of the gratings were kept the same, in order to show the allowed tolerance of the fabrication process (changing the period with changing the air slots gives the same plus small shifts of the band-gap).

Table 1. Filter parameters for different Bragg mirrors

Cavity, μm	Number of slots on each side	Width, nm	FSR, nm	FWHM, nm	Width of band-gap, nm	Reflectivity of the whole device
20	2	100	12.5	1.2	365	97.7
20	3	100	12.8	0.4	280	99.7
20	2	160	12.8	0.8	385	99.9
20	2	70	12.7	3	320	88.5
20	2	50	12.7	4	290	75
4.5	2	100	49	7	355	97.7

As shown in Table 1, the filter with a larger number of periods and/or larger air sections widths gives the smallest FWHM. For example, using three 100-nm air-slots on each side of a 20- μm cavity increases reflection of mirrors, making the filter peaks sharper (FWHM= 0.4 nm). At the same time, the diffraction losses of the filter will be increased, resulting in lower transmitted power and a reduction in the obtained Q. Thus, for the filters described in this chapter we choose the minimal amount (two) of 100 nm air-slots on each side of the cavity allowing us to have a theoretical FWHM of 1.2 nm, which is acceptable for WDM systems.

5.3 Quantum confined Stark effect

The aim of this and the following sections is to find ways for realisation of tunable photonic crystal filters. To provide tunability, we must introduce a means of changing the optical path length of the structure. The QCSE and carrier-injection were used to achieve tunability in the devices described in this chapter. Two different quaternary/quaternary

InGaAsP/InGaAsP MQW wafers were designed for the implementation of these methods. This section demonstrates QCSE-based tunable microphotonic filter.

5.3.1 Theory background

The application of an electric field perpendicular to the plane of a quantum well (QW) can influence its optical properties. Among the prominent effects observed is the QCSE [8]. At a zero-field, the QW is treated as a quantum mechanical “particle-in-a-finite-potential” and the electron and the hole have symmetric wave functions (Fig.6 a). When an electric field is applied (Fig. 6 b), band bending occurs, which results in a lowering of the energy band transitions (the electron sub-band energy level drops and the hole sub-band energy level rises). At the same time, the wave functions of the electrons and holes are pulled towards the opposite directions, as illustrated in Fig.6 (b).

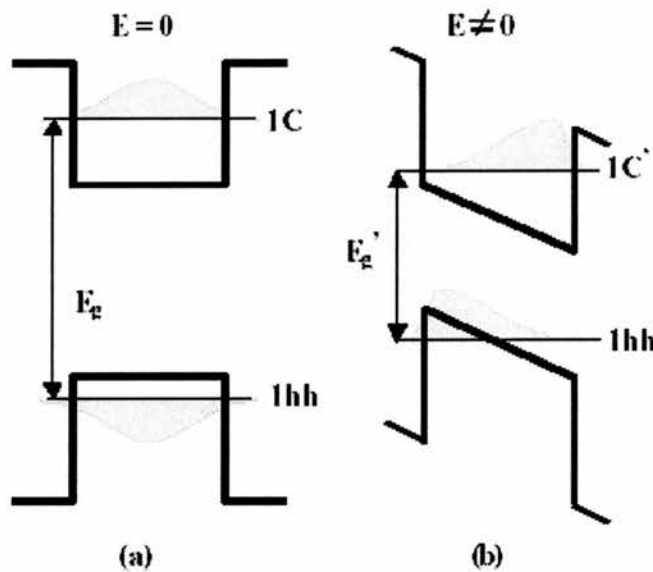


Fig. 6. The band structure of a quantum well without (a) and with (b) an applied E-field perpendicular to the wells. E_g is the bandgap energy and $1hh$, $1C$, $1hh'$, $1C'$ denote the first heavy hole (hh) and electron (C) sub-band energy levels without and with an applied field.

As a result, the band edge absorption is reduced, broadened and shifted to lower energy. An experimental absorption spectrum at different applied voltages for InP-based

MQW modulator [9] is shown in Fig. 7. The peak just above the band edge of the absorption spectrum is called the exciton absorption peak. The electron and hole, attracted to one another by the Coulomb force, create the exciton. The absorption can be considered as the creation of excitons. Thus, the exciton absorption peaks correspond to the direct creation of such excitons by optical absorption. The peaks are below the band-gap energy of the material by the amount of their binding energy. Excitons can be observed in bulk material only at low temperatures. In quantum wells, the excitons are “squeezed”, thus, the overlap between electron and hole is larger. Consequentially, the absorption peak is even stronger and may be observed even at room temperature.

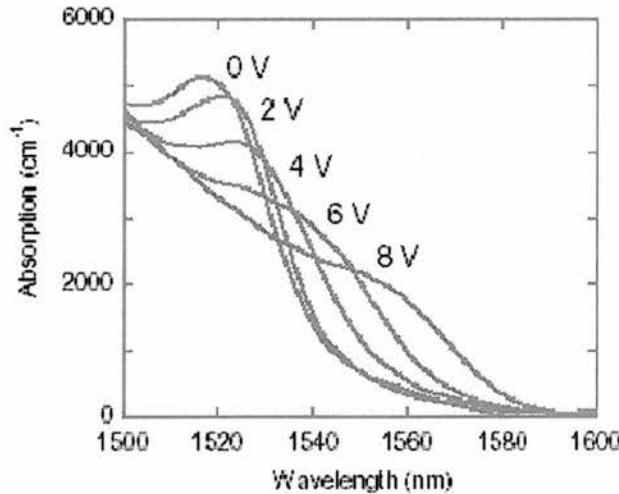


Fig. 7. Measured MQW absorption spectra of InP-based modulator [9].

Changes to the exciton absorption ($\Delta\alpha$) give rise to changes in the refractive index (Δn) via the Kramers-Kronig relations [10]:

$$\Delta n(\omega) = \frac{c}{\pi} P \int_{\omega_1}^{\omega_2} \frac{\Delta\alpha(\omega') d\omega'}{(\omega')^2 - \omega^2} \quad (6)$$

where c is the speed of light, ω is the frequency of light, and P indicates the principal value of the integral.

The changes in the refractive index are the largest near the exciton peak, where absorption is large. Hence, there exists an inherent trade-off between maximizing refractive index changes and minimizing excitonic absorption losses in the design of the tunable filter.

5.3.2 Wafer design

In order to have QCSE-based devices operating at around 1.3 μm , the MQW wafer has to be designed with an absorption spectrum maximum between 1.22-1.25 μm . At a wavelength about 50-nm away from the absorption peak, losses are expected to be tolerable ($\sim 15 \text{ cm}^{-1}$), while QCSE is still clearly pronounced.

Using quaternary/quaternary InGaAsP/InGaAsP QWs and barriers offer choosing the band-gap of the designed material by simple variation of In concentration. Thus choosing material with band-gaps at wavelengths of 1.3 μm and 1.1 μm for QWs and barriers, respectively (see Table 2), we will have a material with an absorption peak at around 1.235 μm (Fig. 8).

Table 2. A wafer design for QCSE.

<i>Repeat</i>	<i>Thickness, nm</i>	<i>Material</i>
1	600	InP
1	354	InGaAsP(Q1.1)
1	76	InGaAsP(Q1.1)
10	6	InGaAsP(Q1.3)
10	76	InGaAsP(Q1.1)
1	430	InGaAsP(Q1.1)
1	1500	InP

A well width of 6 nm was used as narrowing the well results in a rapid reduction in the Stark shift [11]. At the same time, it was important to keep the barrier width large enough to confine the electron and hole to a single well. However, thin barriers are

desirable as they increase the electric field produced across the sample for a given drive voltage. In general, 6-8 nm wide barriers are thick enough to reduce interwell coupling [12], but in fact, we chose extremely thick barriers of 76 nm in order to reduce diffraction losses (see later).

The more QWs are used, the higher overlap (I) with the travelling optical mode, and this produces a higher Stark effect. At the same time, the larger the number of QWs, the higher absorption losses. 10 QWs were chosen for our material, giving a 6 % overlap between the QWs and the electro-magnetic field. Absorption was assumed to be around 15 cm^{-1} away from the peak from the literature [9, 13].

The top and bottom claddings were doped, forming a p-i-n structure. Therefore, the electric field was applied across only the intrinsic layer ($1.6 \mu\text{m}$ thick). The wafer grown at the University of Sheffield showed the photoluminescence spectrum depicted in Fig. 8, illustrating that an absorption maximum is at $\sim 1235 \text{ nm}$.

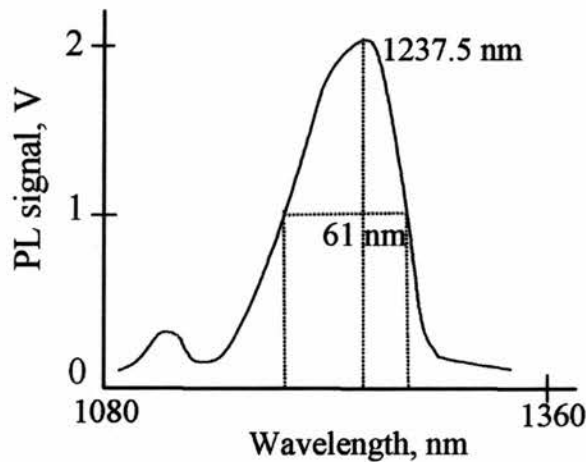


Fig. 8. Photoluminescence (PL) spectrum of the wafer MR 1913 7171, performed at the University of Sheffield.

5.3.3 Three-dimensional modelling: diffraction losses

A commercial software package called FIMMPROP/FIMMWAVE (Photon Design), based on eigenmode value expansions [14], was used in order to calculate the expected losses of the filter. The program calculates losses as the coupling efficiency between air modes and the guided mode in the semiconductor heterostructure (mode

mismatch). According to the model, for the best results, a thick WG with an even distribution of qwells is desirable since it flattens mode profile.

This thick core (equivalent to a weak vertical confinement) minimises diffraction losses at the air/semiconductor interfaces. Similar results were reported by W. Bogaerts *et al.*, [15] for 1-D PhCs, illustrating that weak vertical confinement reduces diffraction losses due to a flatter mode profile. In agreement with these predictions, we have also measured low losses in 2-D photonic crystals fabricated in this material (see Chapter 4).

FIMMPROP, however, models the air sections as slots of the “infinite” depth (in the sense that there is no substrate at the bottom of air sections). Thus, this software is unable to predict additional losses in the air-sections connected with the finite depth of the slot, which results in scattering of the travelling light to the substrate. Therefore, a finite-difference time-domain (FDTD) 2-D simulator for photonic devices [16] was used in order to calculate the etch depth required to have minimal scattering of the light to the substrate modes.

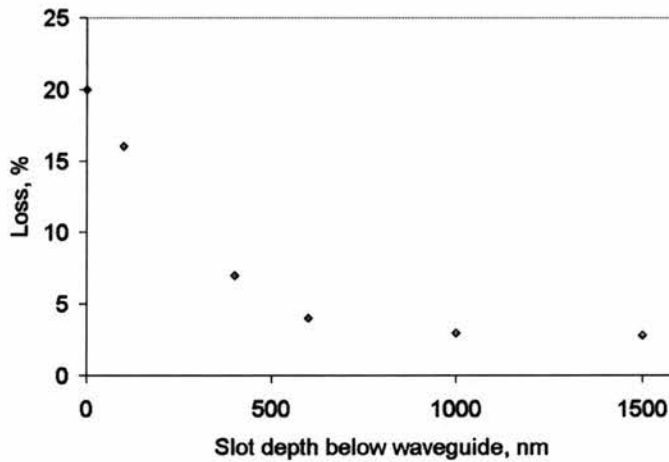


Fig. 9. The calculated transmission spectrum via an etch depth for a filter with a 1.6- μm waveguide.

Fig. 9 indicates that the slots etched to 600 nm below the waveguide are sufficient for an almost lossless propagation. However, since the program models the air-slots with ideal vertical walls, an additional 1-3 μm of the etch depth seems advisable in practice. This is due to the nature of the etched slots in InP, which exhibits tapered bottoms.

5.3.4 Operation in a single lateral mode

The following calculations were performed to determine conditions for single transverse mode operation. Shallow etched waveguides are the means of keeping thick waveguides single-moded (shallow etching means that the etching does not go through the waveguide core). This creates weak lateral confinement that confines only the first-order mode with the second-order mode leaking. The necessary etch depth for this to occur depends on the ridge waveguide width and the core thickness.

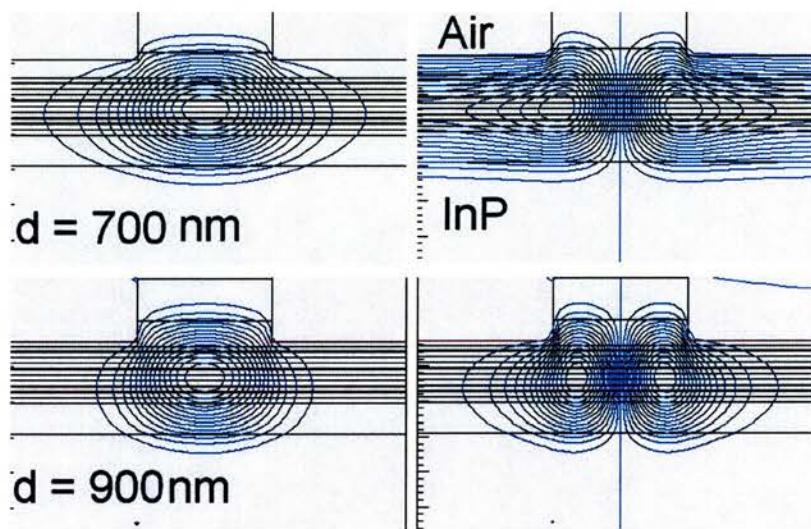


Fig. 10. First- and second-order mode profiles of the filter for two different etch depths modelled by FIMMWAVE.

Fig. 10 shows the profiles of the first- and second-order modes for two different etch depths of a 5- μm wide ridge waveguide. As one can see from these calculations, in order to keep the 5- μm wide waveguide single-moded it should be etched to a depth of 700 nm (or less).

For wider ridge waveguides, the maximum allowed etch depth for the single-mode operation decreases. For a 10- μm wide waveguide, for example, an etch depth of 550 nm produces a waveguide supporting only a single-mode.

It is useful to note that due to the thickness of the core of 1.604 μm , it can, unfortunately, also support undesirable vertical modes. In practice, however, it is hard to launch light into such a second-order vertical mode.

5.3.5 Fabrication of quantum confined Stark effect–based tunable filters

QCSE–based filters, described above, were successfully fabricated. A detailed description of the fabrication process is presented in Chapter 2. Here, only a summary of all fabrication steps performed for a tunable filter via QCSE realisation is given.

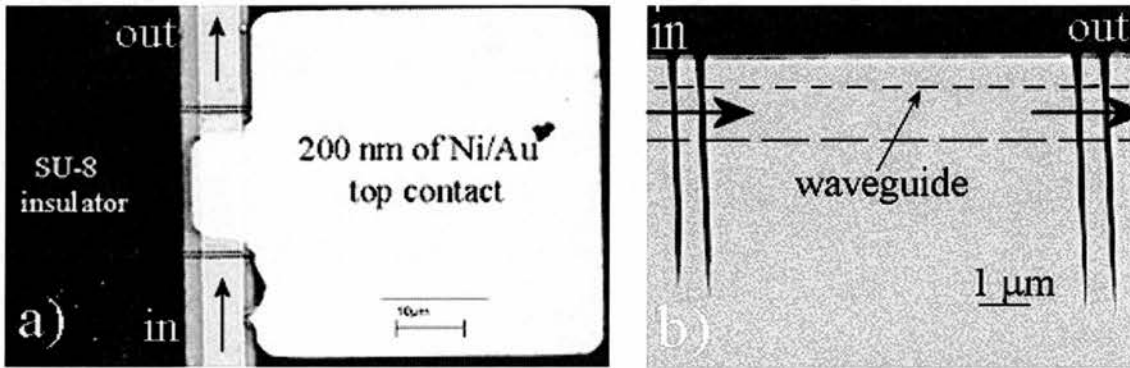


Fig. 11. A SEM image of a QCSE-based filter: a) top view, b) a cross-section of the slots etched to the depth of 5 μm using CAIBE.

100-nm air slots were electron-beam written in a PMMA. They were transferred into a SiO_2 hard mask using RIE with fluorine chemistry. Using the highly effective CAIBE technique of etching high-aspect ratio features in InP-based material described in Chapter 3, deep straight air-slots (Fig. 11 b) were etched with aspect-ratios of approximately 35:1. These deep, straight and smooth air-slots are necessary in order to minimize scattering losses from imperfections in the walls and the coupling of propagating light into substrate modes.

Photolithography and a second-stage shallow etch (CAIBE) was used to create single mode waveguides (5- μm wide). Contact insulation was created in SU-8 via optical photolithography. Contacts were deposited, consisting of 20/200 nm of Ni/Au for the top and 14/14/14/11/200 nm of Au/Ge/Au/Ni/Au for the bottom contacts. The top contact was defined using photolithography and a lift-off technique (Fig. 11 a).

5.3.6 Experimental results and analysis

The measurement set-up was similar to that used for the 2-D PhC loss measurements described in Chapter 4, with just some alterations. A tunable laser operating between 1250-1365 nm was used to launch light into the device via an optical fibre. The substrate was mounted to an aluminium heat-sink mount using a silver epoxy. The output light was collected via an optical lens and passed through a polarizer (to select TE polarisation) placed before a detector.

First of all, passive filters were tested. These are filters without contacts and insulation and are, thus, relatively easy fabricated. The transmission spectrum of one such filter with a 20- μm cavity is presented in Fig. 12, exhibiting FWHM of less than 2 nm and FSR of 11 nm.

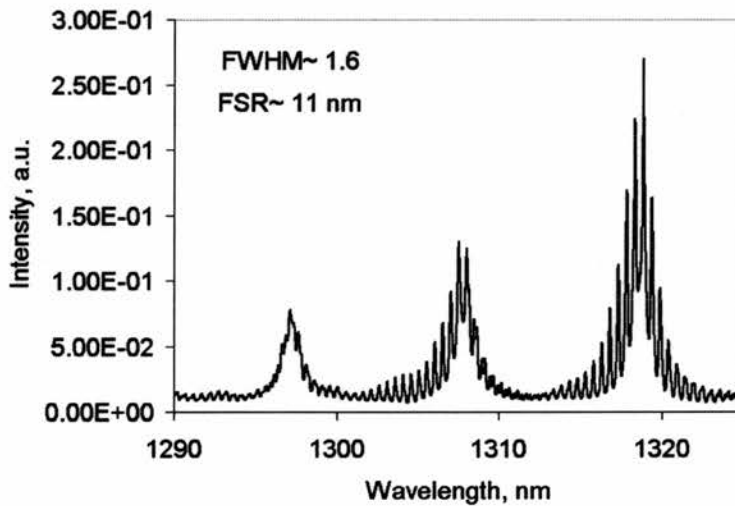


Fig. 12. An experimental transmission spectrum of the passive filter with a 20- μm long cavity.

The height of the experimental transmission peaks is strongly influenced by the absorption spectrum of the material, which has a peak of absorption at 1235 nm. The multiple ripples inside the filter peaks in Fig. 12 correspond to the cavity formed by the cleaved facets.

We then moved on to devices with contacts in order to look for electro-optic tuning. A transmission spectrum of a tunable filter with and without applied reverse bias of 8 V is illustrated in Fig. 13. At 1285 nm, a red-shift of 0.9 nm was obtained. The closer to the band-edge (1235 nm), the bigger the shift, as one can see from the figure where a red-shift of 1.5 nm was observed at the wavelength of 1265 nm.

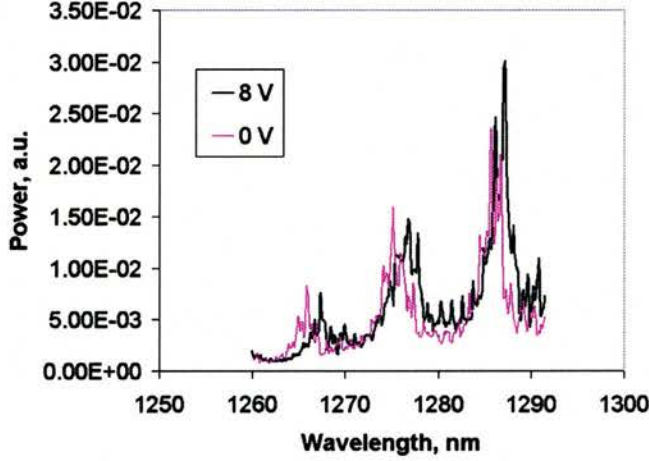


Fig. 13. The observed transmission spectrum with and without applied reverse field of 8 V.

The relationship between the experimentally observed red-shifts and the refractive index changes can be derived from the condition for transmission maximum:

$$N \frac{\lambda_0}{2} = nL, \quad (7)$$

where n is the effective refractive index, L is the cavity length, N is an integer, and λ_0 is the wavelength of maximum transmission. Thus,

$$\frac{\Delta n}{n} = \frac{\Delta \lambda}{\lambda_0}. \quad (8)$$

The electro-optic behaviour of the device can be described by an electro-optic parameter η [17]:

$$\eta = \Delta n \Delta \omega / E^2, \quad (9)$$

where $\Delta\omega$ is the energy detuning from the band gap; Δn is the refractive index changes; and E is the applied electric field. This parameter was introduced by J. E. Zucker *et al* [17] from the observed experimental dependences, such as $\Delta n \sim 1/\Delta\omega$ and $\Delta n \sim E^2$.

This parameter η can be useful for the prediction of changes in the refractive index for different wavelengths and/or applied voltages for a given well width. In our case, we found the electro-optic parameter to be $4 \cdot 10^{-5} \text{ meV cm}^2 \text{ kV}^{-2}$, using the shift of the resonator peak at a wavelength of 40 meV below (corresponding to a wavelength of 1285 nm) the gap edge and an applied voltage of 8 V. Fig. 14 shows good agreement between the predicted refractive index changes and those found from the experiment (for the applied field $E = 50 \text{ kV/cm}$)¹.

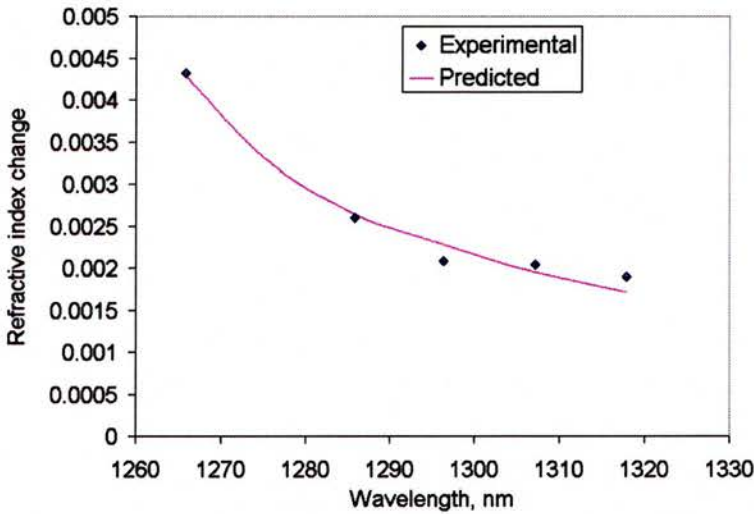


Fig. 14. The experimental and predicted refractive index changes at applied field $E = 50 \text{ kV/cm}$.

For the best device, however, this electro-optic parameter was improved by a factor of three, reaching a value of $14 \cdot 10^{-5} \text{ meV cm}^2 \text{ kV}^{-2}$. This parameter was calculated from an experimental shift of 1.2 nm at $E = 37.5 \text{ kV/cm}$ and $\Delta\omega = 64 \text{ meV}$ illustrated in Fig. 15.

¹ The electric field was found for a given applied voltage by dividing it by the intrinsic region width. We assume an even charge distribution.

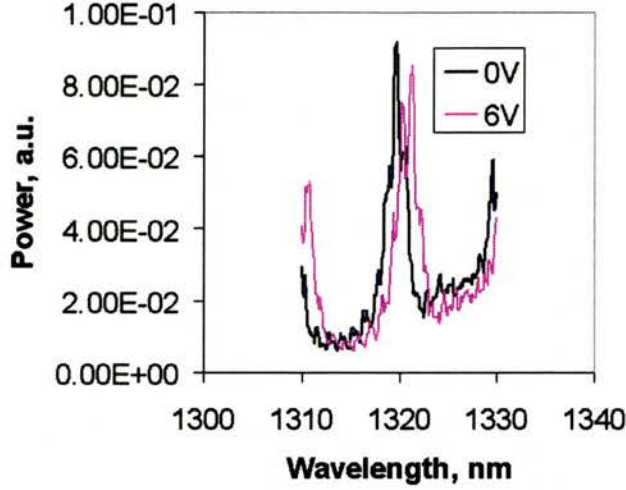


Fig. 15. The observed 1.2 nm red-shift at 1319 nm with only $E= 37.5$ kV/cm applied.

This means that the previously mentioned value for η was not limited by the QW structure design but rather by some fabrication imperfections and, thus, was an intrinsic feature of only that particular device. Using this parameter we can predict a shift as big as 5 nm at the wavelength of 1265 nm applying only $E = 50$ kV/cm.

Good agreement was also obtained between the predicted and experimentally observed shifts at 1319 nm at an applied voltage of 3 V. Using this electro-optic parameter we can express the refractive index change as a function of the applied electric field. The refractive index is also connected with the electric field via linear (r) and quadratic (s) coefficients in the following form [17, 18]:

$$\Delta n = -\frac{1}{2} n_0^3 (rE + sE^2), \quad (10)$$

where n_0 is the refractive index in the absence of an electric field.

Bearing in mind that the linear dependence of the refractive index on the electric field is weak, we can neglect it in order to find the quadratic electro-optic coefficient using equations (9) and (10).

We found s to be $-10 \cdot 10^{-14} \text{ cm}^2/\text{V}^2$ for an energy detuning of 64 meV from the band-edge. The same quadratic coefficient was found as a fitting parameter to the experimental data (for a different device) of refractive index changes as a function of the

field applied. This value compares favourably to the value of $-1 \times 10^{-14} \text{ cm}^2/\text{V}^2$ reported in a ring resonator configuration at 60 meV from the band-edge reported elsewhere [19].

For comparison, the quadratic coefficient s of $-2.5 \times 10^{-14} \text{ cm}^2/\text{V}^2$ was obtained experimentally for filters fabricated in a material with 5 quaternary InGaAsP QWs (at $\Delta\omega = 48 \text{ meV}$) (this material was designed for carrier-injection-based filters, see later).

At an applied field of 38 kV/cm and $\Delta\omega = 64 \text{ meV}$, the efficiency, $\Delta n/E = 820 \times 10^{-12} \text{ m/V}$ was found experimentally. This is of the same order as results reported elsewhere [17] $\Delta n/E = 806 \times 10^{-12} \text{ m/V}$ but for a wavelength closer to the band-edge ($\Delta\omega = 44 \text{ meV}$) and a higher applied field ($E = 100 \text{ kV/cm}$). These high figures of merit underline the high quality of our material and fabrication.

It is worth mentioning that due to the small dimensions of QCSE-based filters, the theoretical device time response of our device is very low ($\sim \text{ps}$). As is well known from the theory of semiconductor devices, a $p-i-n$ diode can be replaced by the equivalent electrical circuit with a series resistance R_s and the diode capacitance C_D , which control the device time response through the following relationship: $t = R_s C_D$. The diode capacitance C_D for the reverse bias case is as follows: $C_D = \frac{\epsilon A}{w}$, where ϵ is the dielectric constant of the intrinsic region, A is the area of the diode, w is the thickness of the intrinsic region. Thus, calculating the diode capacitance for our case and using an estimated series resistance R_s of 20 Ohms (from the experimental $I-V$ curves) we can predict the theoretical response time of our QCSE-based device to be about 15 ps. This is rather low and very favourable for modern high-speed circuits.

5.4 Carrier-injection

In this section, we report on the fabrication and characterization of 20 and 40- μm -long carrier-injection-based tunable F-P type filters in a five-quantum-well InGaAsP/InGaAsP material. Due to the relatively low surface recombination velocity of InP-based material [20] and good heat sinking, successful tuning of the cavity resonance was achieved using carrier injection. For higher currents, however, thermal effects are observed that reverse the wavelength shift.

5.4.1 Theory background

Carrier-injection changes the refractive index through three effects: bandfilling, band-gap shrinkage, and free-carrier absorption (plasma effect).

The bandfilling effect is based on a decrease in absorption for photon energies near the band-gap, which results from an increase in carrier concentration.

Assuming a parabolic band, the optical absorption near the band-gap is given by the square-root law [21]:

$$\Delta\alpha(N, P, E) = \sum_{\sigma} \frac{C_{\sigma}}{E} \sqrt{E - E_g} \{f_v[E_{i\sigma}(P)] - f_c[E_{f\sigma}(N)] - 1\}, \quad (11)$$

where N and P are the free electrons and holes concentrations, respectively, E is the photon energy, and E_g is the bandgap energy. The sum is performed over the light-hole and heavy-hole bands σ , where C_{σ} is a constant defined by the appropriate matrix element, f_v and f_c are the Fermi-Dirac distribution functions for the valence and conduction bands, respectively, and $E_{i\sigma}$ and $E_{f\sigma}$ are the initial and final states corresponding to band σ , see Fig. 16.

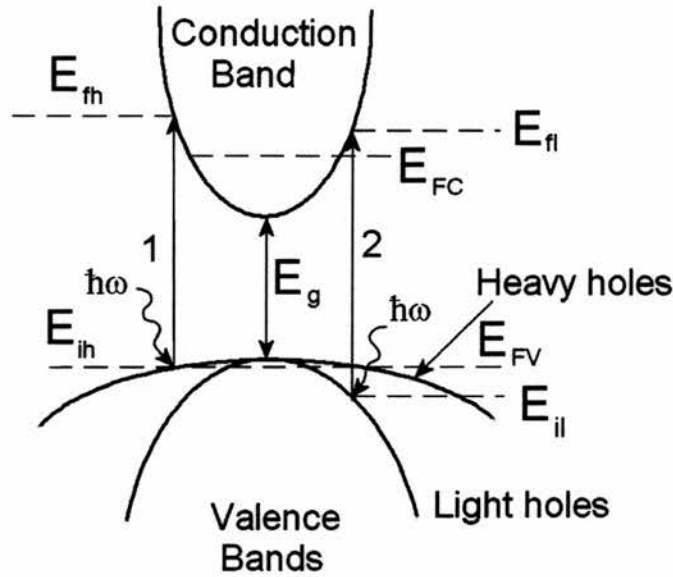


Fig. 16. Energy band structure and bandfilling effect for the semiconductor. Absorption of a photon can occur only between occupied valence band states and unoccupied conduction band states. Transitions involving heavy and light holes are denoted by 1 and 2, respectively. E_{FC} and E_{FV} are the carrier-dependent quasi-Fermi levels [22].

The change in the absorption begins at the band-gap and decreases for energies well above the gap. The corresponding change in the refractive index is calculated through the Kramers-Kronig relations. The refractive index change decreases for energies near and below E_g , and becomes positive for energies well above E_g . The perturbation of the refractive index approaches zero for energies far above or below the bandgap.

Bandgap shrinkage occurs when injected electrons occupy states at the bottom of the conduction band and when their concentration is large enough, so the electron wave functions will overlap, and forming a gas of interacting particles. The electrons will repel one another by Coulomb forces. In addition, electrons with the same spin will avoid one another for statistical reasons. The net result is a screening of electrons and a decrease in their energy, lowering the energy of the conduction band edge. A similar effect for the holes increases the energy of the valence band edge. The sum of these effects results in band-gap shrinkage. These shrinkage effects are determined by the free-carrier density,

and are nearly independent of impurity concentration. The estimated shrinkage is proportional to the cube-root of the carrier concentration. This law is valid only for carrier concentrations bigger than the critical value, which is around 3×10^{17} $1/\text{cm}^3$ for InP material. As in the case of bandfilling, the largest changes in refractive index occur near the bandgap. Unlike bandfilling, however, Δn is positive for energies below the bandgap, a result of the increase in the absorption coefficient for fixed energies.

The free-carrier absorption (the plasma effect) results from the free charge carrier absorption in either the conduction band or the valence bands. A free carrier absorbs a photon and moves to a higher energy state within the band. According to the Drude model, the change in the refractive index is given by [22]:

$$\Delta n(N, P) = \frac{-e^2 \lambda_0^2}{8\pi^2 c^2 \epsilon_0 n_0} \left(\frac{N}{m_e} + P \frac{m_{hh}^{1/2} + m_{lh}^{1/2}}{m_{hh}^{3/2} + m_{lh}^{3/2}} \right), \quad (12)$$

where e is the electron charge, c is the speed of light, ϵ_0 is the permittivity of the vacuum, n_0 is the unperturbed refractive index, m_e is the effective mass of the electron, m_{hh} is the effective mass of the heavy hole, m_{lh} is the effective mass of the light hole, and N and P are the free electrons and holes concentrations, respectively.

The sign of Δn from the plasma effect is always negative; hence, it will add to bandfilling for energies below the bandgap. Because of the λ^2 dependence, the plasma effect increases as the photon energy is decreased below the bandgap.

The relative magnitudes of the three effects are illustrated in Fig. 17, which shows each effect and the total for the electron-hole pairs in InP for a concentration of 3×10^{18} $1/\text{cm}^3$.

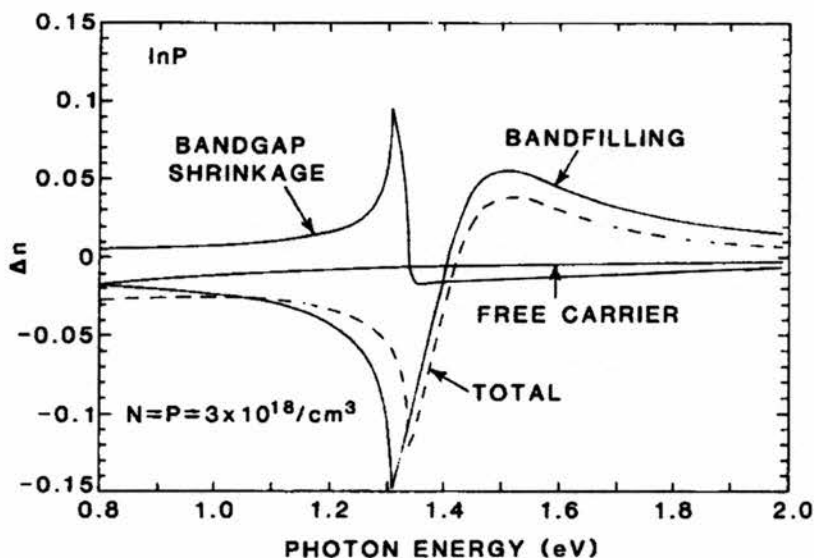


Fig. 17. Predicted changes in the refractive index from bandfilling, bandgap shrinkage, and free-carrier absorption for injection into InP [22].

5.4.2 Carrier-injection based device description

An MQW wafer was designed for a realisation of a tunable filter using carrier injection. 5 quaternary/ quaternary InGaAsP/InGaAsP qwells with a band-gap at 1.3 μm were used. The wafer description is presented in Table 3.

According to the carrier-injection theory described above, the refractive index changes at wavelengths around 1.3 μm for a material with the band-gap at 1.25 μm will be dominated by the bandfilling effect.

The wafer (MR 2024 7838) has, as a top layer, a highly doped InGaAs material. Since InGaAs is not transparent at 1.3 μm , this top layer is kept small (10 nm) in order to minimize light absorption. The purpose of this InGaAs layer is to improve the ohmic contact formation between the semiconductor material and the p-type contact pads.

Table 3. A wafer design for carrier injection

<i>Repeat</i>	<i>Thickness, nm</i>	<i>Material</i>	<i>n</i>	<i>Type</i>
1	10	InGaAs		p(contact layer) $\approx 1 \cdot 10^{19} \text{ cm}^{-3}$ (Zn)
1	600	InP	3.195	p: $5 \cdot 10^{17} \text{ cm}^{-3}$ (Zn)
1	150	InGaAsP(Q1.02)	3.3	
1	8	InGaAsP(Q1.1)	3.39	
5	6.5	InGaAsP(Q1.3)	3.67	
5	8	InGaAsP(Q1.1)	3.39	
1	150	InGaAsP(Q1.02)	3.3	
1	1500	InP	3.195	n: $5 \cdot 10^{17} \text{ cm}^{-3}$ (Si)

As in the case of QCSE-based filter, this device consisted of a cavity (20 μm or 40 μm length) defined by third-order Bragg mirrors (air-slots). The process of air-slots fabrication is identical to the one used for the QCSE tunable filter (see above). The ridge waveguides, insulation, and contact pads were e-beam written (using three-point alignment, described in Chapter 2). E-beam lithography was chosen for this filter out of the necessity of using a different type of contact pad for the carrier injection device. Square contact pads were used for carrier-injection due to the fact that some of the “T-shaped” contacts (shown in Fig. 11) burnt out at the interface between the insulated and non-insulated section under forward biases. This type of contact insulation is required everywhere apart from the top of the cavity region. In order to leave such a small window in the insulation on top of the cavity, e-beam lithography is a better candidate due to its higher resolution and alignment accuracy ($\sim 100 \text{ nm}$). A SEM image of a filter prior to contact evaporation is given in Fig. 18. Finally, a Ni/Au top contact in the shape of big squares 100 x 80 μm wide and an Au/Ge/Ni bottom contact were evaporated.

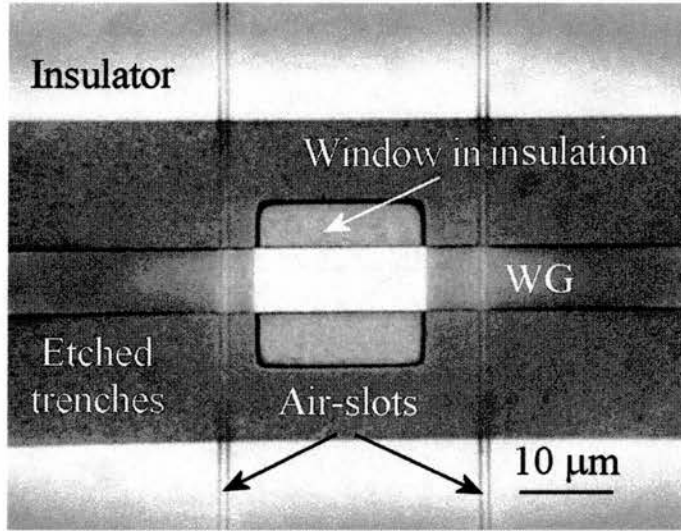


Fig. 18. Top view of the filter with a 20- μm cavity prior to contact evaporation. The 5 μm ridge WG, SU-8 insulator and air-slots for mirrors are clearly indicated.

As before, to obtain operation in the regime of a single transverse mode, shallow etching of the ridge waveguides was performed via CAIBE. Since the core size of the carrier-injection wafer was much smaller (0.38 μm) than that of the QCSE wafer (1.604 μm), a smaller etch depth for the waveguide ridge was required to confine a single mode only. According to FIMMWAVE, etch depths between 150 and 250 for 5- μm wide waveguide will confine a single mode only for a 380 nm thick waveguide. At the same time, such a narrow low-index-contrast WG does not support any higher order vertical modes.

Due to the reduced size of the waveguide core, the required etch depth for these air-slots was also less than for the wafer designed for QCSE. This etch depth, according to the modelling (FDTD), was around 3 μm . Taking into account the tapered bottoms of the slots obtained in practice, the etch depth should be between 3.5 and 5 μm .

5.4.3 Experimental results and discussion

A typical set-up identical to the one used for the QCSE-based filters was used. The experimental transmission spectrum of the device with a 40 μm cavity with a FWHM of less than 2 nm is presented in Fig. 19. The FSR is about 6 nm, as expected from the

model (FIMMPROP). In order to have a larger FSR, smaller cavities can be used. 20- μm long cavities, exhibiting an FSR of 12 nm, were, thus, also fabricated in this material. The height of the experimental transmission peaks is strongly influenced by the absorption spectrum of the material, which has a peak of absorption near 1250 nm, similar to the QCSE-based filter.

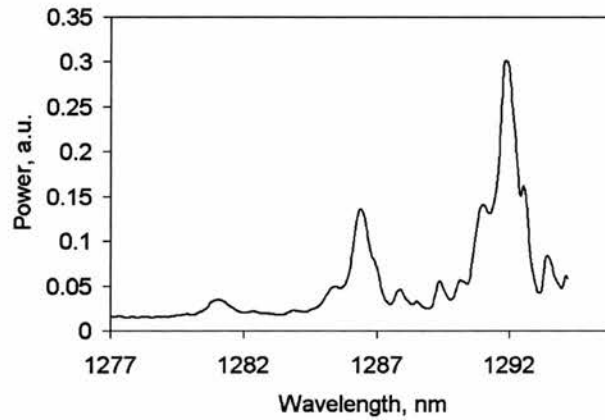


Fig. 19. The transmission spectrum of a passive filter with a 40- μm cavity, exhibiting a FWHM around 2 nm and a FSR of 6 nm. The proximity to the absorption peak of the material near 1250 nm affects the height of the transmission peaks.

Applying a forward bias to the cavity, (the access waveguides were left un-pumped) creates carriers which are mostly collected inside the 5 qwells. This causes changes in the effective refractive index of the waveguide. For carrier densities¹ of around $3 \cdot 10^{18}/\text{cm}^3$ and close to the bandgap, the band-filling effect is predominant and provides the largest contribution to the refractive index changes (see Fig. 17).

¹ The carrier density (N) can be obtained from the carrier rate equation [23], resulting in the following simple formula $N = I\tau(Vq)^{-1}$, where I is the current, τ is the carrier life time, V is the volume (including carrier spreading), q is the electron charge.

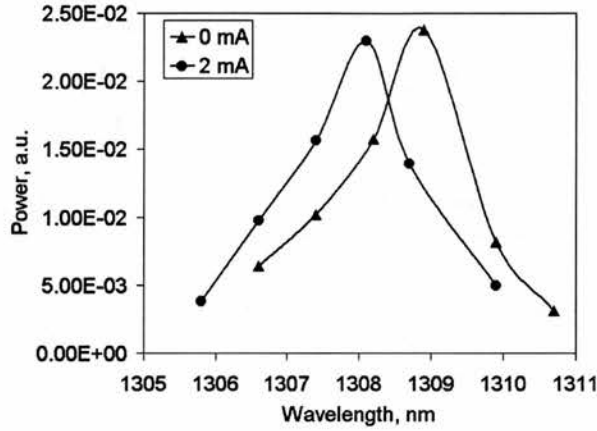


Fig. 20. A blue-shift of 0.7 nm for an injected current of 2 mA. The filter has a cavity length of 40 μm .

Fig. 20 shows the measured carrier-induced blue shift of a single filter peak. A shift of about 0.7 nm at 1309 nm was observed in the device with a 40- μm long cavity for an injected current of 2 mA. However, we failed to observe greater shifts of the transmission peak towards shorter wavelengths at higher currents. In fact, a reduced shift of 0.6 nm was observed for an injection current of 10 mA. This shift in the opposite direction can be explained by heating effects in the micro-cavity, as the thermally induced refractive index change has the opposite sign to that of the carrier -induced shift (Fig. 21).

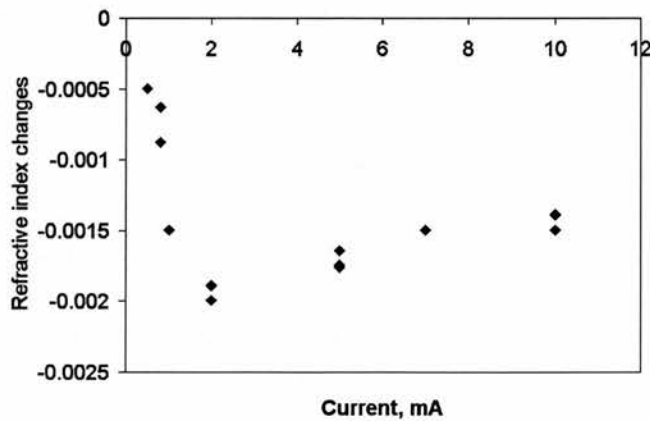


Fig. 21. Carrier-injection modal refractive index changes induced in a 40- μm cavity filter. A pronounced thermally induced shift in the opposite direction appears after 2 mA.

As shown in Fig. 21, the refractive index decreases up to a tuning current of about 2 mA and then increases again for higher currents. We believe that this change of direction occurs because of the onset of lasing at about 2 mA, which was verified independently (see section 5.4.4). At the lasing threshold, the carrier density is clamped, so no further carrier-induced refractive index change can be expected. In our case, the blue shift of the transmission peak will, therefore, not exceed 0.7 nm, which corresponds to an Δn of -0.025 in the quantum wells or a modal Δn of 0.002, taking the overlap factor of 8 % into account. Increasing the current further, then, causes thermo-optical effects that are opposite in sign, thereby reducing the observed shift. The rise in cavity temperature (ΔT) is connected with the power dissipated (P_d) in the cavity of the filter by: $\Delta T = R_{th} * P_d$ [23], where R_{th} is the thermal resistance of the device. At the same time [24]:

$$dn/dT = K_{TO}, \quad (13)$$

where K_{TO} is the thermo-optic coefficient. Thus, knowing K_{TO} for InGaAsP (typically around $2 * 10^{-4} \text{ K}^{-1}$ [24]), ΔT can be derived as a function of the dissipated power from the experimental data of Δn versus I (presented in Fig. 21). From the slope of the curve in Fig. 22 the thermal resistance of 0.2 K/mW can be calculated.

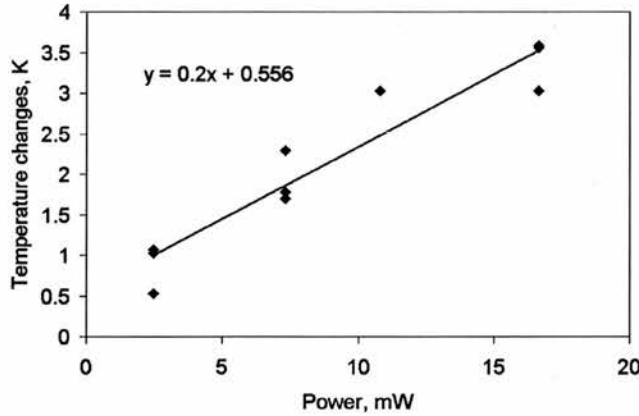


Fig. 22. Experimentally observed dependence of the cavity temperature change vs. dissipated power for a 40- μm cavity filter.

This resistance is less than half of the theoretical value of 0.5 k/mW extracted from the two-dimensional approximation of heat dissipation in the following form [26]:

$$R_{thermal} = \frac{\ln(\frac{4h}{w})}{\pi * K * L}, \quad (14)$$

where h is the thickness of the wafer, w is the lateral dimension of carrier spreading, K is the thermal conductivity of InP, and L is the cavity length. This approximation is valid when the total thickness of the wafer is well in excess of the size of the heat source.

We believe that the values of the thermal resistance (within experimental error) are smaller than theoretically predicted due to heat dissipation by the top contact pad which was deliberately oversized, thereby acting as a “cooling fin” [25].

As one can see from Fig. 21, the rate of change of the transmission peak shift for the filter with 40- μm cavity is $(\Delta\lambda/I) = 0.36 \text{ nm/mA}$. This value exceeds the value of $\sim 0.09 \text{ nm/mA}$ for the InGaAsP/InP FP cavity reported by H. K. Tsang *et al.* [26] and is of the same order as that reported by S. J. Choi *et al.* [27].

Tunable filters with shorter cavity lengths (20 μm) were also investigated (Fig. 23). One of the advantages of this shorter cavity is the larger FSR (of 12 nm). The smaller cavity length also has a higher threshold current density (see below for more detailed explanations), allowing the injection of more current into the device for tuning without reaching the threshold current density, thus, providing an increased carrier density. Thus, a blue-shift of 1.5 nm was experimentally observed at a wavelength of 1288 nm for an injected current of 2.7 mA. However, at the same time the heating effect is more severe for smaller cavities due to their increased thermal resistance. The experimentally extracted thermal resistance for the 20 μm cavity is about 0.4 K/mW (the theoretical value is 1 K/mW). This is two times larger than that of the 40- μm cavity, as expected from equation (14).

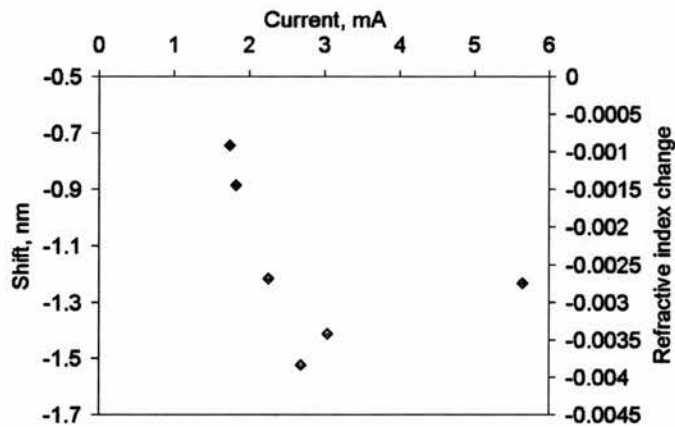


Fig. 23. Carrier-injection refractive index changes induced in a 20- μm cavity filter.

Pulsed currents (10 μs pulse width for 1000 μs period) were used in order to reduce the heating problem, and a blue-shift of 1.9 nm was obtained for an injection current of 2.69 mA. The difference between this value and the 1.5 nm blue shift obtained by the direct currents (DC) measurement, above, agrees well with the red shift (0.3 nm) caused by heating (calculated using the experimental thermal resistance of 0.4 K/mW measured above).

Several effects impact the effectiveness of the carrier-induced index changes. The lateral spread of the current, the low overlap between the optical mode and the QWs ($\Gamma \sim 8\%$) and the surface recombination of the carriers at the etched sidewalls minimize the overall refractive index changes we were able to observe.

5.4.4 Lasing characteristics of the cavities

In order to prove the assumption we made for the calculation of the thermal impedance, namely, that lasing takes place at ~ 4 mA and ~ 2 mA, for 20- μm and 40- μm long cavities, respectively, we performed some additional independent experiments and modelling.

We start from a basic theoretical model of the semiconductor lasers. According to this model, the threshold current density as the function of the cavity length is given by [28]:

$$\ln J_{th} = \frac{1}{L} \left(\frac{\ln \frac{1}{R}}{n_w \Gamma_w g_0} \right) + \left[\frac{\alpha_i}{n_w \Gamma_w g_0} + \ln \frac{J_0 n_w}{\eta_i} - 1 \right], \quad (15)$$

where J_{th} is the threshold current density, L is the cavity length, R is the facet reflectivity, n_w is the number of wells, Γ_w is the confinement factor, η_i is the internal quantum efficiency, J_0 is the current density corresponding to the optimum gain, α_i is the loss per cm, and g_0 is the optimum gain per cm. R and Γ_w , calculated via FIMMWAVE, equal 75 % and 1.6 %, respectively, and J_0 , η_i , α_i and g_0 are available in the literature [13, 29]. The dependence of the threshold current on the cavity length is presented in Fig. 24, calculated using (15) with typical parameters.

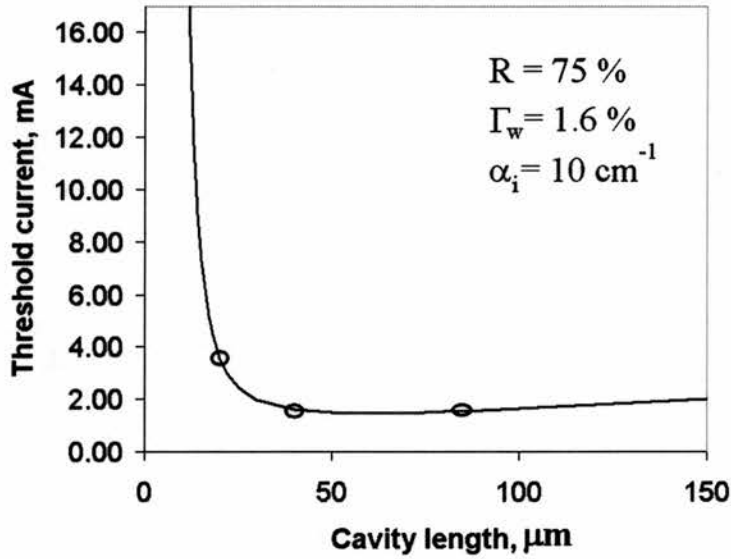


Fig. 24. Theoretical threshold current vs. cavity length, modelled using typical parameters reflecting the experimental situation. The dots correspond to the cavity lengths of 20, 40 and 80 μm examined in our experiments.

At the same time, we carried out additional experiments showing a lasing of 20- and 40- μm long cavities. For these purposes, we cleaved close to one of the mirrors ($\sim 50 \mu\text{m}$), in order to launch the out put light into a detector (otherwise, it gets strongly absorbed by the access waveguide). Fig. 25 shows the experimental “P-I” curve for a 40- μm long cavity. It illustrates that there is indeed the lasing threshold at around 4 mA. The

lasing threshold for an 80- μm cavity was observed at the same 4 mA current. This agrees with the theoretical data presented in Fig. 24, predicting that the threshold currents for the 40- and 80- μm cavity are almost the same.

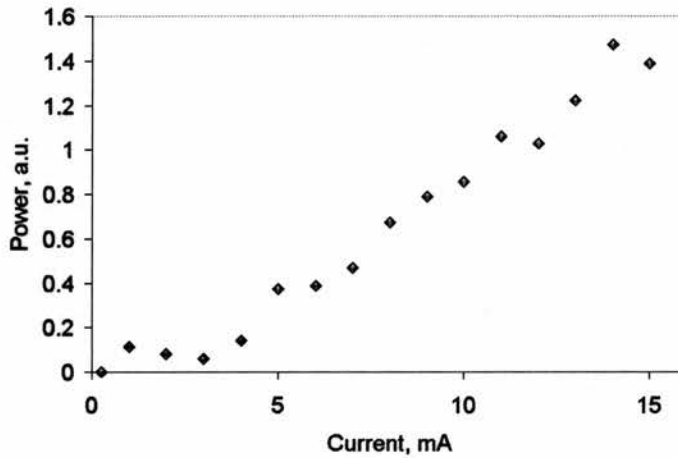


Fig. 25. P-I curve for a 40- μm long laser

In addition, the transmission peaks shifts of the filter with the 40- μm cavity, exhibiting this lasing threshold of around 4 mA, were experimentally observed. The corresponding refractive index changes are presented in Fig. 26 showing thermal “tail” starting around 4 mA which matches (see Fig. 25) the lasing threshold of this cavity reported above. Thus, the assumption that the lasing threshold corresponds to the start of the heating “tail” appears to be correct.

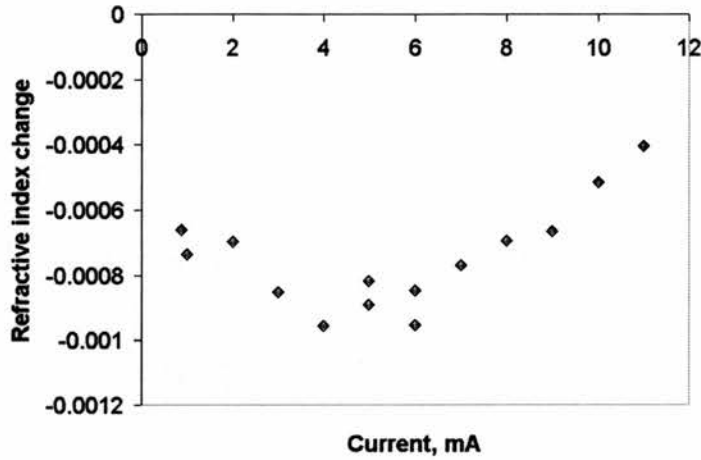


Fig. 26. Refractive index changes corresponding to the 40- μm long filter (the corresponding P-I curve of the same device is presented in Fig. 25).

Moreover, the thermal resistance/impedance of this device extracted from this experimental data is 0.2 K/mW (the same as for the other 40- μm cavity described above).

The electrical resistance of our device was extracted from the slope of “I-V” curve and was about 20 Ohms for a 40- μm long cavity (Fig. 27).

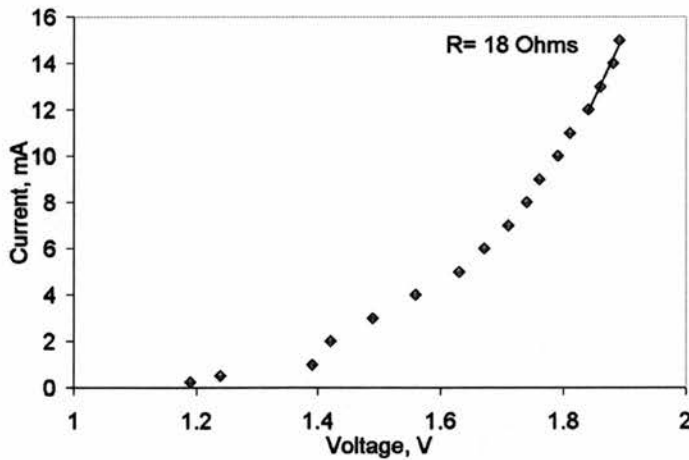


Fig. 27. I-V curve for a 40- μm cavity exhibiting 20 Ohms differential resistance.

It is noteworthy that the laser operation did not affect our tunability measurements, as almost the entire out-put laser power was absorbed by access waveguides, and, thus,

did not interfere with the detected light propagating through the devices from the external tunable laser.

Larger shifts may be achieved by shifting the reflectivity peak of the mirrors (Fig. 28), in order to suppress the laser action at the gain peak, hence increasing the tuning range. This improvement, however, requires a very careful cavity design, in order to ensure low reflectivity at the peak of the gain curve.

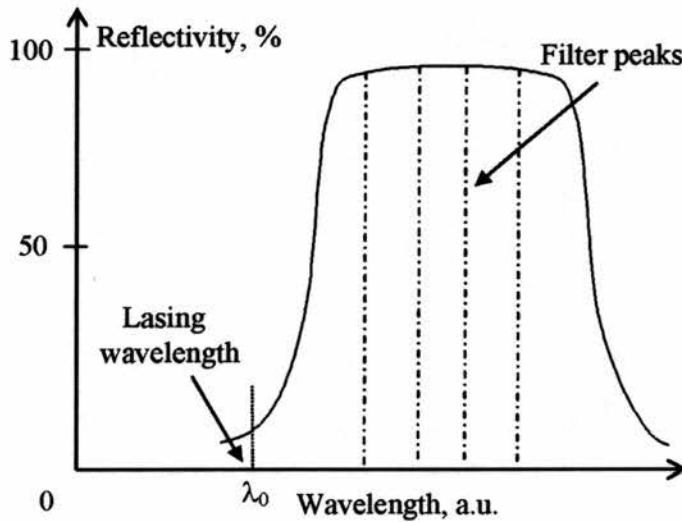


Fig. 28. A schematic view of a possible filter design for lasing suppression.

5.5 Comparison of tunable filters operated by quantum confined Stark effect and carrier injection

Table 4 shows a comparison between the achieved filter transmission peak shifts induced via QCSE and carrier injection.

Table 4. Comparison of experimental results obtained for QCSE- and carrier injection-based filters

<i>Parameters</i>	<i>QCSE</i>	<i>Carrier injection</i>
Number of QWs	10	5
Confinement factor, %	6	8
Cavity length, μm	20	20
Shift, nm	1.2	1.5
Detuning from the band-edge, nm	70	40
Electric field, kV/cm	37.4	50 (corresponds to 2.7 mA)
$\Delta n/E$, m/V	821	758
Material index change	~ 0.05	~ 0.05

As one can see from Table 4, the observed shifts for the different methods are in fact very close to one another (a QCSE red shift of 1.2 and a carrier injection blue shift of 1.5 nm). Considering the conditions under which these shifts were observed, one can see that the QCSE-induced red shift was obtained at a smaller applied electric field and further away from the band-edge, compared with the carrier-induced shift. Using the experimentally measured electro-optic parameter of $\eta = 14 \cdot 10^{-5} \text{ meV cm}^2 \text{ kV}^{-2}$ (see above), we can predict a QCSE-induced red shift of 3 nm for the applied voltage of 50 kV/cm and a detuning of $\Delta\omega = 44 \text{ meV}$. Furthermore, QCSE is faster ($\sim \text{ps}$) than carrier-injection ($\sim \text{ns}$), as there is no need to sweep carriers out of the QWs. However, QCSE-related absorption losses are higher and increase rapidly compared to carrier injection. This can badly compromise the filter performance (reduced Q-factor) at high electric-fields ($> 100 \text{ kV/cm}$).

As was mentioned earlier, carrier injection is dependant on carrier recombination at the sidewalls. Carriers that recombine non-radiatively at the side walls do not contribute to changes in the refractive index or produce gain, while still causing heating effects. It has been shown [30] that the ion damages produced during dry etching (especially for high beam-voltages for 1500 V) may result in an increase in the surface recombination velocity by a factor of 4. This makes carrier-injection-based tunable devices very

dependant on the fabrication techniques. A wet etching step applied afterwards has been suggested as a method of reducing the surface recombination velocity.

The QCSE-based device does not suffer from problems such as carrier surface recombination and heating. An overall comparison of the advantages and disadvantages of the two different methods is given in Table 5.

Table 5. Summary of advantages/disadvantages of QCSE and carrier-injection for realization of active components

<i>QCSE</i>	<i>Carrier Injection</i>
	Sensitive to carrier surface recombination
High speed (~ps)	Lower speed (~ns)
High absorption losses	
	Carrier-induced heating leading to thermo-optic shift
	Highly dependant on fabrication quality
Narrowband: only works near band-edge	Broadband: Plasma effect works away from band-edge; band filling has narrowband, however.
Compact devices	Compact devices
QCSE, ideally, consumes less power since no current flows	Low power consumption (few mA of current)

5.6 Summary

Deeply etched tunable filters in the InP-based material with 5 and 10 quaternary QWs were designed and successfully fabricated. A FWHM of less than 2 nm and a FSR of 12 nm was experimentally achieved for the filter with a 20- μ m cavity. At an applied field of 37.5 kV/cm, we observed a red shift of 1.2 nm in the position of the filter peak at wavelength of 1319 nm for 10 QW QCSE material. This shift corresponds to the efficiency $\Delta n/E=820*10^{-12}$ m/V.

For an increased applied field up to 50 kV/cm at a wavelength of 1265 nm, we predict that the red shift may reach 5 nm, though with considerably increased absorption losses. The use of the chopped (coupled) QWs [31] can give up to 2 times higher QCSE red shifts. With the slight increase of the strain, this chopped QW material may also be used for polarization-independent switching.

Using carrier injection, shifts of 1.5 nm (DC) and 1.9 nm (pulsed) were achieved for the 5 QWs material. Only 6 mW of power was consumed. A design with large contact pads (relative to the size of the cavities) allowed us to reach relatively small thermal resistances of 0.2 and 0.4 K/mW for the filters with 40- and 20- μm cavities, respectively. The use of an additional wet-etching step may minimize the additional surface recombination velocity caused by dry-etching and increase the amount of the carriers available for tuning.

Both these devices suffered from the effects of absorption in the access waveguides. By contacting and pumping these waveguides, this absorption may be avoided. Through the integration of such filters with semiconductor optical amplifiers not only is the loss reduced, but operation is enabled closer to the bandgap, with a consequent improvement in the resonance shift.

Overall, we have highlighted the limitations and opportunities for III-V semiconductor-based tunable microphotonic circuit elements by demonstrating compact tunable filters in the 1.3 μm wavelength regime.

The red and blue shifts of resonance transmission peaks were observed for the QCSE- and carrier-injection tuned devices, respectively. The tuning results were analysed and compared, showing advantages and disadvantages of both mechanisms. Parameters important for successful tuning, when designing and using microcavities based on any of these tuning mechanisms, were highlighted.

References

- [1] T. A. Ibrahim, W. Cao, Y. Kim, J. Li, J. Goldhar, P.-T. Ho and C. H. Lee, "Lightwave switching in semiconductor microring devices by free carrier injection," *J. Lightwave Technol.*, vol. 21, pp. 2997-3003, Dec 2003.
- [2] K. Djordjev, S.-J. Choi, S.-J. Choi, and P.D. Dapkus, "Microdisk tunable resonant filters and switches," *IEEE Photon. Technol. Lett.*, vol. 14, pp. 828-830, June 2002.
- [3] C. A. Barrios, V. R. Almeida, R. R. Panepucci, B. S. Schmidt, and M. Lipson, "Compact Silicon Tunable Fabry-Perot Resonator with low power consumption," *IEEE Photon. Technol. Lett.*, vol. 16, pp. 506-508, Feb 2004.
- [4] N. C. Panoiu, M. Bahl, and R. M. Osgood, "Ultrafast optical tuning of a superprism effect in nonlinear photonic crystals," *J. Opt. Soc. Am. B*, vol. 21, pp. 1500-1508, Aug 2004.
- [5] G. Cocorullo, M. Iodice, and I. Rendina, "All-silicon Fabry-Perot modulator based on the thermo-optic effect," *Opt. Lett.*, vol. 19, pp. 420-422, Mar 1994.
- [6] D. Hofstetter and R. Thornton, "Theory of loss measurements of Fabry-Perot resonators by Fourier analysis of the transmission spectra," *Opt. Lett.*, vol. 22, pp. 1831-1833, Dec 1997.
- [7] T. F. Krauss and R. De La Rue, "Optical characterization of waveguide based photonic microstructures," *Appl. Phys. Lett.*, vol. 68, pp. 1613-1615, Mar 1996.
- [8] D. A. B. Miller, D. S. Chemla, T. C. Damen, A. C. Gossard, W. Wiegmann, T. H. Wood, and D. A. Burrus, "Electric field dependence of optical absorption near the band gap of quantum-well structures," *Phys. Rev. B*, vol. 32, pp. 1043-1060, Jul 1985.
- [9] R.I. Killey, C. P. Liu, M. Whitehead, P. Stavrinou, J. B. Song, J. S. Chadha, D. Wake, C. C. Button, G. Parry, and A. J. Seeds, "Multiple Quantum Well Asymmetric Fabry-Perot Modulators for RF-over-Fiber Applications," *IEEE Trans. Microwave Theory and Techniques*, vol. 49, pp. 1888- 1893, Oct 2001.
- [10] J. S. Weiner, D. A. B. Miller, and D. S. Chemla, "Quadratic electro-optic effect due to the quantum-confined Stark effect in quantum wells," *Appl. Phys. Lett.*, vol. 50, pp. 842-844, Mar 1997.

- [11] H. Temkin, D. Gershoni, and M. B. Panish, "InGaAsP/InP quantum well modulators grown by gas source molecular beam epitaxy," *Appl. Phys. Lett.*, vol. 50, pp. 1776-1778, Jun 1987.
- [12] R. W. Martin, S. L. Wong, R. J. Nicholas, K. Satzke, M. Gibbon, and E. J. Thrush, "The design of quantum-confined Stark effect modulators for integration with 1.55 μm lasers," *Semic. Sci. Technol.*, vol. 8, pp. 1173-1178, 1993.
- [13] P. Abraham, J. Piprek, S. P. Denbaars, and J. E. Bowers, "Study of temperature effects on loss mechanisms in 1.55 μm laser diodes with $\text{In}_{0.81}\text{Ga}_{0.19}\text{P}$ electron stopper layer," *Semic. Sci. Technol.*, vol. 14, pp. 419-424, 1999.
- [14] A. S. Sudbo, "Film mode matching: a versatile numerical method for vector mode field calculations in dielectric waveguides," *Pure Appl. Opt.*, vol. 2, pp. 211-233, 1993.
- [15] W. Bogaerts, P. Bienstman, D. Taillaert, R. Baets, and D. De Zutter, "Out-of-plane scattering in 1-D photonic crystal slabs," *Optic. And Quant. Electron.*, vol. 34, pp. 193-203, Jan/Mar 2002.
- [16] M. Qiu, "Effective index method in heterostructure slab waveguide based two-dimensional photonic crystals," *Appl. Phys. Lett.*, Vol. 81, pp. 1163-1165, Aug 2002.
- [17] J. E. Zucker, I. Bar-Joseph, B. I. Miller, U. Koren, and D. S. Chemla, "Quaternary quantum wells for electro-optic intensity and phase modulation at 1.3 and 1.55 μm ," *Appl. Phys. Lett.*, vol. 54, pp. 1989-1991, Jan 1989.
- [18] J. E. Zucker and T. L. Henderickson, "Electro-optic phase modulation in GaAs/AlGaAs quantum well waveguides," *Appl. Phys. Lett.*, vol. 52, pp. 945-947, Mar 1988.
- [19] R. Grover, T. A. Ibrahim, S. Kanakaraju, L. Lucas, L. C. Calhoun, and P.-T. Ho, "A tunable GaInAsP-InP optical microring notch filter," *IEEE Photon. Technol. Lett.*, vol. 16, pp. 467-469, Feb 2004.
- [20] M. Boroditsky, I. Gontijo, M. Jackson, R. Vrijen, E. Yablonovitch, T. F. Krauss, C-C Cheng, A. Scherer, R. Bhat, and M. Krames, "Surface recombination measurements on III-V candidate materials for nanostructure light-emitting diodes," *J. Appl. Phys.*, vol. 87, pp. 3497-3504, Apr 2000.

- [21] N. Dudovich, G. Levy Yurista, A. Sharon, A. A. Friesem, and H.-G. Weber, "Active semiconductor-based grating waveguides structure," *IEEE J. Quantum Electron.*, vol. 37, pp. 1030-1039, Aug 2001.
- [22] B. R. Bennett, R. A. Soref, and J. A. Del Alamo, "Carrier-induced change in refractive index of InP, GaAs, and InGaAsP," *IEEE J. Quantum Electron.*, vol. 26, pp. 113-122, Jan 1990.
- [23] L. A. Coldren and S. W. Corzine, *Diode Lasers and Photonic Integrated Circuits*, Wiley Series in microwave and optical engineering, New York: J. Wiley, Chapter 2, 1995.
- [24] F. G. D. Corte, G. Cocorullo, M. Iodice, and I. Rendina, "Temperature dependence of the thermo-optic coefficient of InP, GaAs, and SiC from room temperature to 600 K at the wavelength of 1.5 μm ," *Appl. Phys. Lett.*, vol. 77, pp. 1614-1616, Sept 2000.
- [25] K. P. Pipe and R. J. Ram, "Comprehensive heat exchange model for a semiconductor laser diode," *IEEE Photon. Technol. Lett.*, vol. 15, pp. 504 -506, Apr 2003.
- [26] H. K. Tsang, M. W. Mak, L. Y. Chan, J. B. D. Soole, C. Youtsey, and I. Adesida, "Etched cavity InGaAsP/InP Waveguide Fabry-Perot filter tunable by current injection," *J. Lightwave Technol.*, vol. 17, pp. 1890-1895, Oct 1999.
- [27] S. J. Choi, Z. Peng, Q. Yang, S. J. Choi, and P. D. Dapkus, "Tunable microdisk resonators vertically coupled to bus waveguides using epitaxial regrowth and wafer bonding techniques," *Appl. Phys. Lett.*, vol. 84, pp. 651-653, Feb 2004.
- [28] T. Krauss, "Semiconductor ring laser," PhD thesis, University of Glasgow, 1992.
- [29] P. W. A. McIlroy, A. Kurobe, and Y. Uematsu, "Analysis and Application of theoretical Gain Curves to the design of Multi-Quantum well laser," *IEEE J. Quantum Electron.*, vol. 21, pp. 1958-1963, Dec 1985.
- [30] P. D. Hewitt and G. T. Reed, "Improved modulation performance of a silicon p-i-n device by trench isolation," *J. Lightwave Technol.*, vol. 19, pp. 387-390, Mar 2001.
- [31] B. H. Dorren, A. Yu. Silov, M. R. Leys, D. M. H. Dukers, J. E. M. Haverkort, D. H. Maat, Y. Zhu, F. H. Groen, and J. H. Wolter, "A chopped quantum-well polarization independent interferometric switch at 1.53 μm ," *IEEE J. Quantum Electron.*, vol. 36, pp. 317-324, Mar 2000.

[32] E. S. Koteles, "Integrated planar waveguide demultiplexers for high density WDM applications", *Proc. SPIE Wavelength Division Multiplexing (a critical review)*, vol. CR71, edited by R. T. Chen and L. S. Lome, SPIE Optical Engineering Press, Bellingham, USA, pp. 3-32, 1999.

Chapter 6

Conclusion

The results achieved during the work described in this thesis are summarised in this chapter. Possible means of improvement are suggested. Future work following the progress made in the thesis is discussed.

6.1 Achieved results

We have developed a high voltage chemically assisted ion beam etching (CAIBE) regime that is very favourable for the etching of high-aspect-ratio one- and two-dimensional photonic crystals in InP-based material. This regime makes use of a high beam voltage to beam current ratio, which allows:

- a) the partial elimination of one of the classic InP etching problems such as wobbling; we define “wobbling” as poor etching directionality at the bottom portions of high aspect ratio features in InP. The reason for this issue is not fully understood yet, however, using high beam voltage etching regime improves this etching directionality;
- b) an improvement of the semiconductor/mask selectivity (up to 34:1) through silica hardening under the impact of high energy argon ions. It is always preferable to use the minimum mask thickness, as this gives the highest resolution;
- c) the production of improved etch depth of $> 5 \mu\text{m}$ (for holes of 250 nm diameter); such a large etch depth is important due to another InP etching problem- tapered bottoms. Gradually narrowing bottoms of high-aspect-ratio features, referred to as tapered bottoms, can cause out-of-plane scattering and coupling of the guided mode to substrate modes. Thus, the deeply etched holes allow us to keep these tapered areas as far as possible

from the waveguide core, minimising their detrimental effect on the propagation of the guided mode;

- d) the reduction of wall roughness due to etching at low beam-currents, which causes a large ion-induced chemical-etching yield. It means that the amount of chemical etching per ion is large, resulting in a strong chemical reaction, which smoothes out the damage caused by the ion impacts. Smooth walls are desirable for low-loss propagation.

Once this etching regime was developed, it allowed us to fabricate low-loss two-dimensional (2-D) photonic crystal (PhC) planar waveguides in the InP heterostructure. These PhC waveguides were optically characterized using an “end-fire” method. Propagation losses were determined by applying the Fourier transform technique to the experimental Fabry-Perot (F-P) spectrum of waveguides containing PhCs. Losses as small as 1.8 dB/mm were measured for the PhC waveguides consisting of three air rows removed for a 400-nm period. To the best of our knowledge, these were the lowest reported losses at that time, which, in fact, reached the intrinsic limit for PhCs of this type [1].

After the demonstration of low-loss PhC waveguides, we moved on to developing active PhC-based components, which could constitute a building block for photonic integrated circuits. As a first step towards tunability, filters based on one-dimensional (1-D) PhCs were designed. These filters consist of a F-P cavity with deeply etched 1-D PhC mirrors on each side of it. To comply with the wavelength division multiplexing (WDM) criteria requiring a channel spacing less than 2 nm [2], filters with full width at half maximum (FWHM) of < 2 nm were designed. In order to realise tunability, two methods were implemented, the quantum confined Stark effect (QCSE) and free carrier-injection. Applying forward (for carrier-injection) or reverse (for QCSE) biases to the filter cavity region creates changes of the refractive index that cause shifts of filter resonances. Blue-shifts (carrier-injection) of 1.9 nm and red-shifts (QCSE) of 1.5 nm were experimentally observed for filters with 20- μm long cavities fabricated in 5 and 10 quaternary/quaternary InGaAsP/InGaAsP Multiquantum-well (MQW) material, respectively.

The tuning results were analysed, highlighting advantages and disadvantages of both mechanisms. For example, tuning via carrier-injection has the down-side of thermal

heating, which produces refractive index changes opposing those of carrier-injection. We experimentally observed small thermal-induced shifts of the filter resonances during free carrier-injection. Values for the thermal resistances of the cavities were also derived from these experiments. These were rather low (< 0.5 K/mW), which allowed us to keep parasitic thermal tuning to a minimum. This compares favourably to a tunable filter realised on silica-on-insulator (SOI), where due to high thermal resistances the thermal tuning mechanism¹ overcame tuning via carrier-injection [3].

6.2 Possible improvements and future work

PhC's properties are strongly affected by the propagation losses. Thus, achieving the intrinsic loss limit for the PhCs is an important task. The etching technique developed in this thesis as well as the etching results presented in [4, 5] allow the fabrication of high-quality low-loss 2-D planar PhC waveguides. By further optimization of the planar waveguide structure for a given etching process and for given hole shapes, a regime where losses reach their lower limit was achieved [1]. We managed to reach the intrinsic loss limit (~ 2 dB/mm) for W3 PhC planar waveguides of 400-nm period etched to the depth of 5.3 μm . However, the intrinsic loss limit has yet to be reached for PhC waveguides with smaller periods (~ 300 nm) due to poorer etching profiles (less deep, tapering starts earlier). This can be achieved by further development of the etching regimes (increasing substrate temperature/decreasing chlorine flow, *etc.*).

One of the motivations of our study of W3 (three air rows removed) waveguides is the fact that these broader waveguides have lower propagation losses than PhC waveguides with one row removed. Thus, they are more favourable for practical applications. At the same time, the presence of higher-order modes in these W3 waveguides creates unique mini-stop bands, which offer important opportunities for spectral and dispersive functionalities. For example, E. Schwoob *et al.* [6] have proposed a wavelength monitor for WDM, based on W3 and W5 PhC planar waveguides, with 500 GHz inter-channel spacing. Thus, there would be some interest in trying to tune these mini-stop bands.

¹ Thermal tuning is undesirable due to its low speed.

At the moment, the experimentally achieved tuning range of the filters is limited to about 2 nm, which is rather small for wide practical use in dense WDM systems. However, several ways of increasing tuning range of the filters are possible:

For QCSE-based devices:

- a) working closer to the absorption peak; a red shift of 5 nm was predicted (for our material and design) at a wavelength of 1265 nm for an increased applied field of only 50 kV/cm, though with increased absorption losses; additional pumping of the access waveguides can provide some gain to counter-balance absorption losses in the cavity;
- b) increasing the overlap Γ between the QWs and the optical field will lead to bigger modal refractive index changes. A straightforward way of increasing Γ is to increase the number of the QWs, but this will cause higher absorption losses. An improvement of Γ can be obtained by reducing the barrier width down to 7.6 nm and, thus, concentrating all 10 QWs in the middle of the waveguide core, which will increase Γ from the current 6 % to 9 %. Further decrease of the waveguide core down to typical widths of \sim 380 nm will allow us to reach Γ as big as 16 %; although this method will also result in higher absorption losses;
- c) the use of the coupled QWs (with very thin barriers [7]) can produce up to 2 times higher QCSE-induced red shifts.

For carrier-injection-based devices:

- a) suppressing laser action of the cavities at the gain peak, via shifting the reflectivity peak of the mirrors, will allow the use of higher carrier densities, thus, increasing the possible tuning range of the filter;
- b) applying a wet etching step after CAIBE will reduce the surface recombination velocity of the carriers, thus increasing the amount of “useful” carriers which participate in the refractive index changes for a given amount of the injected carriers; this would improve the efficiency of the device and minimise the thermal effects. This would be especially useful for the devices in which lasing has been suppressed (see (a));

- c) increasing the number of QWs will increase the overlap Γ . Although, there is a risk of an uneven distribution of the carriers, which could lead to the reduction of the effective Γ .

Also, it should be technically possible to achieve tuning via carrier-injection and QCSE in the same device. This would almost double the tuning range and enhance the usefulness of these devices. However, some very careful modelling will be necessary to realize this type of devices.

Applying the QCSE and carrier-injection tuning mechanisms to 2-D PhCs is one of the future steps. Carrier-injection of 2-D PhC microcavities was already demonstrated by Baba *et al.* [8] via optical pumping. However, having an additional external optical source for optical pumping of 2-D PhCs is undesirable for use in integrated circuits with many elements. Thus, the electrical pumping considered in our thesis would be preferable.

One of possible applications of a small tuning range (of < 10 nm) is tunable PhC-based dispersion compensating devices. Due to the fact that the dispersion curve of the PhC waveguide changes rapidly, shifts of even a couple of nanometres along dispersion curve will be enough to change the dispersion relation dramatically.

Another possibility is to use small tuning ranges in PhC-based microcavities, which possess a very high Q-factor of 100 000 and can have extremely narrow peaks of less than 0.1 nm (0.022 nm) [9] (these values were recorded for the “membrane”-type of PhC, where there is no possibility of heat-sinking during carrier-injection).

In conclusion, our future work lies in improving the etching regime for the W3 PhC waveguides with small periods (~ 300 nm) in order to reach lower losses than those reported here (~ 3.5 dB/mm) and optimizing the waveguide structure for a given etch depth and shape to achieve comparable losses for the W1 waveguides. Regarding tuning, we should try to optimise our 1-D PhC-based filters in order to get wider tuning ranges and apply tuning to the 2-D PhCs which have considerable potential.

References

- [1] R. Ferrini, A. Berrier, L. A. Dunbar, R. Houdré, M. Mulot, S. Anand, S. de Rossi and A. Talneau, "Minimization of out-of-plane losses in planar photonic crystals by optimizing the vertical waveguide," *Appl. Phys. Lett.*, vol. 85, pp. 3998-3400, Nov 2004.
- [2] E. S. Koteles, "Integrated planar waveguide demultiplexers for high density WDM applications", *Proc. SPIE Wavelength Division Multiplexing (a critical review)*, vol. CR71, edited by R. T. Chen and L. S. Lome, SPIE Optical Engineering Press, Bellingham, USA, pp. 3-32, 1999.
- [3] C. A. Barrios, V. R. Almeida, R. R. Panepucci, B. S. Schmidt, and M. Lipson, "Compact Silicon Tunable Fabry-Perot Resonator with low power consumption," *IEEE Photon. Technol. Lett.*, vol. 16, pp. 506-508, Feb 2004.
- [4] M. Mulot, S. Anand, R. Ferrini, B. Wild, R. Houdré, J. Moosburger, and A. Forchel, "Fabrication of two-dimensional InP-based photonic crystals by chlorine based chemically assisted ion beam etching," *J. Vac. Sci. Technol. B*, vol. 22, pp. 707-709, Mar 2004.
- [5] F. Pommereau, L. Legouézigue, S. Hubert, S. Sainson, J.-P. Chandouineau, S. Fabre, G.-H. Duan, B. Lombardet, R. Ferrini, and R. Houdré, "Fabrication of low loss two-dimensional InP photonic crystals by inductively coupled plasma etching," *J. Appl. Phys.*, vol. 95, pp. 2242-2245, Mar 2004.
- [6] E. Schwoob, H. Benisty, F. Pommereau, L. Legouézigue, J.-P. Chandouineau, O. Drisse, O. Legouézigue, C. Cuisin, G.-H. Duan, S. Golka, K. Janiak, H. J. Hensel, and H. Heidrich, "Fault-tolerant in-plane wavelength monitor exploiting mini-stopbands of a multimode planar photonic crystal waveguide," *Proc. International Workshop on Photonic Electromagnetic Structures (PECS)*, Kyoto, Japan, 2004.
- [7] B. H. Dorren, A. Yu. Silov, M. R. Leys, D. M. H. Dukers, J. E. M. Haverkort, D. H. Maat, Y. Zhu, F. H. Groen, and J. H. Wolter, "A chopped quantum-well polarization independent interferometric switch at 1.53 μm ," *IEEE J. Quantum Electron.*, vol. 36, pp. 317-324, Mar 2000.
- [8] T. Baba, M. Shiga, K. Inoshita and F. Koyama, "Carrier plasma shift in GaInAsP photonic crystal point defect cavity," *Electr. Lett.*, vol. 39, pp. 1516-1517, Oct 2003.

[9] Y. Akahane, T. Asano, B-S. Song, and S. Noda, "Demonstration of ultrahigh-Q photonic Nanocavity based on Gaussian-like optical confinement," *Proc. International Workshop on Photonic Electromagnetic Structures*, Kyoto, Japan, 2004.